Atomic layer lithography of plasmonic nanogaps for enhanced light-matter interactions: fabrication and applications

A THESIS
SUBMITTED TO THE FACULTY OF
UNIVERSITY OF MINNESOTA
BY

Xiaoshu Chen

IN PARTIAL FULFILLMENT OF THE REQUIREMENTS
FOR THE DEGREE OF
DOCTOR OF PHILOSOPHY

Sang-Hyun Oh

January 2016

Acknowledgements

I would first like to thank my advisor, Professor Sang-Hyun Oh, for his continuous support, guidance, and motivation over the past five years of my Ph.D. study. I appreciate the opportunities in his lab that allowed me to work on several different scientific projects, attend conferences and collaborate with scientists around the world.

I would also like to thank my collaborators, Prof. Nathan Lindquist, Prof. Matthew Pelton, Prof. David Smith, Prof. Stefan Maier, Prof. Jaime Peraire, Prof. David Norris, Dr. Christian Ciracì, and Dr. Ngoc-Cuong Nguyen. Their expertise and knowledge helped to extend my study to broader areas. And many thanks go to my lab fellow members, especially, Hyungsoon Im, for helping me to start my research in nanofabrication, and Hyeong-Ryeol Park, for working together through many projects. Also thanks to many current and previous lab members including Antoine Lesuffleur, Luke Jordan, Avijit Barik, Tim Johnson, Jonah Shaver, Si-Hoon Lee, DaeHan Yoo, Dan Mohr, Nathan Wittenberg, Shailabh Kumar, Dan Klemme, Seon Namgung, Yong Sang Ryu, Lauren Otto, Steve Olson, Sudhir Cherukulappurath, and Jincy Jose, who have also

provided me with many support and good friendship through the years. I thank the staffs in Minnesota Nano Fabrication Center and Characterization Facility for helping me with all the tools and processes.

I thank my family and friends for all the supports, encouragements and fun through the past five years. Especially thanks to my parents, for their love through my life. Also to my husband, thank him for always being the strongest support and a best friend. I thank Liyuan Zhang, who works out with me in gym every week, and always being a great friend. All of these people mentioned above and some people not been mentioned helped me to go through the past five years of hard work.

Dedication

I dedicate this thesis to my husband and our parents for all of their love and support throughout my life.

Abstract

Enhanced light-matter interactions at the nanometer scale have many potential applications, such as thin film sensing, enhanced Raman scattering, enhanced infrared absorption, particle manipulation, among others. Metal – insulator – metal nanogap structure is one of the most effective plasmonic devices for such applications since they are capable of generating the strongest light field enhancement inside the nanogap. However, current techniques to make such nanogap structures are either very expensive, slow, or lacking of control over nanogap size, pattern shape, and position. In this thesis, two wafer-scale fabrication methods are presented to address the challenges in fabrication. The fabricated devices are then used to demonstrate the above-mentioned applications.

Atomic layer deposition is used in both methods to define the width of nanogap with angstrom resolution. The length, position, and shape of the nanogaps are precisely controlled in wafer scale by photolithography and metal deposition. A simple tape peeling and a template stripping process are used to expose the nanogaps. Nanogap devices with different designs are proved to support strong optical resonances in visible,

near infrared, mid infrared, and terahertz-frequency regimes. By squeezing electromagnetic waves into nanometer wide gaps, huge field enhancement can be achieved inside the gaps. These novel fabrication methods can easily be duplicated and thus lead to broad studies and applications of the enhanced light-matter interactions.

Table of Contents

List of Tables

List of Figures

List of Publications

1. **Xiaoshu Chen**†, Hyeong-Ryeol Park†, Matthew Pelton, Xianji Piao, Nathan C. Lindquist, Hyungsoon Im, Yun Jung Kim, Jae Sung Ahn, Kwang Jun Ahn, Namkyoo Park, Dai-Sik Kim, and Sang-Hyun Oh, "Atomic layer lithography of wafer-scale nanogap arrays for extreme confinement of electromagnetic waves", Nature Communications, 4, 2361, 2013. †Equal contribution. http://dx.doi.org/10.1038/ncomms3361.
2. **Xiaoshu Chen**, Christian Ciracì, David R. Smith, Sang-Hyun Oh, "Nanogap-enhanced Infrared Spectroscopy with Wafer-scale Arrays of Buried Plasmonic Cavities", Nano Letter, 2015, 15, 107-113. http://dx.doi.org/10.1021/nl503126s.
3. **Xiaoshu Chen**†, Hyeong-Ryeol Park†, Nathan C. Lindquist, Jonah Shaver, Matthew Pelton, Sang-Hyun Oh, "Squeezing Millimeter Waves through a Single, Nanometer-wide, Centimeter-long Slit", Scientific Report, 4, 6722, 2014. †Equal contribution. http://dx.doi.org/10.1038/srep06722.
4. Hyeong-Ryeol Park†, **Xiaoshu Chen**†, Ngoc-Cuong Nguyen†, Jaime Peraire, and Sang-Hyun Oh, "Nanogap-enhanced Terahertz Sensing of 1-nm-thick (λ/1000000) Dielectric Films," ACS Photonics, **2**, 417-424. †Equal contribution. http://dx.doi.org/10.1021/ph500464j.
5. Hyeong-Ryeol Park, Seon Namgung, **Xiaoshu Chen**, and Sang-Hyun Oh, "High-density metallic nanogap arrays for sensitive detection of single-walled carbon nanotube thin films", Faraday Discussions, **178**, 195-201, 2015. http://dx.doi.org/10.1039/C4FD00233D.

6. Hyeong-Ryeol Park, Seon Namgung, **Xiaoshu Chen**, Nathan C. Lindquist, Vincenzo Giannini, Yan Francescato, Stephen A. Maier, and Sang-Hyun Oh. "Perfect extinction of terahertz waves in monolayer graphene over 2-nm-wide metallic apertures", Advanced Optical Materials, **3**, 667-673, 2015. http://dx.doi.org/10.1002/adom.201400546.
7. J. Britt Lassiter, **Xiaoshu Chen**, Xiaojun Liu, Christian Ciracì, Sang-Hyun Oh, Maiken H. Mikkelsen and David R. Smith, etc., "Third-Harmonic Generation Enhancement by Film-Coupled Plasmonics Stripe Resonators", ACS Photonics, **1**, 1212-1217, 2014. http://dx.doi.org/10.1021/ph500276v.
8. Christian Ciracì, **Xiaoshu Chen**, Jack J. Mock, Felicia McGuire, Xiaojun Liu, Sang-Hyun Oh, and David R. Smith, "Film-coupled nanoparticles by atomic layer deposition: comparison with organic spacing layers", Applied Physics Letters, **104**, 023109, 2014. http://dx.doi.org/10.1063/1.4861849.
9. Nathan C. Lindquist, Jincy Jose, Sudhir Cherukulappurath, **Xiaoshu Chen**, Timothy W. Johnson, and Sang-Hyun Oh, "Tip-Based Plasmonics: Squeezing light with metallic nanoprobes", Laser & Photonics Reviews, **7**, 453-477, 2013. http://dx.doi.org/10.1002/lpor.201209044.
10. Sriharsha, V. Jayanti, Jong Hyun Park, Alexandr Dejneka, Dagmar Chvostova, Kevin M. McPeak, **Xiaoshu Chen**, Sang-Hyun Oh, David J. Norris, "Low – temperature enhancement of plasmonic performance in silver films", Optical Materials Express, 5, 1147-1155, 2015. http://dx.doi.org/10.1364/OME.5.001147.

CHAPTER 1

1. Introduction

1.1 Introduction and motivation

Light, as a part of electromagnetic waves, interacts with materials and thus reveals information of the world around us. The strength of the light-matter interactions depends on the relative energy of the light and the matter, intensity of the light field, and the alignment between the momentum of the light and the matter. The interactions between light and nano sized materials, such as molecules, are usually very weak due to the mismatch between the wavelength of the light and the size of nano materials. There are many methods to enhance light-matter interactions, for example, increasing the interaction volume, increasing the intensity of light, and matching the light frequency with the frequency of the oscillations of the matter. Enhanced interactions have been demonstrated for many applications, such as surface enhanced spectroscopy[1, 2], high-resolution imaging[3] , photovoltaics[4], integrated optical circuits[5], optical trapping[6], light emission[7], data storage[8, 9], and biosensing[10], etc.

One method to enhance light matter-interaction is to confine light into a small volume to increase the intensity of the light field locally. With normal optical lens, light in free space can be focused into a spot of a radius about half of the wavelength, which is known as the diffraction limit. Deep-subwavelength confinement of optical energy has been demonstrated using nano-sized metal particles[11-16], holes[17-19], slits[19-21], gaps[22-24], and tips[25], etc. The greatest degree of confinement is obtained within a nanometer-scale gap between two metals[15,16, 26].

Existing methods, such as aggregates of noble-metal nanoparticles[15,16, 26], electromigration[27], electron-beam (e-beam) lithography[28], or scanning probes[29], are capable of fabricating nanometer-scale gaps in metal film. However, none of these methods can fabricate angstrom-scale devices, control the geometries precisely, and at the same time guarantee wafer size area uniformity. Furthermore, these methods are primarily used to make point-like junctions. The amount of light that can be coupled from free space into the point-like junctions is limited, due to the size mismatch between the optical wavelength and size of the junction. On the other hand, transmission measurements on these point-like junctions are impractical, because of the large background of light that passes by next to the junction. These challenges become even

greater at longer wavelengths. In particular, squeezing millimeter waves (THz waves) into one-nanometer scale gaps would lead to extremely high field enhancements, but exploiting resonances at THz frequencies will require the nanogap to be extended over millimeter length scales.

Therefore, the motivation of the work is to develop a lower cost, higher throughput, larger area, and simpler fabrication method to fabrication nanogap structures, which can help to achieve real applications of enhanced light-matter interactions in plasmonic nanogap structures.

1.2 Scope of this thesis

The scope of this thesis includes the development of new fabrication methods to create nanogaps and exploring the applications of the nanogaps for enhanced light-matter interactions. First, I will discuss my new method to fabricate vertical nanogap structures at the wafer scale. The nanogaps are then characterized optically and electrically, and then being used as a platform for thin film sensing. Also introduced are the modifications of the methods and pattern designs to make different types of nanogaps, such as buried nanogaps and planar nanogaps, for various studies and applications, including enhanced

absorption, nonlinear optical effects, molecule sensing, small particles manipulation and light emission. Finally, some future directions are discussed.

This thesis is organized into the following chapters, each outlining a significant portion of the original research performed throughout my Ph.D. study.

- Chapter 2 presents theoretical background as a basis for following chapters, including solving Maxwell equations with Drude model for surface plasmon. Plasmons in nanogap structures are introduced. And light-matter interactions at the nanometer scale are also discussed.
- Chapter 3 introduces our solutions to make three different forms of ultra thin nanogaps with simple and high-throughput fabrication methods. Previous efforts for making nanogap structures are also briefly discussed. The electron microscopy characterization of the nanogap structures is presented.
- Chapter 4 discusses the optical characterization of the nanogap structures in the visible, near infrared, mid infrared and THz regimes.
- Chapter 5 introduces the applications of buried nanogap arrays for surface enhanced infrared absorption and surface enhanced Raman scattering. Nanogap-enhanced thin

film sensing using THz waves and enhanced nonlinear optical effects are briefly introduced.

- Chapter 6 presents the fabrication methods for electrically addressable nanogap chips and the application in tunneling-induced light emission.
- Chapter 7 is a summary of the work preformed for my Ph.D. study. Also included is a discussion of future directions.

CHAPTER 2

2. Theory and Background

This chapter provides the theoretical support for the following chapters. First, fundamental theories of surface plasmon resonance and gap plasmon resonance are described. Additionally, the theoretical backgrounds for surface enhanced Raman scattering and surface enhanced infrared absorption are introduced.

2.1 Optical properties of materials

2.1.1 Drude model

Maxwell's equations describe electromagnetic fields and how they evolve over time. The equations provide a fundamental understanding of light and light-matter interactions, and take the following forms:

$$\nabla \cdot \mathrm{D} = \rho \tag{2.1}$$

$$\nabla \cdot \mathrm{B} = 0 \tag{2.2}$$

$$\nabla \times \mathrm{E} = -\frac{\partial \mathrm{B}}{\partial \mathrm{t}} \tag{2.3}$$

$$\nabla \times \mathrm{H} = \mathrm{J} + \frac{\partial \mathrm{D}}{\partial \mathrm{t}} \tag{2.4}$$

Here, E (Volts per meter) and H (Amperes per Meter) are electric and magnetic fields. D (Coulombs per square meter) and B (Tesla) are materials related electric flux density and the magnetic flux density, respectively, and are defined as:

$$\varepsilon = \varepsilon_r \varepsilon_0 \tag{2.5}$$

$$\mu = \mu_r \mu_0 \tag{2.6}$$

$$D = \varepsilon E \tag{2.7}$$

$$B = \mu H \tag{2.8}$$

here ϵ_0 and μ_0 are the electric permittivity and the magnetic permeability of free space. ϵ_r and μ_r are the relative permittivity and permeability of materials. In this thesis, only the case where $\mu_r = 1$ is considered.

With an applied electric field, the electric flux density can also be written as:

$$D = \varepsilon_r \varepsilon_0 E = \varepsilon_0 (1 + \varepsilon \chi_e) E = \varepsilon_0 E + P \tag{2.9}$$

χ_e is the dielectric susceptibility. P is defined as the macroscopic polarization:

$$P = \epsilon_0 \chi_e \mathbf{E}. \tag{2.10}$$

Light, as electromagnetic waves, can be written as a time-varying electric field $E(\mathrm{t}) = \mathrm{E}_0\mathrm{e}^{-\mathrm{i}\omega\mathrm{t}}$. Here, ω is the angular frequency of light, and $\mathrm{k} = \omega/\mathrm{c}$, is the wavevector of light propagating at a speed of c in vacuum. H(t) is defined in the same way. Solving the equations 2.1 to 2.4, one solution for light electric field can be:

$$\mathbf{E}(\mathrm{x},\mathrm{t}) = \mathrm{E}_0\mathrm{e}^{\mathrm{i}\mathrm{k}\cdot\mathrm{x}-\mathrm{i}\omega\mathrm{t}} \tag{2.11}$$

The optical properties of metals can be described as free electrons gas that oscillate in response to an applied electromagnetic field, i.e. the incident light. The position of free-electrons x (t) under the external electric field E can be described as:

$$\mathrm{m}[\ddot{\mathrm{x}} + \gamma\dot{\mathrm{x}} + \omega_0^2\mathrm{x}] = -\mathrm{e}\mathbf{E}(\mathrm{x},\mathrm{t}) \tag{2.12}$$

where m is the effective mass of each electron, γ is the viscous damping parameter, and ω_0 is the characteristic resonant frequency of bound electrons. For light as a time-varying electric field $\mathrm{E}_0\mathrm{e}^{-\mathrm{i}\omega\mathrm{t}}$, the solution of the above equation becomes:

$$\mathrm{x}(\mathrm{t}) = \frac{\mathrm{e}\mathbf{E}}{\mathrm{m}(\omega^2 - \omega_0^2 + \mathrm{i}\gamma\omega)} \tag{2.13}$$

Then the macroscopic polarization can be written as:

$$\mathrm{P} = -\mathrm{ex} = \frac{\mathrm{e}^2\mathbf{E}}{\mathrm{m}(\omega_0^2 - \omega^2 - \mathrm{i}\gamma\omega)} \tag{2.14}$$

If considering all the electrons in the materials, with N electrons per volume and Z electrons per molecule, and considering different binding frequencies for each electron, the macroscopic polarization becomes:

$$P = \frac{Ne^2\mathbf{E}}{m}\sum_j \frac{f_j}{(\omega_j^2-\omega^2-i\omega\gamma_j)} \tag{2.15}$$

$$\varepsilon_r(\omega) = 1 + \frac{P}{\varepsilon_0\mathbf{E}} = 1 + \frac{Ne^2}{\varepsilon_0 m}\sum_j \frac{f_j}{(\omega_j^2-\omega^2-i\omega\gamma_j)} \tag{2.16}$$

This is the general form of the Lorentz model for a material with multiple resonances. Here, f_j is the strength of each oscillator with a damping constant of γ_j and a binging frequency of ω_j. The total number of j is Z. If we do not consider the contributions from bound electrons, and assume all the electrons are the same, then the equation 2.16 turns to a simpler form:

$$\varepsilon_r(\omega) = 1 - \frac{{\omega_p}^2}{(\omega^2+i\omega\gamma)} \tag{2.17}$$

where ${\omega_p}^2 = Ne^2/\varepsilon_0 m$. This is the form of the Drude model[30], with ω_p being the bulk plasmon frequency of the metal, indicating all the free electrons are oscillating in phase at the plasma frequency. When ω changes from $\omega < \omega_p$ to $\omega > \omega_p$, the material transits from metal behavior to dielectric behavior. We can see that the $\varepsilon_r(\omega)$ has both a real and an imaginary part ($\varepsilon_r(\omega) = \varepsilon_1(\omega) + i\varepsilon_2(\omega)$):

$$\varepsilon_1(\omega) = 1 - \frac{{\omega_p}^2\tau^2}{1+\omega^2\tau^2} \tag{2.18}$$

$$\varepsilon_2(\omega) = \frac{{\omega_p}^2\tau}{\omega(1+\omega^2\tau^2)} \tag{2.19}$$

where $\tau = 1/\gamma$ substitutes γ and it is defined as the average time between collisions of free electron gas.

2.1.2 Surface plasmon polaritons and gap plasmons

For a bulk metal, $\omega = \omega_p$ describes the collective oscillations of free electrons. For a slab metal, the plasmon changes to a surface plasmon (SPs) with $\omega = \omega_p/\sqrt{2}$. For a sphere metal particle with radius r $\ll$ wavelength of the excitation light, the plasmon is called localized surface plasmon resonance (LSPR), and $\omega = \omega_p/\sqrt{3}$.

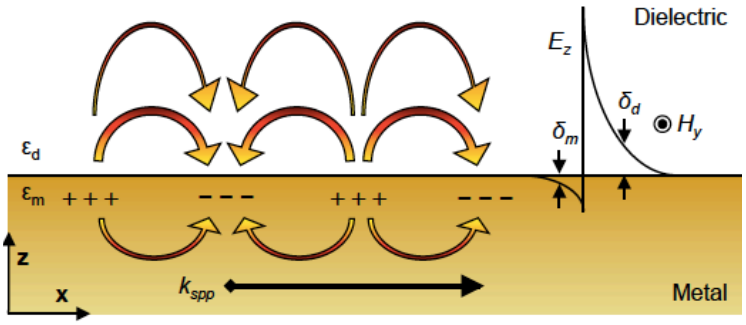

Figure 2.1 An illustration of surface plasmons (SPs). A surface plasmon is collective oscillations of the free electrons at the interface of metal and dielectric. The wave vector of the oscillation decays exponentially away from the interface. The magnetic field of the surface plasmon only has a y component. Reprinted with permission from Nathan Lindquist, et.al.[31] Copyright 2013, John Wiley and Sons.

Assuming $\omega \ll \gamma$ and $\omega < \omega_p$, $\varepsilon_r(\omega)$ is a complex number. Then k is also complex. For $k^2 = k_x^2 + k_y^2 + k_z^2 = n^2\omega^2/c^2 = 4\pi^2 n^2/\lambda^2$, in the schematic shown in Figure 2.1, surface plasmon propagates in the x and y directions, with k_x and k_y being real and k_z being complex. So the wave propagates in z direction has an evanescent component and decays exponentially into the metal and into dielectric.

TE polarized light has no electric filed component in the direction of light propagation, so it cannot excite SPs at metal/dielectric interface. Usually, a TM polarized light with an electric component $k_x \neq 0$ is needed to excite SPs. By solving the boundary conditions at the interface of metal and dielectric, we get:

$$k_{z,m}/\varepsilon_m = -k_{z,d}/\varepsilon_d \tag{2.20}$$

$$k_{x,m} = k_{x,d} = k_x \tag{2.21}$$

It can be seen from (2.20) that SPs only exist when ε_m and ε_d are opposite signs. Nobel metals such as gold and silver satisfy this condition. In the metal and in the dielectric separately, we have:

$$k_{x,m}^2 + k_{z,m}^2 = \varepsilon_m(\omega/c)^2 \tag{2.22}$$

$$k_{x,d}^2 + k_{z,d}^2 = \varepsilon_d(\omega/c)^2 \tag{2.23}$$

Solving the above two equations gives the dispersion relation of SPs:

$$k_{spp} = k_x = \frac{\omega}{c}\sqrt{\frac{\varepsilon_d \varepsilon_m}{\varepsilon_d + \varepsilon_m}} \tag{2.24}$$

In the case of two metal / dielectric interfaces, say a thin layer of dielectric is sandwiched between two metal films in the metal-insulator-metal nanogap structure as shown in Figure 2.2, the SPs at the two interfaces couple with each other. As the separation (the thickness of the dielectric layer, or the width of nanogap) of the two interfaces decreases, the two SPs waves couple with each other and split into two modes: the odd-field mode (in phase) and even-field mode (out of phase) as shown in Figure 2.2. Below a certain core thickness, the small gap between the two metal films will act as a gap plasmonic waveguide.

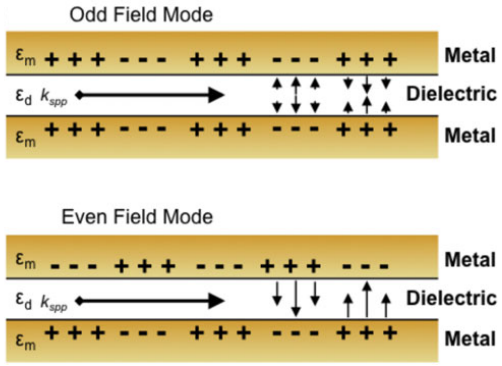

Figure 2.2 Metal-insulator-metal plasmonic waveguides. The gap plasmons have an even and an odd mode with respect to the field distribution. As the core thickness approaches the field penetration depths into the dielectric, the plasmons on both metal-dielectric interfaces will couple, forming a gap plasmon mode with a dispersion relation

that deviates significantly from a single-interface SPs. Reprinted with permission from Nathan Lindquist, et.al.[31] Copyright 2013, John Wiley and Sons.

The gap plasmons have dispersion relations that deviate significantly from the single interface SPs. The dispersion relationship of the even-field mode, which can be excited with linearly polarized plane wave illumination, is given as:

$$\tanh\left(\frac{d}{2}k_d\right) = -\frac{\varepsilon_d(\omega)k_m}{\varepsilon_m(\omega)k_d} \tag{2.25}$$

here d is the dielectric layer thickness.

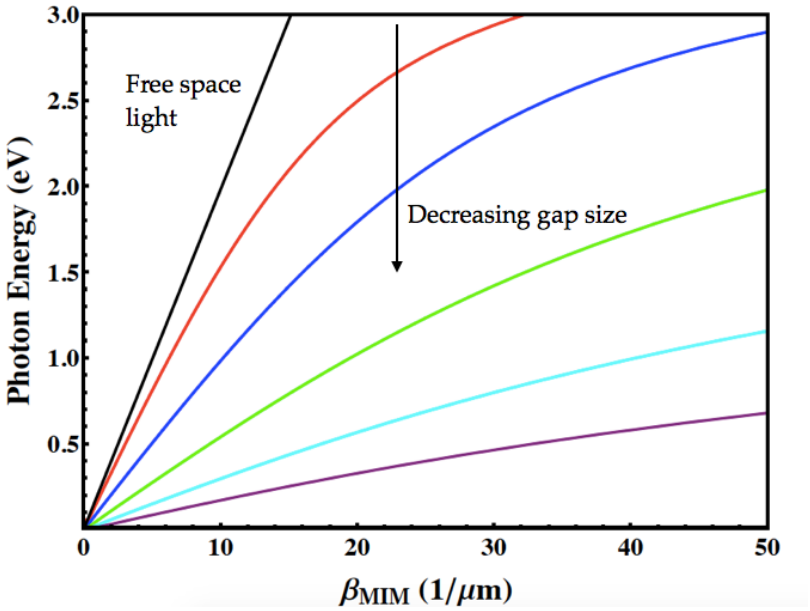

Figure 2.3 Dispersion of gap plasmon for various nanogap sizes.

From the above equation, it can be seen that the dispersion of the gap plasmon depends on the dielectric properties of the materials. Various metal and dielectric materials, which ε_m and ε_d are opposite signs, have been studied, for example, metals,

such as gold, silver, aluminum, copper, platinum etc., and dielectric, such as aluminum oxide (Al_2O_3, alumina), silicon dioxide, hafnium oxide, etc. In this thesis, I will focus on gold, silver, and alumina in nanogap structures. The dielectric functions of the metal and the dielectric layer decide the dispersion of nanogap plasmon. Using Eq. (2.25), the dispersion curves of the gap plasmon with silver and Al_2O_3 is plotted in Figure 2.3.

It also can be seen that the dispersion of the nanogap plasmon depends on the width of the nanogap. The dispersion curves for nanogap plasmon vary with different nanogap widths. As the width of the nanogap decreases, the dispersion curves move toward far lower energy comparing to the free space light dispersion curve, which indicates tighter confinement of light and higher effective refractive index.

2.2 Light-matter interactions at nano scale

Electromagnetic (EM) waves and matter interact because the charges (electrons) in the matter are pushed and pulled by the oscillations of the electric field of the EM waves. EM waves and molecules interaction is the fundamental of the infrared and Raman spectroscopy. Both Raman and infrared spectroscopy reveal similar but complementary fingerprinting information of molecules. This section is based on the descriptions given in Barbara Stuart's book[32] and in Ricardo Aroca's book[33], where the process of light

interaction with a quantum molecule is described by a semi-classical theory of quantum transitions. A coupling operator between the quantum molecule and the electromagnetic field is used to describe the interaction and it is given by

$$H = -p \cdot E \tag{2.26}$$

here p is the dipole moment. Normally, the intensity of the interaction, such as infrared absorption and Raman scattering signals, are described by interaction cross-section. The interaction cross-section is defined as the entities of molecules contained in a unite volume of the medium along the light path. It can be calculated as an average absorption / scattering coefficient divided by the number of molecules in a unite volume of the medium. Both the infrared absorption and Raman scattering have very small interaction-cross section. For example, the infrared absorption cross-section for CH_4 and CH_3CH_3 are in the order of 10^{-21} /cm^2 per molecule. Raman scattering cross-section is even smaller, usually in the order of $10^{-24} \sim 10^{-29}$/cm^2 per molecule.

2.2.1 Mid infrared absorption

Molecular vibrations and some phonon-polaritons are located in the mid infrared (MIR) regime. Therefore infrared spectroscopy is widely used to investigate the vibrational

spectra of solid, liquid, and gas species. In MIR spectroscopy, light is usually characterized by the quantity of wavenumber:

$$\tilde{\nu} = \frac{1}{\lambda} = \frac{E}{hc} \tag{2.27}$$

where λ, E, and c are the wavelength, energy, and the speed of the light, respectively.

In infrared, the dipole moment p in equation (2.26) is

$$p = \mu = \mu_0 + (\frac{\partial \mu}{\partial q})_0 q + \frac{1}{2}(\frac{\partial^2 \mu}{\partial q^2})_0 q^2 + \cdots, \tag{2.28}$$

where q is the displacement and μ_0 is the equilibrium dipole moment of the molecules. Ignoring the second and higher order derivatives of the dipole moment, the infrared absorption intensity can be written as:

$$A \propto \left|\frac{\partial \mu}{\partial q} \cdot \mathbf{E}\right|^2 = \left|\frac{\partial \mu}{\partial q}\right|^2 |\mathbf{E}|^2 \cos^2\theta \tag{2.29}$$

where $\frac{\partial \mu}{\partial q}$ is the derivative of dipole moment describes the reactions of the chemical bond to the applied electric field. The E in equation 2.29 is the local electric field that excites the molecule, and θ is the angle between $\frac{\partial \mu}{\partial q}$ and E. Therefore the absorption enhancement is proportional to the square of local E field at the metal surface or near the nano structures.

Due to the small interaction cross-section of light and nano sized molecule, the absorption of light by molecule vibrational bands is usually an extremely weak effect.

Researchers tried different schematics to enhance the interactions. Two mechanisms attribute to enhance infrared absorption of molecules at metal surface or near patterned nano structures if look at equation 2.28: the electromagnetic mechanism and the chemical mechanism. It has been demonstrated that the absorption of molecules on metal surfaces show 10-1000 times higher intensity than that from conventional measurements without metal[34,35]. This is the so-called surface enhanced infrared absorption (SEIRA). Besides using deposited metal islands as SEIRA substrate, different platforms for SEIRA have been developed: micro hole arrays fabricated using photolithography[36], nano antenna arrays fabricated with e-beam lithography[37], and nano rod dimers with a nanometer sized gap[38], etc.

2.2.2 Raman scattering

When light is scattered by molecules, the scattered light might have the same energy, or lower energy, or higher energy comparing to the energy of the incident light. The later two situations are called inelastically scattering. C. V. Raman and K.S. Krishnan first reported the inelastically scattering of light in 1928 [39]. In inelastic collisions between the incident photons and the molecules, light waves gain or loose energy by interacting with

vibrational and rotational motions of molecules. The optical scattering is now called Raman scattering named after Sir C. V. Raman.

The quantum mechanical model of Raman scattering is shown in Figure 2.4. Depending on the relative energy of the scattered light and the initial incident light, Raman scattering is categorized as stoke and anti-stoke Raman scattering. When an incident photon with energy $\hbar\omega_0$ is scattered by a molecule, the molecule absorbs a part of energy $\hbar\omega_1$ from the photon, so the scattered photon has a lower energy of $\hbar\ (\omega_0 - \omega_1)$. This process is called Stocks scattering. If the molecule emits a part of energy $\hbar\omega_1$ to the incident photon, then the scattered photon has a higher energy of $\hbar\ (\omega_0 + \omega_1)$. This process is called Anti-Stocks scattering. Usually, the possibility of the Stocks scattering is 10^7 times higher than that of the Anti-Stocks scattering. The energy $\hbar\omega_1$ is determined by the energy of vibrational and rotational motion of the chemical bond of the molecule.

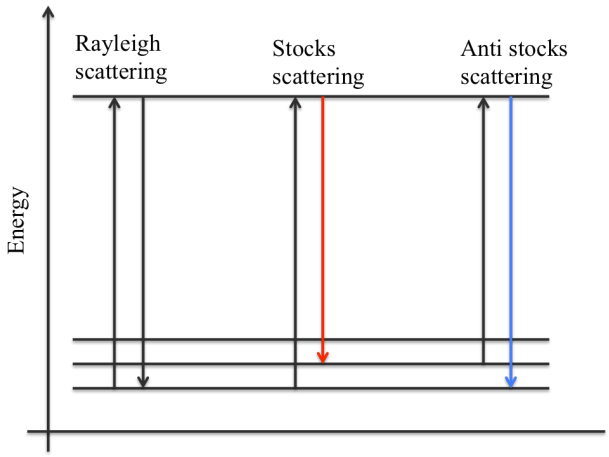

Figure 2.4 Quantum mechanical model of Raman scattering.

Typical Raman scattering peaks are known to be very sharp and unique lines that enable analysis of different chemical bonds. So Raman scattering also reveals "fingerprint" information of the molecule and is a very widely used tool to differentiate and study the chemical structures of molecules. For Raman scattering, the coupling factor of the light and matter is also described by equation (2.26), where p is the induced dipole moment and becomes:

$$p = \alpha E = \alpha_0 + (\frac{\partial \alpha}{\partial q})_0 qE + \frac{1}{2}(\frac{\partial^2 \alpha}{\partial q^2})_0 q^2 E^2 + \cdots. \quad (2.27)$$

here, α is the polarizability. Its first derivative $\alpha' = (\frac{\partial \alpha}{\partial q})_0$ is responsible for the observation of Raman scattering signal. Similarly, by ignoring the second and other higher order derivatives, Raman intensity is proportional to $|\alpha' E \cdot E|^2$. It can be seen that the Raman scattering intensity is the forth order of the local electric field and it is also

related to the chemical property of the molecule. Due to the typical ultra small interaction cross-section (10^{-29}-10^{-31} / cm^2 per molecule) of Raman scattering, enhanced local electric field from surface plasmon is normally used to enhance the interactions, which is known as surface enhanced Raman scattering (SERS). Plasmonic nano substrates, such as metal nano islands, nano tip, and nano antennas, are widely used as SERS substrates, even for single molecule detection. The SERS was first clarified by Van Duyne and Creighton independently in 1977 [40,41], and the enhancement is attributed to both the electromagnetic and chemical mechanisms, similar to those for surface enhanced infrared absorption as discussed above.

2.2.3 Measurement setups for infrared absorption and Raman scattering

Fourier transform infrared (FTIR) spectroscopy is a technique to obtain infrared spectra of absorption, reflection, and transmission of analyte. An FTIR spectrometer simultaneously collects spectral data in a wide wavelength range. This is a significant advantage over a dispersive spectrometer, which only measures intensity over a narrow range of wavelength.

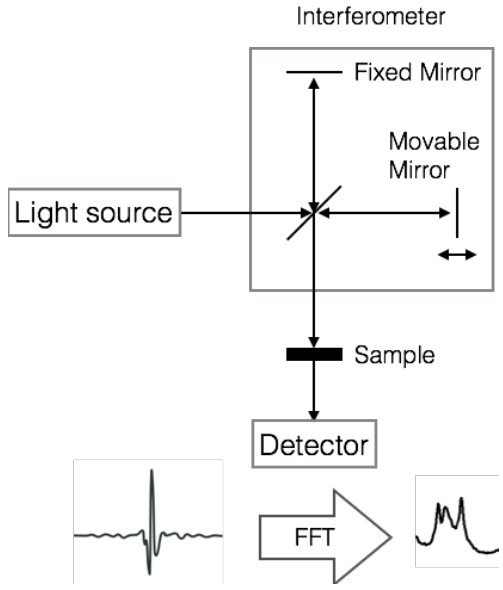

Figure 2.5 Schematic of a Fourier transform infrared spectrometer. Radiation from an IR source is guided to a beam splitter in the interferometer. After reflection from a fixed mirror and a translating mirror, both portions of the radiation interfere and a detector then detects the transmitted interferogram. A Fourier transformation of the interferogram gives an IR spectrum.

The simplest FTIR spectrometer utilizing a Michelson interferometer is shown in the above Figure 2.5 with a fixed mirror and a movable mirror. The movable mirror provides a difference between the optical paths of the two beams. For the path difference being $\left(n+\frac{1}{2}\right)\lambda$ or $n\lambda$ (n=0,1,2…), the transmitted beam and the reflected beam interfere destructively or constructively. With a polychromatic IR source, the interference pattern contains all the spectral information. The intensity signal in the time domain recorded by the detector can be transformed to an IR spectrum in the frequency domain by a

mathematical method called Fourier transformation. To obtain an FTIR spectrum from certain samples, it is necessary to produce an interference pattern without and with a sample in the beam path. Each of the spectra is transformed into a spectrum of (a) the IR spectrum without sample absorption as a reference and (b) the IR spectrum with sample absorption. The ratio of (b) to (a) gives a double-beam dispersive spectrum, which is the measurement scheme in this thesis. FTIR has two advantages over the other dispersive IR spectrometer (1) The signal to noise ratio can be improved by multiple times signal-averaging; (2) Without using a slit, the total light source output can be used to interact with the samples and thus gives a higher signals and improves signal-to-noise ratio.

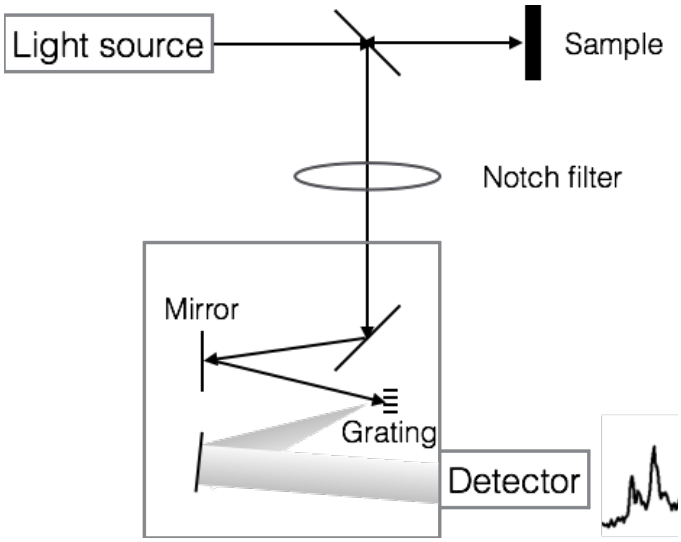

Figure 2.6 Schematic of a dispersive Raman spectrometer. The laser is first focused on the sample, and then the backscattered light is collected by an objective lens. The elastically scattered portion of the backscattered light is suppressed by a Notch filter, and

the inelastically scattered portion is guided to the spectrograph, dispersed by a grating and then detected by a charge coupled device (CCD).

A schematic light path for a dispersive Raman spectrometer is shown in Figure 2.6. The laser is first focused on the sample. Then a notch filter is used to block the elastic scattered / reflected light. The transmitted inelastically scattered light is guided to a spectrograph and dispersed by gratings and detected by a CCD camera.

CHAPTER 3

3. Atomic Layer Lithography

In this chapter, fabrication schemes for making different forms of nanogap structures in noble metals are discussed. Those nanogap structures include vertical nanogap, "U" shape buried nanogap, and planar nanogap structures.

My contributions: I designed nanogap devices, developed fabrication to make the devices in wafer scale. I performed all the fabrications and characterized the devices using scanning electron microscopy (SEM), atomic force microscopy (AFM), and transmission electron microscopy (TEM).

3.1 State-of-the-art for fabricating nanogaps

Due to the broad potential applications of metal-insulator-metal nanogap structures, various fabrication schemes have been developed, including both bottom-up and top-down fabrication methods. For example, using a bottom-up method, the gaps between self-assembled metal nano particles, can be made as narrow as sub 1 nm with very low cost[12]. However, the width and the position of the self-assembly method are not controllable, as discussed in Chapter 1. The top-down fabrication methods, such as e-

beam lithography, focused ion beam (FIB), provide precise control over the nanogap size, the pattern position, and the shape. With these tools, nanogaps as narrow as sub 5 nm are possible. However, the high cost, the long writing time, and the low yield are still the main limitations.

3.2 Vertical nanogap

To address the above challenges, I developed an atomic layer lithography method to make vertical nanogaps. The method is based on standard photolithography, atomic layer deposition and simple tape peel-off process. The details of this work are described in the following publications:

1. **Xiaoshu Chen**†, Hyeong-Ryeol Park†, Matthew Pelton, Xianji Piao, Nathan C. Lindquist, Hyungsoon Im, Yun Jung Kim, Jae Sung Ahn, Kwang Jun Ahn, Namkyoo Park, Dai-Sik Kim, and Sang-Hyun Oh, "Atomic layer lithography of wafer-scale nanogap arrays for extreme confinement of electromagnetic waves", Nature Communications, 4, 2361, 2013. †Equal contribution.
2. **Xiaoshu Chen**†, Hyeong-Ryeol Park†, Nathan C. Lindquist, Jonah Shaver, Matthew Pelton, Sang-Hyun Oh, "Squeezing Millimeter Waves through a Single, Nanometer-wide, Centimeter-long Slit", Scientific Report, 4, 6722, 2014. †Equal contribution.

3.2.1 Atomic layer deposition

In atomic layer lithography method, instead of using lithography or FIB to make the smallest feature — nano-sized gap, atomic layer deposition (ALD) is used to define the width of the gap. ALD is a thin film deposition method. Comparing to other thin film techniques, such as sputtering, evaporation, oxidation, and spin coating, ALD is uniquely suitable for the fabrication of sub-nanometer-scale structures[42,43], as its self-saturating nature enables conformal deposition of dense and uniform films on metal surfaces with atomic resolution.

A typical ALD reaction for depositing a binary compound is shown in Figure 3.1[44]. Precursors "A" and "B" are sequentially introduced into a reaction chamber with a nitrogen purging step between each precursor: A/ nitrogen purge / B / nitrogen purge. This process is called one cycle and it is repeated until the desired thickness is reached. The quality of ALD deposited thin film and the deposition rate are strongly affected by the chamber temperature, pressure, precursor mass, and the purge time.

Among various material options, the ALD process for alumina is the most extensively characterized. This process consists of the sequential injections of water vapor and trimethylaluminum (TMA) vapor into the chamber. The deposition rate of each cycle is

typically between 1 to 2 Å, making it an ideal option to deposit sub-nanometer dielectric layer.

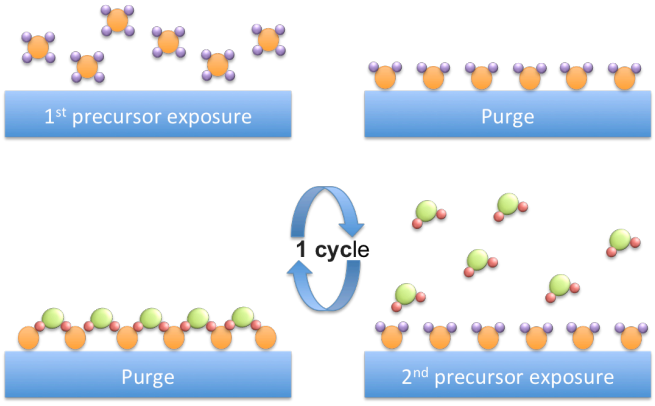

Figure 3.1 A typical reaction for a binary compound deposition using ALD. The two precursors are sequentially pumped into a reaction chamber, with a purging step in between each precursor. Each step is a self-saturation process, which guarantees the uniformity and reproduction of ALD and enables atomic resoluble thickness control by the number of deposition cycles.

The deposition rate of ALD, which is critical in defining nanogap width, is calibrated by AFM scan as shown in Figure 3.2. The calibration sample is a partially coated template-stripped ultra-smooth silver film. The left side of the ultra-smooth silver film is covered with alumina film deposited by ALD with various thicknesses on three samples (nominal thickness on each sample: 1, 2, and 5 nm). The right side is template-stripped bare silver. AFM is used to scan across the edge of the alumina film to get the height of

the step, i.e. the thickness of the alumina film. More information about ALD and the calibration sample preparation process is discussed in Appendix A.1.

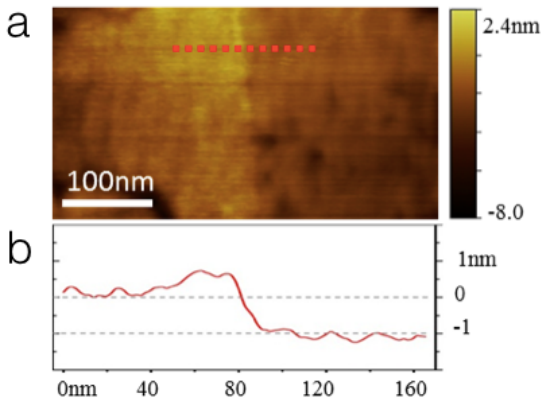

Figure 3.2 Calibration of ALD deposition rate using AFM. a, AFM scan over an area of 1 μm by 1 μm on a template-stripped silver film. The left half of the film is covered by 1 nm alumina film deposited by ALD, and the other half is bare silver. **b**, A line scan over the sample showing a step at the edge of alumina film.

3.2.2 Atomic layer lithography

Previously, ALD was combined with ion milling to pattern sub-10 nm vertical gaps along the perimeter of hollow micron-sized metal patterns[45]. As these structures are hollow, transmission measurement suffers from high background levels. This thesis therefore presents the efforts to develop a new planarization scheme that does not create a center hollow structures except the nanogaps themselves, as shown in Figure 3.3 left and right, to allow both optical and electrical study of nanogaps.

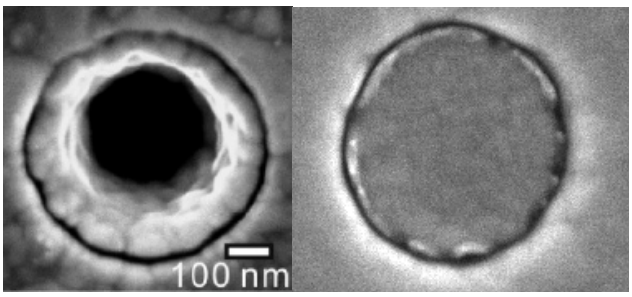

Figure 3.3 The advantage of the improved fabrication method is to be able to fill the hollow hole (left) and make nanogap in a flat surface of metal film (right). The idea is to eliminate the transmitted background signal and allow the study of nanogap alone both optically and electrically. The left figure is reprinted with permission from Hyungsoon Im, et al.[45]. Copyright 2010, American Chemical Society.

The atomic layer lithography method combines ALD with a 'plug-and-peel' metal patterning process using an adhesive tape. The processing scheme is illustrated in Figure 3.4a. First, trenches with the desired geometries are patterned in metal film on a Pyrex glass substrate using photolithography (with negative resist: NR71-1500P), e-beam lithography or FIB milling, followed by a metal deposition process using e-beam evaporation (Temescal or CHA) and then lift-off is carried out in a solvent (1165 remover) to remove the resist. After cleaning the wafer with acetone, methanol, and isopropanol (IPA) and blow dry with nitrogen gas, the patterned metal film is conformally coated with a thin alumina layer using ALD at 250 °C (Cambridge NanoTech Inc., Savannah^{TM}). If the metal is silver, then alumina is deposited with ALD

at 50 ºC to avoid the oxidation of silver. (Details of ALD recipes are discussed in Appendix A.1).

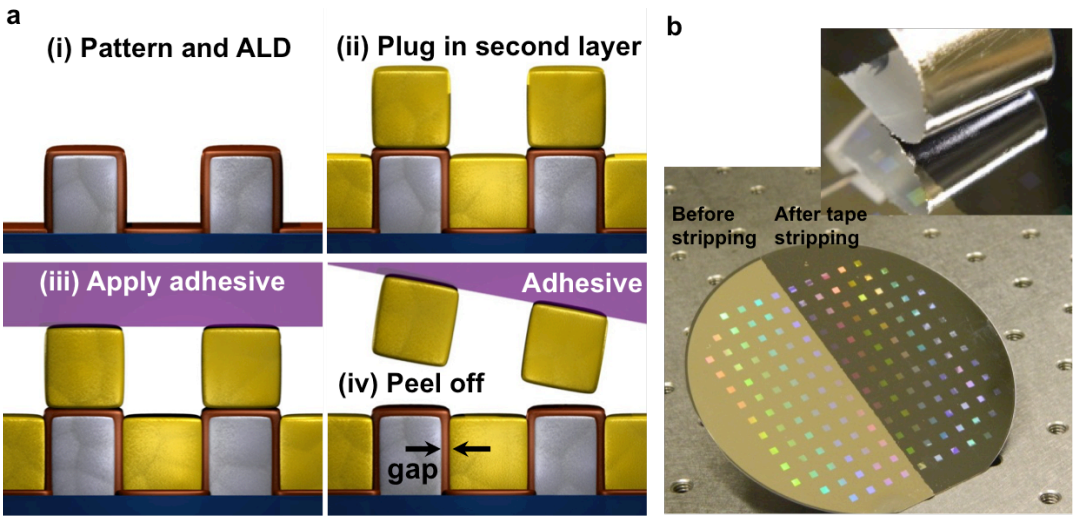

Figure 3.4 Schematic of wafer-scale atomic layer lithography. a, (i) A patterned substrate with trenches in metal film is conformally coated with a thin layer of insulator (alumina) deposited with ALD. **(ii)**, A subsequent metal evaporation embeds metal plugs in the trenches. **(iii)** and **(iv)**, Excess metal atop the substrate is removed using an adhesive. **b**, A silicon wafer with excess metal on the left of the wafer and being peeled off on the right side of the wafer. The insert on the top-right shows the tape peeling off process.

In the ALD process, TMA and H_2O vapors are sequentially pulsed through the chamber. Nitrogen gas is used to purge the chamber between each injection. The thickness of the alumina film is calibrated using ellipsometry on a Si wafer placed in the same chamber. The measured deposition rate is 1.1 Å/cycle. The trenches, now over-

coated with the alumina film, are subsequently filled with metal by directional evaporation (Temescal, the 'plug' process is shown in Figure 3.4a ii). The plug can be of a different material than the initial patterned metal. It is crucial that the sidewall of the first layer be vertical, so that there is a discontinuity between the first metal and the second metal layers. This makes it possible to peel off the metal film atop the substrate using a standard adhesive tape (single-sided 3M Scotch® Magic™ Tape), leaving behind planarized metal plugs that are isolated from the first metal film by the alumina film. As the adhesive is in contact only with the second metal layer, the process does not leave any residue on the left metal films.

Although standard lithography defines the overall footprint of the structures, the gap size is independently controlled by ALD, giving an angstrom-scale lateral resolution along the entire contour of structures. Instead of using ion mill etch, which is relative more expensive, time consuming, and causes possible surface roughness by ion bombing, the metal deposited outside of the trench is easily removed by an adhesive tape without leaving any residue or extra roughness.

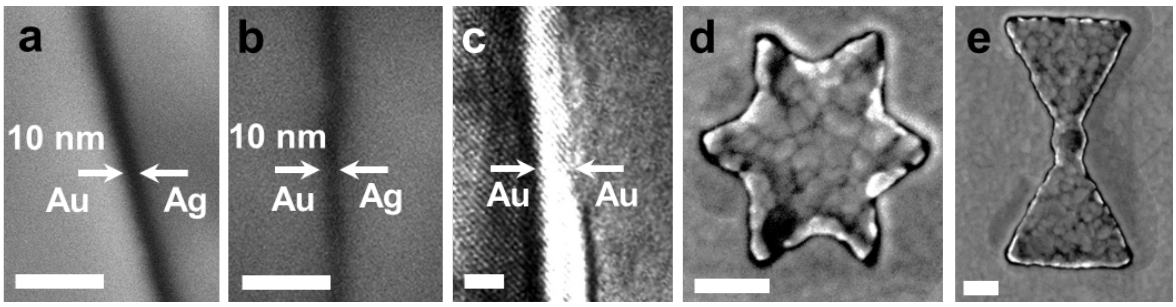

Figure 3.5 Scanning electron micrographs for nanogaps. a and **b**, top and cross-sectional SEMs of a 10-nm-wide alumina layer between Ag and Au. **c**, Cross-sectional TEM of a 9.9-Å-wide alumina layer between two Au layers. Top-view SEM of **d** star, and **e** bowtie milled with FIB in a 200 nm-thick Au film on a glass substrate. These patterns are filled with 200-nm-thick Ag plugs with 10-nm-thick alumina layer in between. Scale bars: **a**, 50 nm; **b**, 50 nm; **c**, 1 nm; **d** 300 nm; **e**, 300 nm.

To confirm that the nanogaps are formed through optically thick metal film, SEM and TEM are used to check the top surface and cross-section of the nanogap samples. Figures 3.5a and b are SEMs top and cross-section view of 10 nm thick gap formed in Ag and Au films, showing a uniform10 nm thick alumina film filled inside the nanogap. Also it can be seen that two different metals can be deposited to fabricate hybrid nanogap structures. The alumina is deposited with ALD for 9 cycles at 250 ºC at a rate of 1.1 Å/cycle, with a nominal thickness of 9.9 Å. The thickness of the alumina layer between the two metal layers is confirmed by the TEM cross-section view as shown in Figure 3.5c. Figures 3.5d and e demonstrate that nanogaps with aspect ratios over 200 can be formed along the

contours of arbitrary patterns. Even if the lateral sidewalls display some residual roughness from the initial patterning process, the conformal ALD coating ensures that the nanogaps are uniform in thickness and electrically insulated. This technique can be used to produce nanogap structures with thicknesses of less than 1 nm in opaque metal films with a yield over 90% in wafer scale. Furthermore, a particularly notable feature of the atomic layer lithography is the resulting nanogaps extend uniformly along a millimetre-scale loop, even centimeter-long loop, as shown in Figures 3.6a - d, allowing us to explore broad applications of the nanogaps.

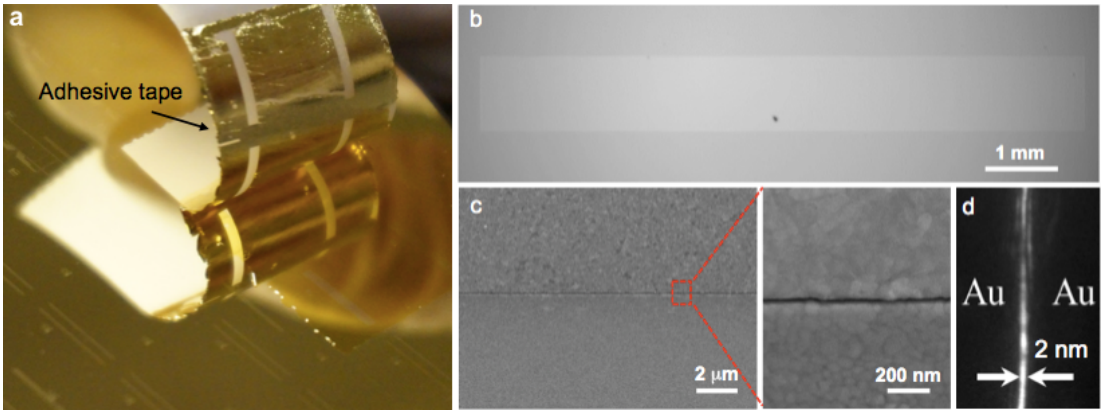

Figure 3.6 Centimeter long metal-insulator-metal nanogaps made by atomic layer lithography. a, Photograph taken from the tape peeling process for making centimeter nanogap. **b**, Photograph taken from the backside of the nanogap loop structure (0.8 cm x 1 cm). **c**, Top-view SEM of a 20 nm-wide gap in a gold film. Also shown is a zoomed in SEM image of the nanogap. **d**, Cross-sectional TEM of a 2 nm-wide alumina layer

between two gold layers. Reprinted with permission from Xiaoshu Chen, Hyeong-Ryeol Park, et.al.[47] Copyright 2015, John Wiley and Sons.

3.3 Buried nanogap

As discussed in Chapter 2, it is known that the small IR absorption cross-section of molecules is the main limitation of the applications of IR spectroscopy. Surface-plasmon-enhanced local optical field is thus widely used to enhance IR absorption of the molecules adsorbed on metallic surfaces. Various geometries such as metallic islands[48], nanorods[49, 50, 51], nanoholes[36], split rings[52], and nanoshells[15] are utilized to enhance the local electromagnetic fields. While isolated metallic structures have shown impressive performance for SEIRA, coupled nanogap structure, which takes the advantage of gap plasmons, is an ideal geometry to achieve the smallest mode volume and the maximized field enhancement. For broader applications of SEIRA, also to improve its sensitivity, reproducibility, and lessen the requirement of intense light sources, there is an increasing demand to manufacture nanogap substrates with arrays of hotspots in large area.

In the following section, a new method based on ALD and template stripping is introduced to make "U" shape buried nanogap structures as a novel SERIA substrate. The work is described in the publication:

1. **Xiaoshu Chen**, Christian Ciracì, David R. Smith, Sang-Hyun Oh, "Nanogap-enhanced Infrared Spectroscopy with Wafer-scale Arrays of Buried Plasmonic Cavities", Nano Letter, 2015, 15, 107-113. http://dx.doi.org/10.1021/nl503126s.

3.3.1 Buried nanogap structures on two dimensional substrate

Plasmonic nanogap structures have been fabricated using e-beam lithography[53, 38, 54], FIB[55, 56], electromigration[57], or nanosphere lithography[58, 59, 60]. Reproducible manufacturing of single-digit nanometer gaps, however, remains a challenge. In addition to direct-write lithography techniques, nanogaps can also be constructed via thin-film deposition[61], in which case it is not easy for light to couple into the gaps. The technical challenges have been addressed by our atomic layer lithography described in the past section. The atomic layer lithography method can be used to create single-digit-nanometer metallic nanogap structures with much higher throughput, lower cost, easier light coupling, precise positioning, and better uniformity in wafer scale for practical sensing applications.

In this section, a buried nanogap cavity device is proposed to address the above issues for applications of SEIRA. As shown in Figure 3.7 (left), the structure consists of a metal-insulator-metal waveguide flanked by vertical arms that couple normally incident

light. The cavity is made of two vertical arms and one flat section. The thickness of the insulator (purple in color) defines the nanogap size. The cavity length equals to the sum of the length of the flat and vertical parts of the nanogap. The cavity length is designed carefully to tune the resonance to the mid infrared. The insulating film in the vertical arms can be removed without compromising the mechanical stability of the cavity and then be backfilled with analyte molecules using methods such as self-assembly, drop-and-dry, and spin coating, etc.

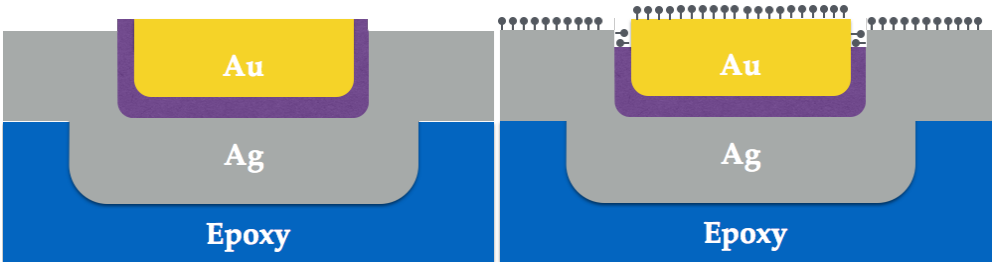

Figure 3.7 Schematic cross-section view of the buried nanogap cavity (left) and schematic of utilizing the buried nanogap as SEIRA substrate (right).

Comparing to other SERIA substrates, the buried nanogap cavity has many advantages. First, the metallic nanocavities are protected by a silicon template and a glass slide from contamination and can be template-stripped to expose nanogaps on-demand. As a dense array of single-digit-nanometer gaps can be created uniformly over an entire wafer, the technique will facilitate broader applications of surface-enhanced

spectroscopies. Furthermore, the resultant buried cavity geometry, wherein the patterned metals are tightly embedded in the surrounding metal films, is mechanically robust against wet processing. The planarized top surface facilitates subsequent integration with other devices, such as microfluidics.

Here, photolithography, atomic layer deposition, and template stripping are used to produce wafer-scale nanocavity arrays with precisely defined size, shape, and orientation. The method constructs metallic nanocavities with smooth patterned metals surfaces using template stripping[43,62, 63] , and achieves uniform strong field enhancement hotspots through precise control of the gap size using atomic layer deposition. The process flow for making the buried nanogap structure is illustrated in Figure 3.8. First, arrays of 80-nm-thick gold stripes are patterned on a 4-inch Si wafer using standard photolithography followed by a metal evaporation and a lift-off process. Note that no adhesion layer is used between the gold film and the Si substrate, which is a necessity for template stripping of the final structure. The gold stripes are then conformally coated with a thin layer of alumina using ALD (Figure 3.8b). The key advantage of this approach is that the film thickness can be readily controlled with single-digit-nanometer scale or even angstrom-scale resolution using ALD to create gaps with sub-nm thickness[46]. Then a second layer

of metal (150-nm-thick silver) is deposited on top of the alumina to form nanogaps between the gold and the silver films. The gap width is precisely defined by the thickness of ALD-grown alumina film (Figure 3. 8c).

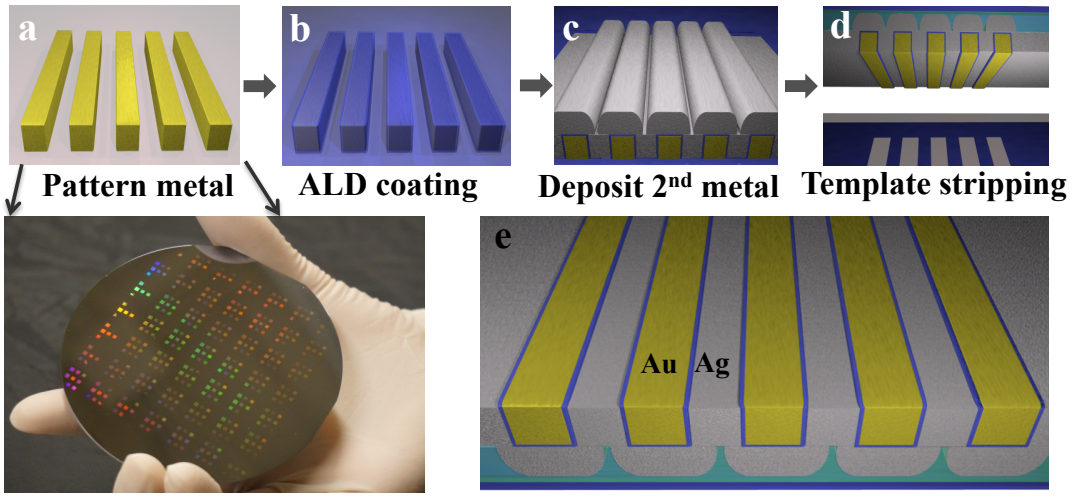

Figure 3.8 Schematic fabrication process for buried nanogaps. **a**, Standard photolithography is used to pattern gold films (stripes or disks) on a 4-inch silicon wafer. The photograph at the bottom left shows a 4-inch wafer containing metal stripes after lift-off. Each square on the wafer is approximately 1.5 mm by 1.5 mm in size, and the size is only limited by lithography. **b**, Metal patterns are conformally encapsulated with a thin alumina spacer layer deposited using ALD. **c**, A silver film is deposited conformally on the pattern. **d**, The whole structure is stripped off from the silicon substrate by gluing the substrate to a glass slide steadily with UV cured epoxy. **e**, A schematic diagram showing buried nanogaps are exposed after template stripping.

Switched between metal layer and the silicon substrate, the nanogaps are protected by metal and silicon substrate before template stripping. The sealed nanogaps are easily

exposed for molecule deposition and spectroscopic measurements. This is accomplished by stripping the patterned metals from the Si substrate due to the poor adhesion between noble metal and silicon. To carry out template stripping, a UV-curable optical adhesive (NOA 61, Norland Products Inc.) is applied on the surface of the silver film (Figure 3.8d), covered with a glass slide, cured under a UV lamp for 15 minutes and then baked on a hotplate for overnight, and at last, the whole structure is stripped off from the Si wafer (Figure 3.8e). More details can be found in Appendix A.4.

Using this method, plasmonic hotspots are generated along the entire length of the 1.5-mm long nanocavity, thus our structure is robust against local defects or impurities compared to point-like nanogap structures. Importantly, these cavities are protected by a silicon template, and can be template-stripped immediately before use to prevent surface contamination and degradation of the ultra-thin nanogaps. This is shown in Figure 3.9a that the chips are glued to glass slides by epoxy. The zoomed-in SEMs in Figure 3.9a, which are taken after template stripping, show cavities with a 5-nm gap size between gold and silver. With standard photolithography, any pattern shapes can be produced. Because the nanogaps are made entirely with wafer-scale batch processes, namely metal deposition, standard photolithography and ALD, there is no limitation in the size and

shape of the cavity patterns, such as disks (Figure 3.9b) and wedges (Figure 3.9c). The high packing density, combined with millimeter-scale horizontal length (perpendicular to the cavity length direction), facilitates applications in mid infrared.

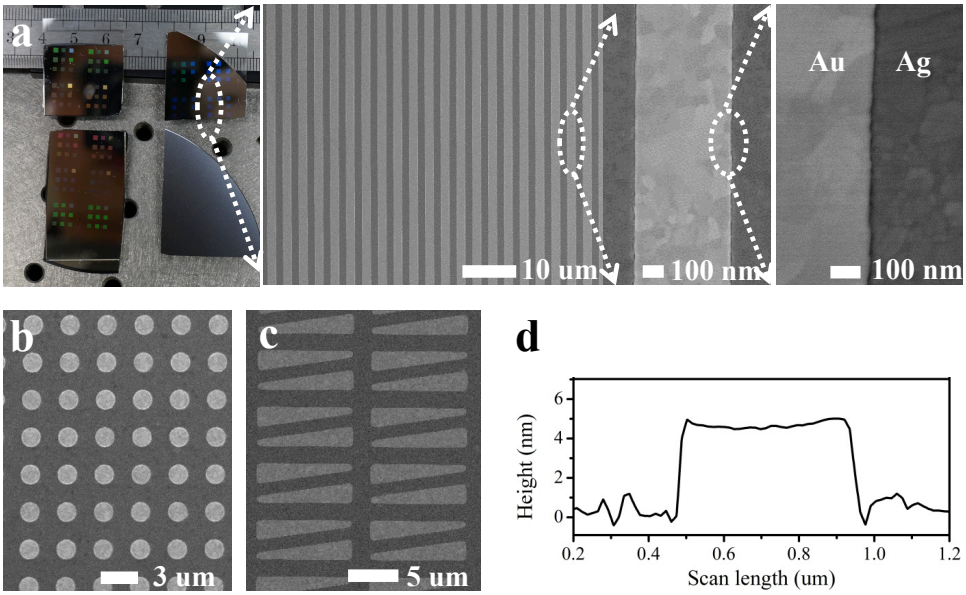

Figure 3.9 SEMs and AFM scan of buried nanogaps. a, A photograph of chips clued to a glass slide by cured epoxy. On the top right chip, the silicon substrate is already stripped off and the nanogaps are exposed. SEM image shows an array of buried nanogaps on the chip. Further zoomed-in images show a single cavity and a 5 nm nanogap on one side of the cavity. **b** and **c,** SEMs of nanogap in disk and wedge pattern. **d,** Contact mode AFM line scan across a nanogap cavity shows a height difference of 5 nm between gold and silver.

AFM is used to scan the surface of a sample with a 5-nm gap size as shown in Figure 3.9d. A line scan across the entire cavity shows the ultra smooth template-stripped gold

film, with typical root-mean-square roughness (RMS) < 1 nm, and silver film, RMS between 1 nm and 2 nm. On the template-stripped surface, it can be seen that the gold film protrudes 5 nm above the silver substrate. This height difference is the same as the thickness of the ALD deposited alumina layer. The reason for the height difference is that, during the peeling off process, the alumina film on the substrate region stays, due to the relatively stronger adhesion of alumina to silicon than that to silver.

3.3.2 Buried nanogap structures on three dimensional substrate

Nanogaps and nano tips are essential structures that can generate strong plasmonic field enhancement. Researchers have made complex structures with nanogaps on sharp tips for enhanced light field using e-beam lithography, FIB, and metal deposition into a patterned mold, etc. The hybrid structure combining nanogaps with nano tips can benefit applications such as near field optical scanning probes[64], nonlinear optics[65], and optical nano tweezers[66].

Here, a method based on atomic layer deposition and template stripping on three-dimensional substrate is introduced to fabricate nanogaps on wedges tip is introduced, as shown in Figure 3.10. First, V-shaped trenches with 54.74º are fabricated with anisotropic etching (30% potassium hydroxide (KOH) saturated with IPA at 80 °C) of a

standard (100) silicon wafer. Due to the difference in etch rates for different crystal facets of silicon crystal in KOH solution, V-shaped trenches can readily be made. The resulting sidewalls of etched silicon templates are atomically smooth.

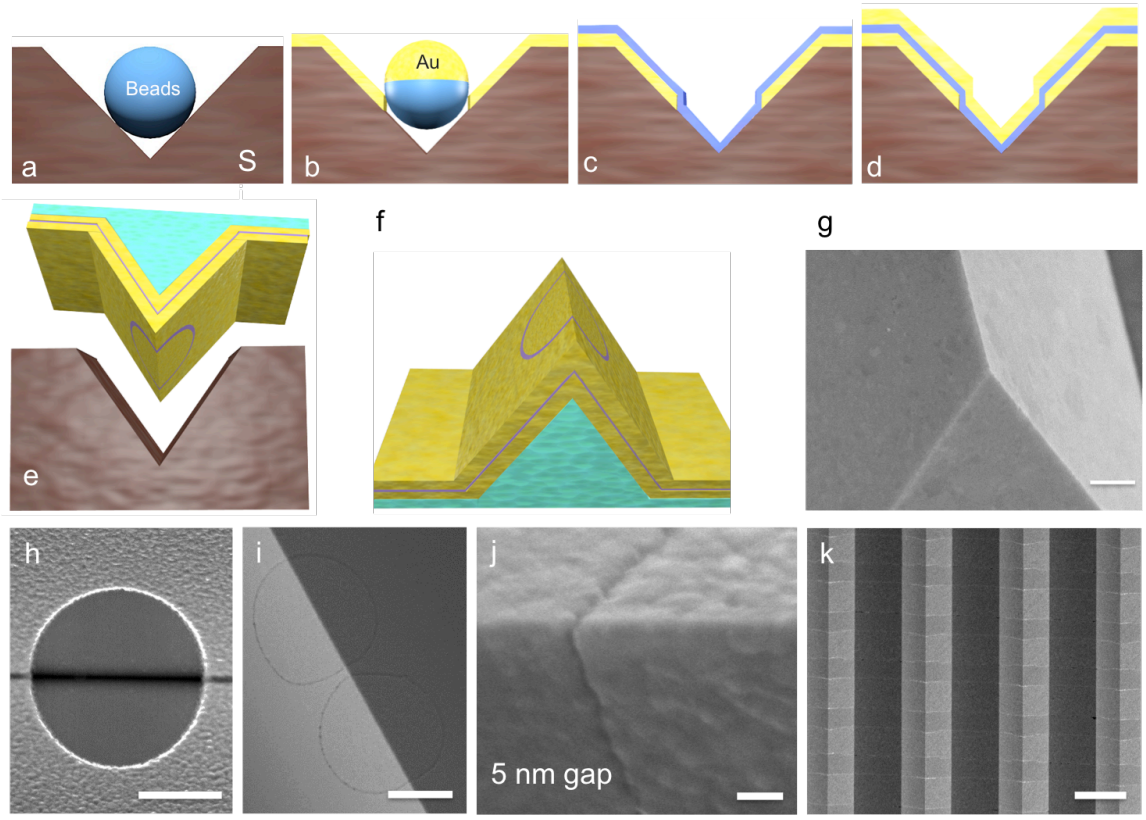

Figure 3.10 Fabrication of buried nanogaps on a template-stripped 3D wedge. a-f Schematics of the fabrication of nanogaps on wedge tips combining nanosphere lithography, atomic layer deposition, and template stripping. By putting nano / micro spheres into V shape trenches in silicon wafer as masks for metal deposition, holes in metal (in this case, silver) film inside the wedge are formed. A conformal layer of alumina is deposited by ALD to define nanogap size. Then a silver film is deposited into the wedge. The metal-insulator-metal stack layers is then stripped by glue it to a glass

slide with UV cured adhesive. **g**, SEM of a template-stripped gold wedge with the radius of about 10 nm (Scale bar 400 nm). **h**, SEM image shows a hole in metal film after removing a microsphere by sonication. **i**, Two annular nanogaps formed on the wedge. **j**, Zoomed-in SEM images showing a 5 nm gap on wedge tip. The scale bars in figures **i**, **j** are 1 μm. **k**, Nanogap array formed on the wedges, with the first metal film patterned in V shape grooves by photolithography, metal deposition, and lift-off process. The scale bar in **k** is 2 μm.

After the wedges are fabricated in silicon wafer, silica or polystyrene micro/nano spheres are applied to the wedges by drop-and-dry method. The diameter (D) of the spheres is chosen based on the width (W) of the trench. When the ratio of the W/D is smaller than 2.7 [67], isolated spheres or a linear chain of spheres are formed in the V shape trenches, as shown in Figure 3.10a. If a linear chain of spheres is formed, a dry etch method is used to shrink the size of spheres to get isolated spheres. The excess spheres on the top surface can be easily removed by a lift-off brush. Then a thin metal film (~60 nm) is deposited both on the spheres and on the silicon substrate except the areas shadowed by the spheres, as shown in Figure 3.10b. The spheres are then removed by a gentle sonication process, similar to a lift-off process, leaving holes in metal film in the wedge mold, as shown by the SEMs in Figure 3.10h. Metals with weak adhesion to silicon wafer are used in this method. Then a thin layer of alumina is deposited conformally on the

surface and sidewall of the metal patterns (Figure 3.10c). The thickness of the alumina defines the width of nanogap. A second metal layer thicker than the first metal layer is deposited on top of the alumina layer to completely cover the patterns. Then optical epoxy is poured on top of the sample surface and then cured under UV light and put on a hot plate at 55 ºC overnight for further aging. The multilayer structures, containing a layer of alumina embedded in two metal films, are stripped off from the silicon wedge mold, shown in Figure 3.10 e and f. The metal wedge is prepared by template stripping of deposited metal (silver or gold) from V shape trenches in a silicon wafer. By simple metal deposition and template stripping, 3D metal wedge structures with ultra smooth surface and ultra sharp tips are fabricated[62]. Shown in SEM in Figure 3.10i that two annular nanogaps on the wedge tip. The zoomed-in SEM in Figure 3.10j demonstrates a 5 nm wide nanogap on top of the wedge tip. The trenches in the wedge can also be made into large area and in a well-arranged array by photolithography to make nanogap array on top of wedges as shown in Figure 3.10k. More details of the fabrication process are discussed in detail in Appendix A.5.

3.4 Planar nanogap

In this section, I will demonstrate that thin film deposited by ALD can be used to make planar nanogap structures, which are also called film-coupled devices. The work is described in the following publications:

1. J. Britt Lassiter, **Xiaoshu Chen**, Xiaojun Liu, Christian Ciracì, Sang-Hyun Oh, Maiken H. Mikkelsen and David R. Smith, "Third-Harmonic Generation Enhancement by Film-Coupled Plasmonics Stripe Resonators", ACS Photonics, 1, 1212-1217, 2014. http://dx.doi.org/10.1021/ph500276v.
2. Christian Ciracì, **Xiaoshu Chen**, Jack J. Mock, Felicia McGuire, Xiaojun Liu, Sang-Hyun Oh, and David R. Smith, "Film-coupled nanoparticles by atomic layer deposition: comparison with organic spacing layers", Applied Physics Letters, 104, 023109, 2014. http://dx.doi.org/10.1063/1.4861849.

My contributions: I participated to conceptualize the idea, designed and performed the fabrication, optical measurement, SEM imaging.

3.4.1 Background of planar nanogap

Comparing to vertical nanogaps, the planar nanogaps are easier to fabricate, with dispersed plasmonic nanoparticles (NPs), thin film deposition, e-beam and optical lithography method. NPs can be readily positioned at controlled distances from a metal film with a uniform dielectric spacer layer in between. A NP closes to a metal film and its

electromagnetic image in the metal film are resemble to a dimer configuration in optical properties. Such film-coupled devices have been utilized to enhance Raman scattering[68], to control the reflectivity from surfaces in visible regime[69], to control the spontaneous emission of fluorescent molecules[70], and to study the classical nonlocality effect in the sub-nanometer gap regime[11].

3.4.2 Fabrication process

In this section, two methods are introduced to make planar nanogap structures. The first method is to deposit colloidal NPs on a thin dielectric film coated on gold film. The second method is to use e-beam lithography to make well-arranged planar nanogaps between the first metal film and the patterned metal film. The project of film coupled planar nanogap was collaboration between our group and Dr. Smith's group at Duke University. More details are in references[71,72].

In both methods, a spacer layer is used between the metal film and metal NPs or patterned metal films. As shown in Figure 3.11, the colloidal synthesized plasmonic NPs are deposited on a spacer layer comprising of organic molecules, such as polyelectrolyte layers (PEs) or self-assembled amine-thiol monolayers. The spacer layer can be prepared by spin coating or self-assembly. Organic layers sometimes form fragmentarily when

deposited on the film surface, require long-term immersion during formation, and may break down under high temperature and high laser power. Therefore, it is interesting to explore alternative spacer layer based on inorganic systems.[73]

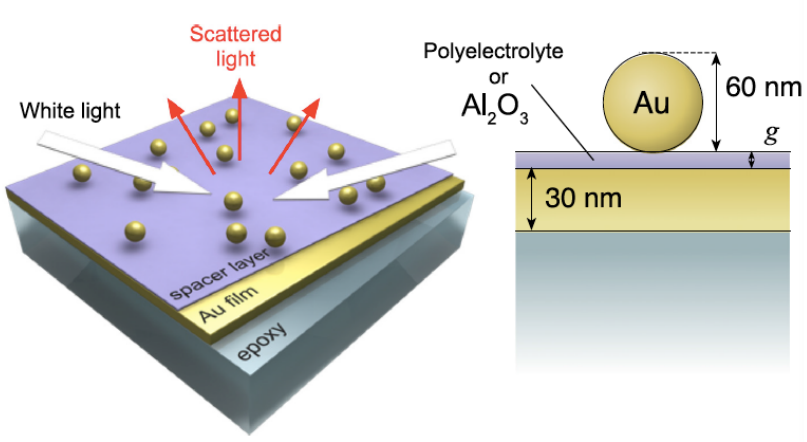

Figure 3.11 Geometry of film-coupled NPs structure. Gold NPs are randomly distributed on a metal substrate through a dielectric spacer layer. Reprinted with permission from Christian Ciracì, Xiaoshu Chen, et.al.[71] Copyright 2014, AIP Publishing LLC.

One robust method to the fabrication of thin inorganic spacer layers is using ALD, which utilizes alternative cycles of self-limiting surface reactions to deposit angstrom scale thin films in a layer-by-layer fashion.[74] Besides its traditional applications in microelectronics, ALD has recently been used for surface passivation[42] as well as lithographic patterning of plasmonic nanostructures[46].

The fabrication process of using e-beam lithogprahy to make the planar gaps is shown in Figure 3.12. First, the ultra smooth gold pattern is prepared by the template stripping fabrication method[62]. In the template stripping process, the gold film is peeled off readily using optical adhesive as a backing layer to reveal the smooth gold surface replicated from the atomic smooth silicon surface. The measured RMS of the template-stripped gold film is 0.33nm measured by AFM, while the typical RMS for deposited gold film is above 1 nm. The dielectric functions associated with these films differ slightly from standard evaporated gold films[69]. In the spectral range of interest, the real and imaginary parts can differ up to 5% and 17%, respectively.

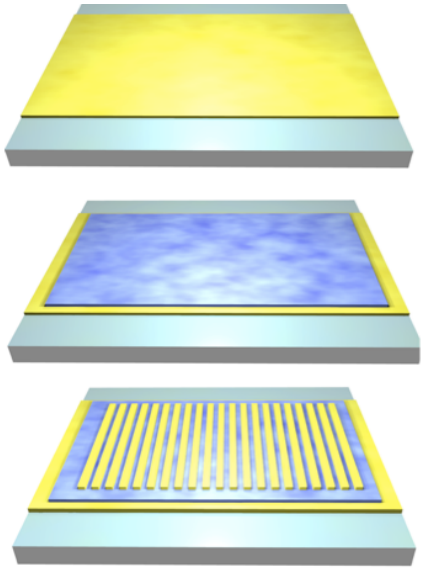

Figure 3.12 Schematics of the fabrication process for planar nanogap arrays. a, A ultra-smooth gold film is prepared by template stripping process. **b**, A thin alumina film

is deposited by ALD. **c**, Gold stripes are patterned with e-beam lithography, metal deposition and lift-off process.

One set of samples is fabricated on template-stripped gold films, with alumina inorganic spacer layers of thicknesses, d, varying from sub 1 nm to a few tens of nanometers. Alumina spacers are deposited by ALD at 50 ºC. The thicknesses of alumina can be deduced by multiplying the number of cycles (self-limiting cycles which are deposited) for each sample times the deposition rate. The calibrated deposition rate is 1.0 Å per cycle, which is confirmed by ellipsometry measurements on test wafers.

3.5 Conclusions

In this chapter, we presented novel fabrication methods to make different forms of metal-insulator-metal nanogap structures, based on standard photolithography, ALD, and adhesive tape or template stripping method. Those methods enable wafer-scale production of 1-nm nanogap arrays containing approximately hundreds of thousands devices at the same time. ALD pushes the gap dimension towards the angstrom scale and thus can boost the wafer-scale investigation of quantum-mechanical and nonlocal effects at optical frequencies[11], optical rectification[24,29], and inelastic electron tunneling excitation of plasmons[7]. Also by combining with the template stripping method, the

hotspots of each nanocavity uniformly extend along millimeter-long lines. Furthermore, the substrates are robust against localized defects or contaminants, which will help to accomplish more reproducible spectroscopy and also the combination of SERS and SEIRA on the same substrate.[75] As with other template-stripped metallic nanostructures,[76] the surfaces of these nanogap cavities are initially protected by a silicon template, which provides a robust protection mechanism against contamination or degradation, and thus each chip can be stored for a long time and template-stripped on-demand. Since two metal films are electrically isolated by an insulating layer in between, applying a bias across the gap can turn these structures into tunnel junctions. Such structures can be used to study interesting effects such as electron tunneling,[77] nonlocal electrodynamics,[11] and photodetection[78].

CHAPTER 4

4. Optical Characterization and Discussions

Optical characterization of nanogap structures in the visible, near infrared, mid infrared, and THz regime will be discussed in this chapter. The optical characterization of the nanogap structures is used to confirm nanogap size, to map gap plasmon resonance, and to figure out gap plasmon resonances for desired applications. The work presented in this chapter can be referred to publications 1 and 3 (visible and near IR), 2 (mid IR), 3-6 (THz waves), 7-8 (near IR) in the publication list.

My contributions: I performed optical characterization in the visible, near infrared, and mid infrared and performed data analysis.

4.1 Characterization at visible and near IR

4.1.1 Visible and near-infrared optical spectroscopy

To prove that uniform nanogaps are formed through the entire metal film thickness, it is straightforward to measure the transmission of light simultaneously through an array of nanogaps in optical thick metal film simply by imaging the sample under a white-light illumination in an optical microscope. For transmission measurements at visible

wavelengths, a Nikon Eclipse inverted microscope, a Newport MS257 imaging spectrometer, and a Princeton Pixis 400 CCD camera are used. Each spectrum is measured through a single gap and averaged over the length of the gap. Repeatable spectra are obtained from different gaps on the same samples. Spectra are normalized to the illumination source. A background spectrum is subtracted from all measured spectra. Nanogap samples for optical transmission measurements are made using standard photolithography (except the spectrum for 2 nm gap in Au film in Figure 4.2b, which is taken from a sample that the trenches are made with FIB).

Similarly, in the transmission measurements at near infrared (NIR) wavelengths, nanogaps are illuminated with an unfiltered halogen lamp through a condenser on an Olympus IX71 inverted microscope. The transmitted light is collected with an Olympus LMPlan IR 100X objective lens and then imaged on the entrance slit of an Acton SP2300 grating spectrometer. The spectrometer is equipped with a liquid-N_2-cooled OMA V InGaAs focal-plane photodiode array (Princeton Instruments).

4.1.2 Results and discussions

In the vertically oriented nanogap configuration, the nanogaps act as waveguides, and only the lowest-order transverse-magnetic mode in the waveguide is excited. This mode

is excited only by light polarized perpendicularly to the gap, which is verified experimentally (Figure 4.1a). It can be seen that the random polarized incident light transmits through the whole range of nanogaps (Figure 4.1a row 1), while the linear polarized incident light only transmits through nanogaps that are perpendicular to the polarization of the light (Figure 4.1a row 2 and 3). This observation is consistent with the expected behavior of gap plasmons.

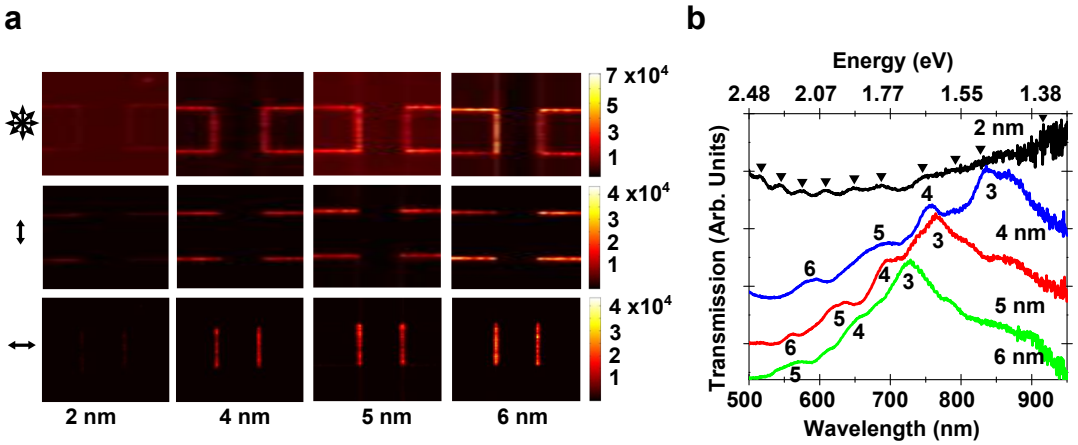

Figure 4.1 Transmission of visible light through nanogaps. a, Optical micrograph of white-light transmission through alumina-filled nanogaps (Gap sizes: 2, 4, 5, and 6 nm for each column) in two adjacent rectangle nanogaps in 190-nm-thick Ag films. The illumination light is polarized randomly (row 1), vertically (row 2) and horizontally (row 3). The widths of the gaps are indicated below each column. The color scale bars on the right show charge-coupled device counts. **b**, Measured transmission spectra through single nanogaps with different gap sizes in Ag at visible wavelengths. Numbers in **b** are the mode orders of FP resonances in the nanogap waveguides. Triangles in **b** indicate FP

resonance positions for 2-nm gaps. Spectra from 2, 4, 5, and 6 nm gaps in **b** are offset vertically for ease of comparison.

The transmission spectra measured from single nanogap geometry with four different gap sizes are shown in Figure 4.1b. Multiple resonances are observed in the visible regime. The relatively low Q factor of the resonance is due to the loss in the metal when the gap plasmons propagate and reflect back and forth inside the ultra thin nanogap for multiple times.

The spectra of light transmitted through the nanogaps show a series of peaks at both visible (Figure 4.1a and b) and near-infrared wavelengths (Figure 4.2a and b). These resonances are Fabry-Pérot (FP) resonances[79,80]: light that travels in the nanogap waveguide is partially reflected at the upper and lower surfaces of the nanogap cavity, forming a standing wave. The resonant wavelength is determined by cavity length, the nanogap width, and the effective refractive index of the cavity, etc. The resonances occur when the following condition is satisfied:

$$\left|2L_{\beta_{MIM}}(\omega) + \Delta\varphi_1 + +\Delta\varphi_2\right| = 2\pi m \qquad (4.1)$$

where β_{MIM} is the gap plasmon propagation constant in the metal-insulator-metal waveguide. m is an integer indicating FP mode number, and $\Delta\varphi_{1,2}$ describe the phase shifts due to reflection at the two end faces of the cavity.

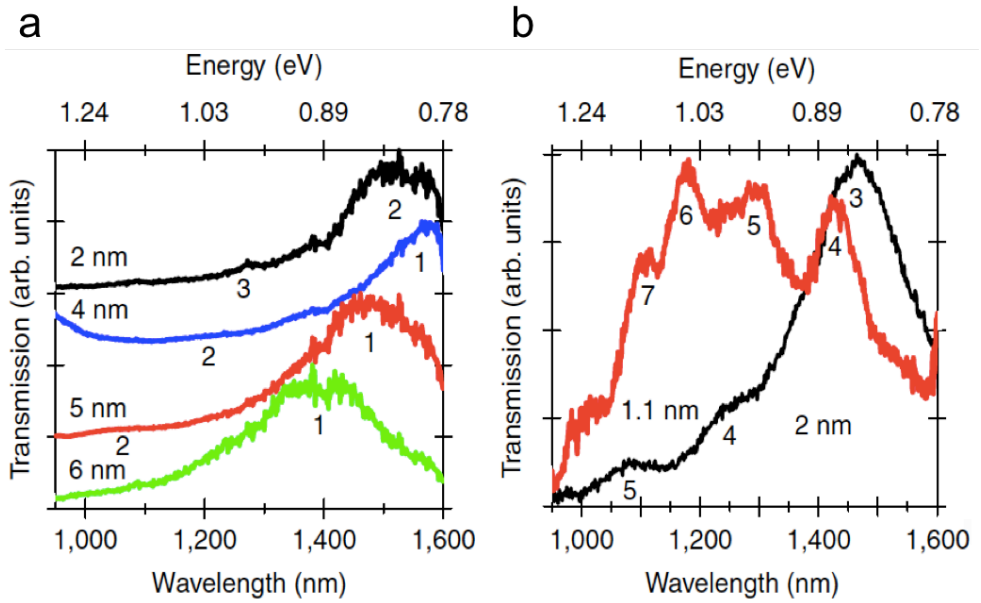

Figure 4.2 Transmission of infrared waves through nanogaps. a, Measured transmission spectra through nanogaps in Ag film at NIR wavelengths. Spectra from 2, 4, 5, and 6 nm gaps in **a** are offset vertically for ease of comparison. **b**, Measured transmission spectra at NIR wavelengths through a 1.1-nm gap in a 190-nm-thick Au film and a 2-nm gap in a 200-nm-thick Au film. Numbers are the mode orders of FP resonances in the nanogap waveguides.

In order to obtain a simple analytical model, we ignore the above mentioned phase shifts, which are expected to be small due to the large effective refractive index mismatch between the waveguide and the free space (air and glass in this case). We then use the

equation (4.1) to map out the dispersion relation of the gap plasmon in nanogap waveguides, provided that we know the mode number, m, corresponding to a given transmission peak. The mode number is determined by comparing the measured data to FDTD simulations, and the resonance peak positions are obtained by fitting Lorentzian curves to the measured spectra.

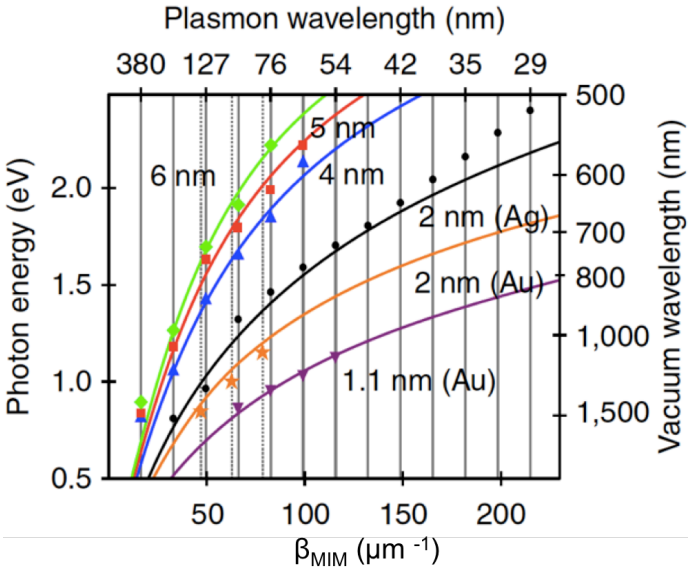

Figure 4.3 Dispersion relations of gap plasmon resonances in nanogaps. The solid curves are theoretical dispersion curves for different gap sizes and materials. The markers are measured resonance peaks from nanogap waveguides from Figure 4.1b, 4.2a and b. The vertical solid grey grid lines denote the wavenumbers of modes 1–13, from left to right, for a cavity length of 190 nm. The vertical dashed gray grids mark the wavenumbers of modes 3, 4, and 5 for a cavity length of 200 nm. The bottom x-axis is the wave vector of gap plasmon. The top x-axis, defined as $2\pi/\beta_{MIM}$, is the gap plasmon

wavelength. The left y-axis is the energy of light, with corresponded free space wavelength showing at right y-axis.

As shown in Figure 4.3, experimental data of the peak positions from the nanogaps in Au and Ag film (Figure 4.1 and 4.2) are in good agreement with the theoretical dispersion relations. Deviations for large wavenumbers may be due to the neglect of the phase shifts upon reflection, or due to errors or variations in the measured thickness of the metal film. The dispersion curves indicate that light with a free-space wavelength of 517 nm is confined to a 2-nm alumina gap in Ag, referring a plasmon wavelength λ_{spp}= 29 nm; this corresponds to an effective refractive index of 17.8, the highest effective refractive index reported in the visible regime.

4.2 Characterization in mid infrared regime

Buried "U" shape nanogaps are designed to have resonances in the mid infrared for applications as SEIRA substrate. The optical characterization is carried out with a Fourier transform infrared spectroscopy (FTIR) as discussed in Chapter 2.

4.2.1 FTIR measurements

A Nicolet Series II Magna-IR System 750 FTIR equipped with an IR microscope (15× IR objective lens, NA = 0.58) is used to measure the spectra from the nanogap samples in reflection mode. Though the spectrometer and the microscope are purged with dry air, the sample and the light path from the objective lens to the sample are exposed in atmosphere. An adjustable built-in aperture in the IR microscope is used to define the illumination spot size. The absorbance spectrum is defined as $Log_{10}(I_o/I)$, where I_o is the reference signal and I is the signal from nanogap cavities. Each spectrum from the nanogap cavity array is normalized to the signal taken from an area of bare silver hundred of microns away from the patterned area using the same aperture size and is averaged for 256 times, with a resolution of 4 cm^{-1} in each spectrum.

4.2.2 Results and discussions

We measured the absorbance spectra from nanogap cavities with lengths of 500, 600, 700, 900, 1300, and 1700 nm, each with gap sizes of 3, 5, 7, and 10 nm. The thickness of the first layer gold film is fixed at 80 nm for all the samples. Buried nanogap cavities with different cavities length are shown in SEMs in Figure 4.4.

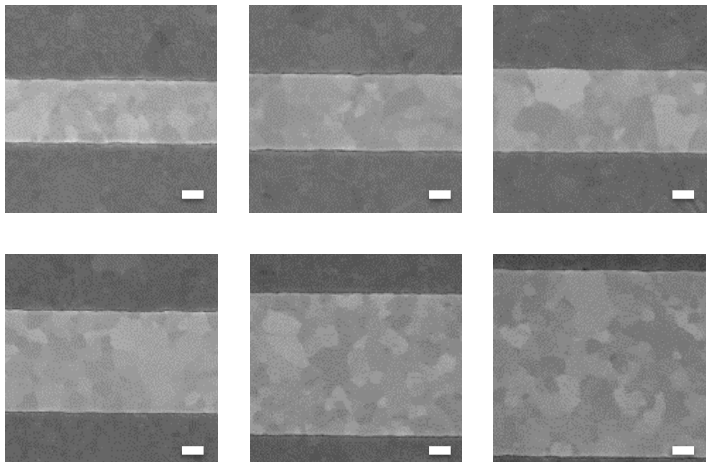

Figure 4.4 SEMs of buried nanogap cavities with various cavity lengths. Scale bar: 200 nm.

Corresponding spectra for different gap sizes and cavity length are shown in Figure 4.5a-d. Multiple FP resonances are observed at wavelengths between 10 μm and 1.6 μm. The peaks observed in the spectra shown in Figure 4.5a-d correspond to the FP resonances in the buried nanogap cavities[22,81]. While each cavity is folded, the gap plasmon follows the dispersion as if it is propagating in an unfolded nanogap cavity.[82] Although we use random polarized light to launch gap plasmon modes in our structures, only the TM component (electric field perpendicular to the stripes) couples to the gap-plasmon mode in the nanogap cavities. Moreover, with normally incident light, only symmetric FP modes (with respect to the magnetic field) can be excited. The first left peak from buried nanogap cavities shown in Figure 4.5 is the first symmetric FP mode. In

our experiments, anti-symmetric modes are also observed as small peaks between much stronger resonance peaks associated with symmetric modes. This is because the incident light is not perfectly collimated due to the numerical aperture (=0.58) of the IR objective lens, which allows certain amount of oblique incident light.

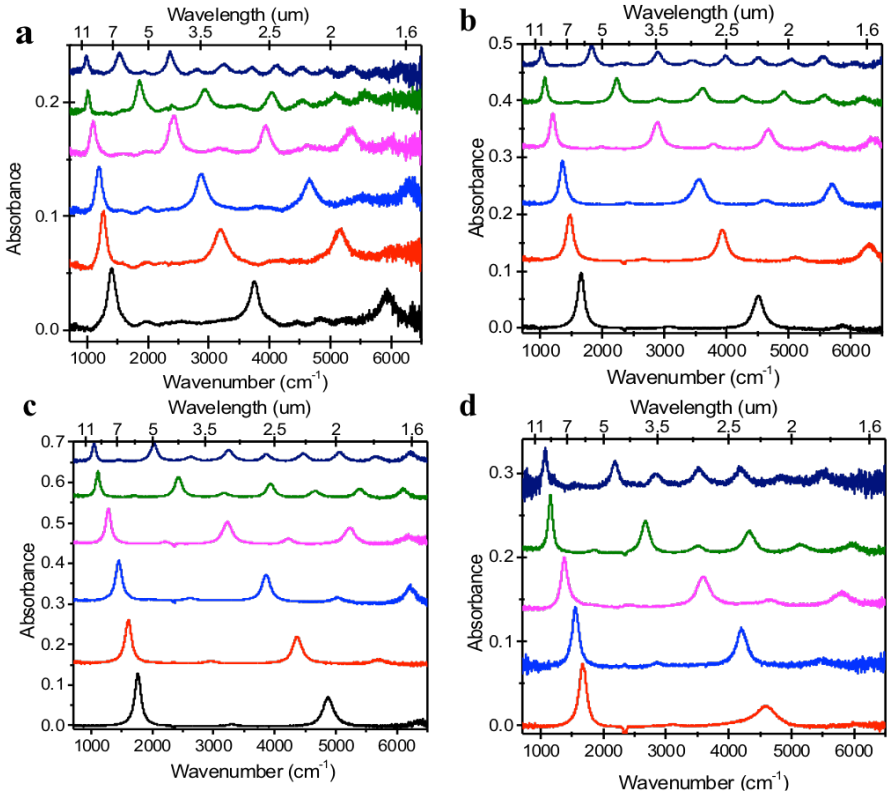

Figure 4.5 Tuning of resonances of nanogaps by varying cavity width. a-d, FTIR spectra from 3, 5, 7, and 10 nm gap cavity respectively, in 2D stripe pattern with various metal stripe widths: 500, 600, 700, 900, 1300, and 1700 nm, from the top curve to the bottom curve. Except in d, the spectra are measured from 600, 700, 900, 1300, and 1700 nm cavity width. Spectra are offset in y-axis for easier comparison.

The spectral scaling can be simply achieved by tuning cavity length or the gap thickness of the nanogap cavity. Increasing the cavity length shifts the FP modes toward longer wavelengths. With micron-scale cavity lengths, which are fabricated using standard photolithography, the cavity resonances are tuned from mid-infrared to near infrared easily.

Figure 4.6a shows a reflection spectrum obtained from 5-nm gap cavities, plotted as a function of wavelength, which shows a series of sharp resonances peaks. A Q factor – defined as $\lambda_{resonance} / \Delta\lambda$ – of 34 is measured at a resonance wavelength of 1.8 μm. For decreasing gap thickness, the resonance shifts toward longer wavelengths because of the dispersion of the gap-plasmon[69]. That is, as the gap width shrinks, the effective refractive index of the tightly confined plasmonic mode goes up, thus increasing the effective cavity length and the resonant wavelength.

The dispersion characteristics of the buried nanogap plasmon for the gap sizes of 3, 5, 7, and 10 nm are deducted from resonance peak positions, as shown in Figure 4.6b. The theoretical plasmon dispersion curves are plotted using gap plasmon dispersion equation. The dielectric function of alumina and template-stripped gold film are taken from peer's work respectively[83,84], and the dielectric function of silver is approximated by the Drude

model. The results from both theory and experimental data are in good agreement. For 3 and 5 nm gaps, the experimental data deviate toward shorter wavelengths compared to theoretical predictions, likely due to the roughness of the metal surface in the nanogap. For the 3 nm gaps, we find an effective refractive index of 6.5 for the waveguide plasmon mode. The resonance peak measured at 10.16 μm wavelength from this sample indicates that the free-space radiation has been squeezed into a cavity as narrow as 3 nm (λ/3387), showing the strong optical confinement enabled by the nanogaps.

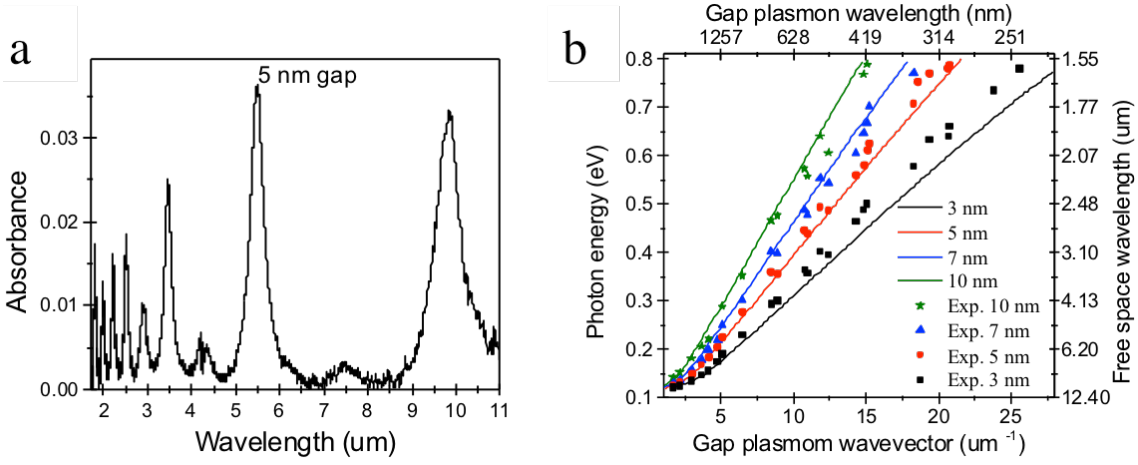

Figure 4.6 Gap plasmon dispersion in mid infrared. a, FTIR spectra from a 5-nm gap cavity with cavity width 1700 nm, plotted in wavelength. **b**, Dispersion of nanogap from experimental and simulation data for 3, 5, 7, and 10 nm gap. The solid lines are the theoretical dispersion curve of gap plasmon in nanogap cavity for different cavity lengths and gap sizes.

It is interesting to notice that the spectra in near infrared regime show very distinct peak resonances, which indicates good coupling between the gap plasmon and the far-field modes. This coupling is quite remarkable for a structure consisting of bare metal for more than 99.5% of its topographically flat surface. The strong coupling can be understood intuitively by replacing the fields radiated by the slits (formed by the vertical arms of the waveguide) with effective magnetic currents that re-emit a wave whose fields have opposite phase with the scattered wave reflecting off the metal region. The resultant destructive interference reduces the total reflected fields, greatly enhancing the energy absorbed from the incident wave[69,85].

4.3 Characterization in THz waves regime

4.3.1 THz waves and time domain spectroscopy

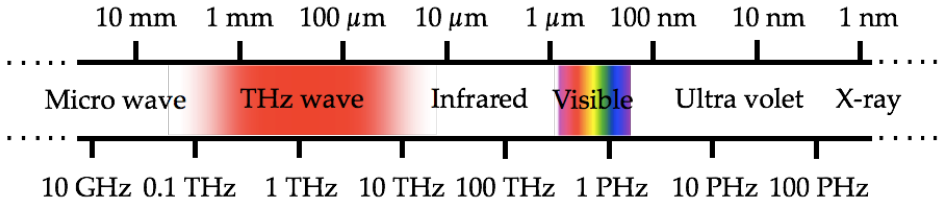

Figure 4.7 Terahertz (THz) waves.

THz waves are the electromagnetic waves loosely defined within the band of frequencies from 0.05 THz to 3 THz (1 THz = 10^{12} Hz), as shown in Figure 4.7. The wavelength of

THz waves ranges from 6 mm to 100 μm. THz waves used to be known as the THz "gap", due to the difficulties of the generation and the detection of THz waves.

In the past two decades, there are plenty of progresses in the studies and applications of THz waves. Many applications, such as medical imaging[86], security[87,88], communications[89], manufacturing[90], and food safety[91], are made possible with the emerging of more efficient THz generation and detection techniques.

4.3.2 THz waves transmission through a single centimeter long nanogap

THz time-domain spectroscopy (TDS) is a spectroscopic technique that is widely used to study the properties of the materials in THz waves[92,93]. A typical TDS system is shown in Figure 4.8.

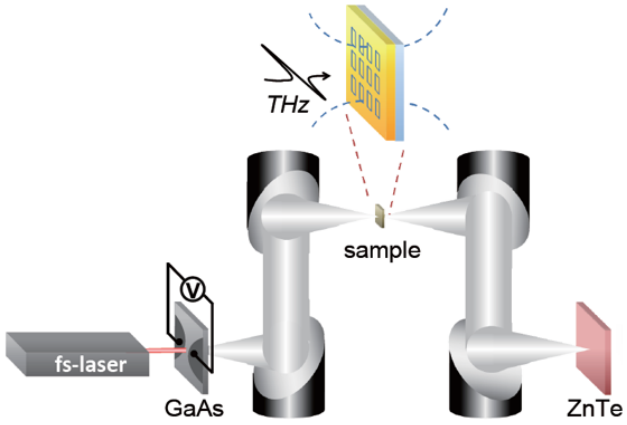

Figure 4.8 THz time-domain spectroscopy system (THz-TDS).

In our TDS system, which was built by a lab member, Hyeong-Ryeol Park, a THz pulse with a few picoseconds pulse width is generated from a GaAs-based photoconductive antenna (Tera-SED, Gigaoptics, GmbH) illuminated by a femtosecond Ti: sapphire laser pulse train with a center wavelength of 780 nm, 80 MHz repetition rate, and 90 femtosecond pulse width (Mai Tai XF, Newport Corporation). As shown in Figure 4.8, the terahertz waves normally illuminate the sample. The transmitted THz pulses through the samples are detected by an electro-optic sampling method using a 1-mm-thick ZnTe crystal (INGCRYS Laser System Ltd.).

THz-TDS has been performed to observe non-resonant transmission of THz waves through tens of nanometer-sized gaps or slits[21,94] fabricated in metal film. In this work, THz waves transmit through even narrower nano gaps in a 150 nm-thick gold film with gap sizes of w = 2, 5, 10, and 20 nm, to achieve even higher field enhancement. The nanogap samples are prepared as shown in Figure 3.6a and b. During THz transmission measurement, a 1 mm-by-1 mm aperture in a stainless steel plate (1 mm in thickness) is used to illuminate only one side of the loop (that is, a single, straight nano sized gap) with the incident THz waves. A small but non-negligible direct transmission of THz waves through the unpatterned gold film is subtracted as background when estimating the field

enhancement in the nanogap[21]. Figure 4.9a shows the transmitted electric field amplitudes through the nanogap samples and the unpatterned gold film on the glass substrate. The transmission is highly broadband without any cut-off or interference effects, and is limited only by the response frequency of the metal.

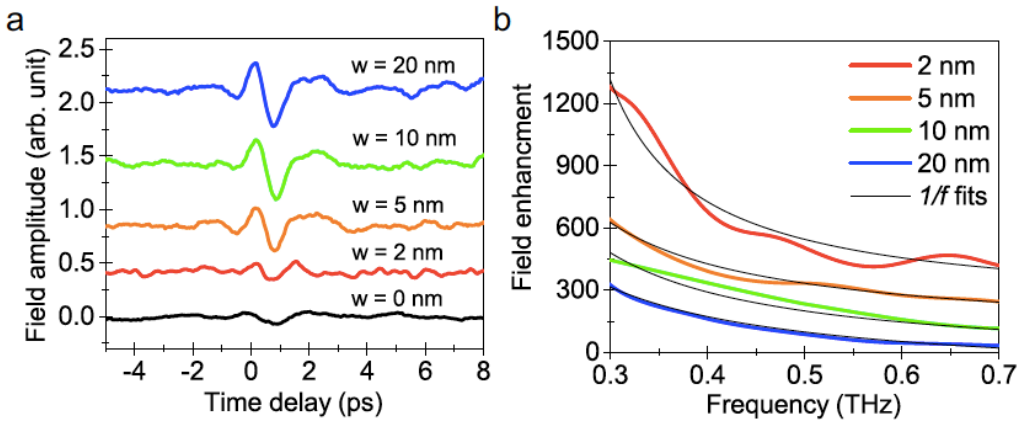

Figure 4.9 Transmission of THz waves through a single metal-insulator-metal nano gap. a, Time-domain signals for transmitted THz waves through single nanogap with gap sizes, w = 20, 10, 5, 2, and 0 nm(unpatterned). The graphs are offset along the vertical axis. **b**, Fourier-transformed electric-field enhancement spectra of the nanogap in the frequency domain. Black lines indicate a1/f dependence.

Transmitted electric field amplitude is obtained by Fourier-transforming of the time-domain signals, which is then normalized to the reference signal collected from the transmission through glass substrate. We infer near-field enhancement factors by normalizing the transmitted amplitudes by the gap coverage ratio, according to Kirchhoff

diffraction theory[21,95]. This can be done because the minimum gap width of 2 nm is larger than the charge screening length (usually about 1 nm). Figure 4.9b shows that the enhancement varies approximately as 1/f, where f is frequency, over the entire measured spectral range. Previous work showed that the field enhancement increases as the slit width decreases down to tens of nanometers, due to capacitive charge accumulation from the light induced currents at the sidewalls[96-98]. Reducing the gap width to 2 nm allows us to achieve a non-resonant electric field (|E|) enhancement of 1300 at f = 0.3 THz, which corresponds to a maximum intensity ($|E|^2$) enhancement of 10^6, the highest obtained in single-nanogap studies. This enhancement is entirely due to the large ratio between the free-space wavelength of the THz wave and the narrow gap width, and does not rely on any resonance effects.

When the nanogaps are irradiated with THz waves, the induced current charges the capacitor formed by the sidewalls of the nanogap. For smaller gaps, Coulomb attraction brings opposite charges closer to the sidewalls and generates a field enhancement that is inversely proportional to the gap size[21,99]. 2D finite-element modeling (2D FEM) using COMSOL are carried out to estimate the electric field enhancement as a function of the gap size, w. As shown in Figure 4.10a, the simulated field enhancement factors are in

good qualitative agreement with the measured factors, showing capacitor-like 1/w dependence. Figure 4.10b shows a cross-section of the electric field distribution around a 2-nm-wide slit. The enhanced electric field within the gap is nearly constant along its entire thickness. In modeling, strongly confined electric fields with enhancement factors over 1,000 near the entrance and exit corners are observed.

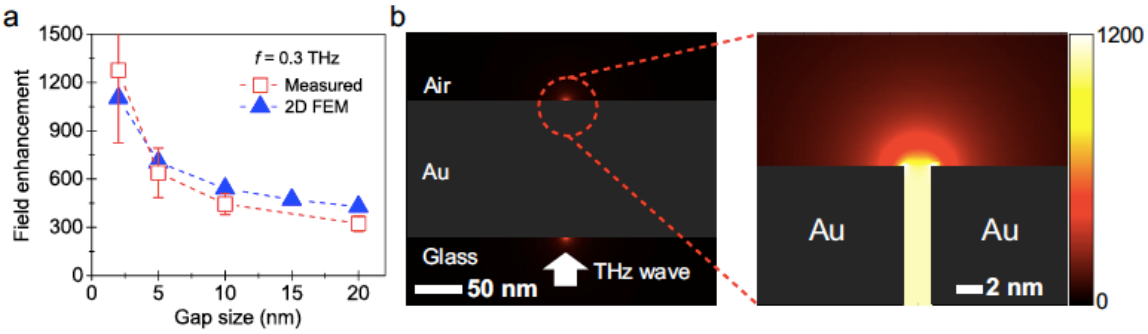

Figure 4.10 Two-dimensional finite-element modeling of THz waves transmitted through a single nanogap. a, Red squares indicate the measured field enhancement of the nanogaps at 0.3 THz as a function of the gap size, performed by THz time-domain spectroscopy. Blue triangles indicate the simulated field enhancements by 2D finite element modeling. **b**, (left) Calculated electric field amplitude around a 2-nm-wide slit in a 150-nm-thick gold film. (right) Enlarged electric field amplitude distribution around the exit of the nanogap. The gap is filled with alumina. Reprinted with permission from Xiaoshu Chen, Hyeong-Ryeol Park, et.al.[47] Copyright 2014, Nature Publication Group.

4.3.3 THz waves transmission through nanogap loop array

Though the film thickness determines the FP resonances at visible frequencies, the horizontal dimension of the loop determines the in-plane resonances at THz frequencies (Figure 4.11a). This leads to the possibility of resonant transmission of THz waves through nanogap ring structures. The work is a collaboration work between our group and that of Prof. D.S. Kim at Seoul National University in Korea.

To experimentally probe the THz response of the annular nanogap waveguides, TDS measurements are carried out over a wavelength range of 0.2–6.0 mm (1.5–0.05 THz) on 150-nm-thick Ag samples with gap sizes w = 1, 2, 5 and 10 nm. Figure 4.11b shows that the period of the second oscillations on the transmitted THz time traces increase from 7.7 to 13 picoseconds as the gap size decreases from 10 to 1 nm. These distortions of transmitted THz pulses correspond to resonance peaks in the spectral domain in Figure 4.11c. By taking the Fourier transform of these time-domain traces, the transmittance amplitude of the input pulse through an array of 1-nm gaps, which occupies only 0.002% of the chip area, is as high as 50% at the resonance wavelength of 4 mm (Figure 4.11c). In contrast, the direct THz transmission through an unpatterned metal film is only 0.1%, indicating very strong field enhancement inside the gap.

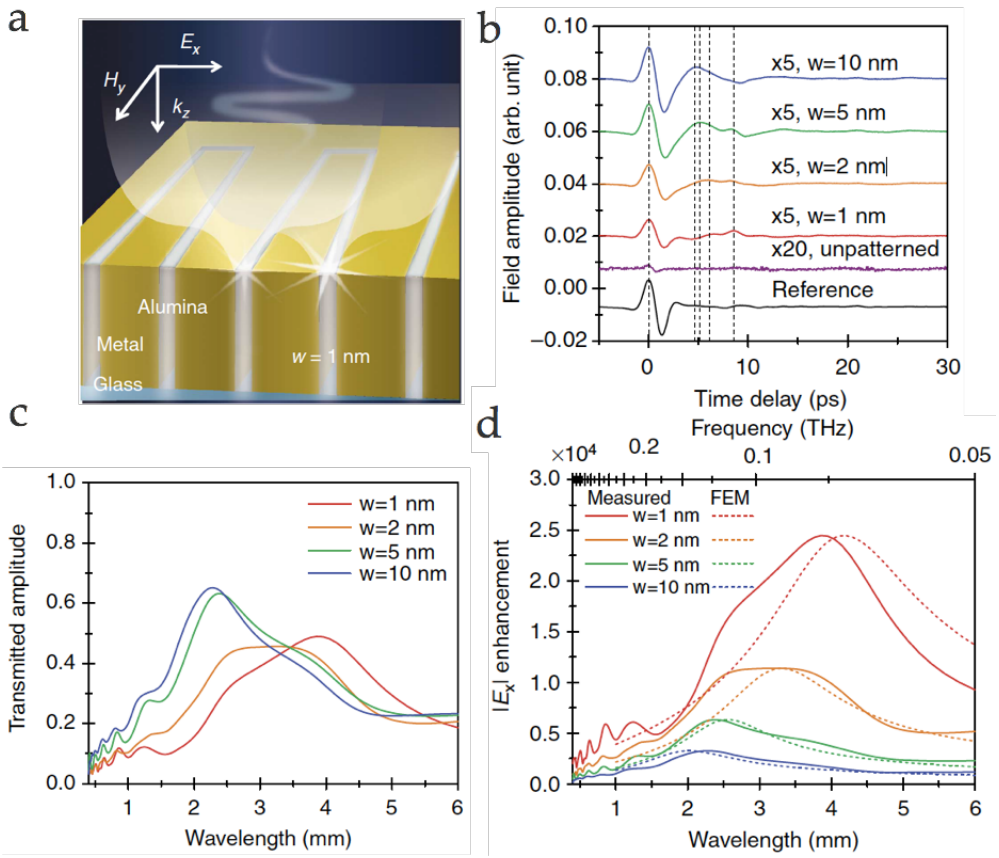

Figure 4.11 Giant THz field enhancements in resonant nanogap ring structures. a, Illustration of THz waves being funneled through nanogaps arranged in rectangular rings. **b**, Time traces for transmitted THz waves through the bare substrate (reference), unpatterned Ag film and nanogap samples with the gap sizes of 1, 2, 5 and 10 nm. The time traces are offset along the vertical axis for clarity. **c**, Fourier-transformed electric-field amplitude, normalized by the reference signal, as a function of wavelength. **d**, Electric-field enhancement, normalized by the coverage ratio of nanogaps with the gap sizes of w = 1, 2, 5, and 10 nm. Solid lines indicate measured fields, determined by THz-TDS. The ringing at wavelengths below 2 mm is the FP resonances in the glass substrate. Dashed lines indicate the calculated transmission spectra, determined by 2D finite

element modeling. To allow resonance wavelengths to be compared, peak values of these calculated spectra are set as the peak values of the experimental spectra.

The diffraction theory, which assumes that the field is concentrated exclusively within the gap, is used to quantify the enhancement factor. This approximation is justified because the dielectric constant of the metal is ~10^6 times larger than that of the dielectric gap at THz frequencies, so that the field intensity in the metal is very small. From this approximation, the field enhancement factors are inferred as high as 25,000 (Figure 4.11d, solid line). It can be seen that the field enhancement is even higher than the factor of 10,000 predicted by 2D FDTD modeling, mostly due to the in-plane THz resonances along the 0.7-mm-long contour of each rectangular loop. To verify that the observed transmission resonances are indeed due to the in-plane resonance, the Wave Eigenmode Analysis tool in COMSOL is used to determine the eigenmodes of the ring structures. Agreement between the measured and calculated resonance frequencies is achieved when a thickness-dependent dielectric constant for the alumina film is used.[100,101] This thickness-dependent response has been inferred from electrical transport measurements, but has not previously been considered when treating the optical response of nanometer-scale junctions. Details on the determination of enhancement factors, in-plane resonances

and thickness determined dielectric constant are given in the Methods section in the reference[46].

In this section, it is demonstrated that a simple patterning method—atomic layer lithography—based on standard photolithography, ALD and adhesive tape, enables wafer-scale production of 1-nm nanogap arrays containing approximately 150,000 devices. The method has the unique ability to produce nanometer-scale gaps over millimetre-scale contours, enabling non-resonant and resonant enhanced transmission of THz waves through nano-sized gaps in opaque metal films. As the measured transmission passes exclusively through the 1-nm gaps, which occupy 0.002% of the chip area, the light transmitted through the nanogaps and the illumination background can be easily separated even for millimetre-sized beam spots. It has been demonstrated that funneling of THz radiation through 1-nm gaps leads to unprecedented field enhancement factors of 25,000, corresponding to intensity enhancement factors of 6.25×10^{8}.

4.4 Conclusions

This chapter introduces the characterization of nanogaps using optical measurements in the visible, near infrared, mid infrared, and THz regimes. The near infrared waves pass through a single nanogap with dimensions as much as 1295 times smaller than the free-

space wavelength, and an effective refractive index as high as 17.8 at visible frequencies is observed in the visible regime. Pushing the gap dimension towards angstrom scale enables wafer-scale investigation of quantum-mechanical nonlocal effects at optical frequencies [11,102-104], optical rectification, [24] and inelastic electron tunneling excitation of plasmons [7,105]. Furthermore, by inserting molecules, nanoparticles or optically active materials in vertically oriented nanogaps, one could dramatically the enhance light–matter interactions over a wide spectral range, enabling a new generation of THz detectors [106] and leading to novel nonlinear phenomena.[107] The centimeter-long nanogap made from the atomic layer lithography makes it possible to gather statistical data from analyte, such as molecules and quantum dots. The smooth top surface the nanogap substrate facilitates the integration with a large array of microfluidic channels. The resonance of the nanogap loops could be easily tuned across broad bandwidth by changing the geometries. Furthermore, by scaling up the nanogap loop length and packing density, it is even possible to study resonant transmission of microwaves through nanogaps[108].

CHAPTER 5

5. Nanogap-Enhanced Light-Matter Interactions

The applications of nanogaps as platforms for enhanced light-matter interactions are discussed. Such applications include nanogap-enhanced infrared absorption, nanogap-enhanced Raman scattering, thin film sensing, and nanogap-enhanced nonlinear optical effect, etc.

5.1 Nanogap-enhanced infrared absorption

The field confinement inside the nanogaps between two metal films enables many applications as stated in the previous chapters. One of major applications of the strong field is spectroscopy. As discussed in section 2.2.1, it is known that infrared absorption spectroscopy is an important analytical technique that complements the Raman spectroscopy to sense and acquire vibrational fingerprint information of molecules in a label-free manner.

Previously, a wafer scale fabrication method that combines atomic layer deposition and template stripping is introduced to make the “U” shape buried nanogap structures. The buried nanogap structures are demonstrated to have strong resonance in the mid infrared confirmed by FTIR measurements. In this section, the application of buried

nanogap cavities as a SEIRE platform will be discussed. The topic covers the modeling of the nanogap cavity, inserting molecules, calculating of enhancement factor, and broadband mid infrared resonator sensor, etc.

The following work is largely derived from the publication:

1. **Xiaoshu Chen**, Christian Ciraciì, David R. Smith, Sang-Hyun Oh, "Nanogap-enhanced Infrared Spectroscopy with Wafer-scale Arrays of Buried Plasmonic Cavities", Nano Letter, 2015, 15, 107-113.

My contributions: I conceptualized the idea and designed the process. I performed all the fabrications, SEM imaging, optical measurements, and molecule sensing. I interpreted the results and wrote the paper.

5.1.1 Modeling of buried nanogap cavity

Modeling of the nanogap cavity is carried out by Christian Ciracì using COMSOL, which is finite-element based commercially available software. It is found that with metal stripe widths gradually changing from 500 nm to 1000 nm with 50 nm increment, the first FP resonance mode from each device ranges from 11 μm to 6 μm. The range covers the typical mid-IR fingerprinting region for molecules, as shown in Figure 5.1a. It also predicts that the strongest electric field of the first FP mode exists at the end facets of

each nanogap cavity, with a simulated field intensity ($|E|^2$) enhancement of about 1600 (Figure 5.1b).

The modeling results suggest the applications of the buried nanogap array: tunable broadband nanogap cavities in mid infrared and molecules sensing using buried nanogap cavities, both of which will be discussed in this section.

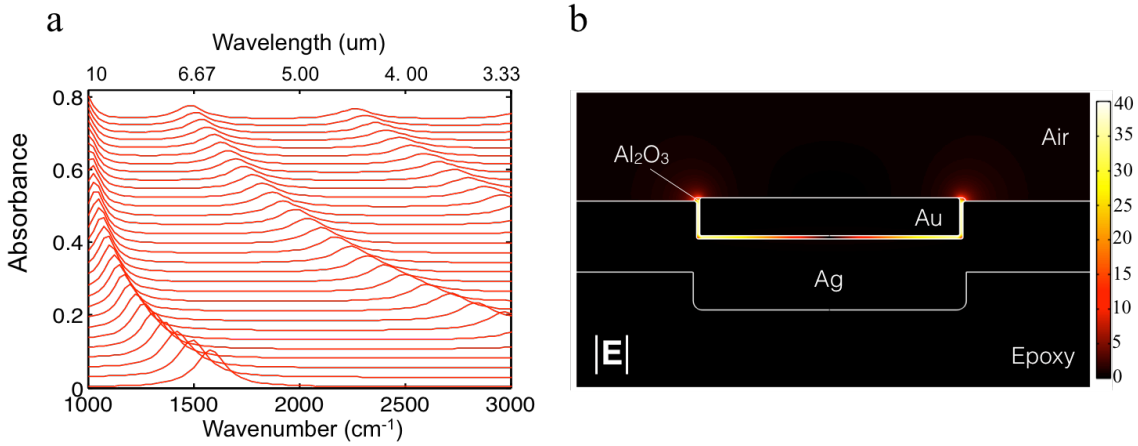

Figure 5.1 COMSOL modeling of gap plasmon in buried nanogap cavities. a, Modeling results of 5 nm gap with various metal stripe width with 50 nm interval. **b**, Electrical field distribution in the buried nanogap, showing the strongest electric field at the outlets of nanogap.

5.1.2 Buried nanogap-enhanced infrared absorption

The resonance of the first FP mode from each nanocavity is tuned in the mid IR by simply changing the width of the metal stripes. Usually, the measured spectral line widths from nano cavities with uniform nanogap cavity width are less than 1 μm, as shown

Figure 4.5 in the section 4.2.2. According to the modeling results in Figure 5.1a, if combine nanogaps with different cavity lengths, it is possible to create a plasmonic resonator that covers a broad spectral region of the mid IR fingerprint region. Similar ideas have been proved by other researches to obtain broadband resonance from engineered optical antennas[109,110].

We made a device with an array of metal stripes, with widths changing from 500 nm to 1010 nm at a 30 nm interval, as shown in Figure 5.2a. The spectrum from this laterally graded cavity resonator is shown in Figure 5.2b. Resonances from nanogap cavity with uniform metal stripe widths of 500, 600, 700, 900 and 1300 nm are also plotted in the same figure for ease of comparison. It can be seen that the device with graded nanocavities possesses a resonance 5-6 times wider than that from the single cavity length resonators.

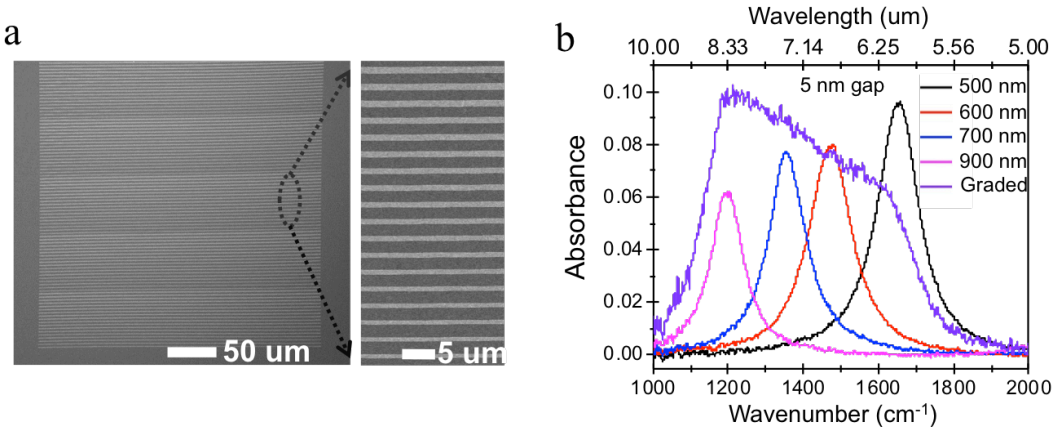

Figure 5.2 Buried nanogap cavities with broadband resonances in mid infrared. a, SEM of the nanogap cavity with graded metal stripe width. The zoomed-in SEM image

shows one section of the device wherein the metal stripe width increasing from 500 nm (bottom) to 1010 nm (top) at a 30 nm interval. **b**, FTIR spectra (purple line) measured from a graded nanogap cavity as shown in **a** (multiplied by 4 for ease of comparison). Spectra from 5 nm gaps with single width (500, 600, 700, and 900 nm) on one device (black, red, blue, and pink line) are plotted respectively in the same figure for comparison. The spectra is measured from an area about 130 μm by 130 μm, and covers about two repeats of the graded nanogap grating structure in **a**.

To utilize the maximum near-field strength inside the gap for sensing application, the molecules should be placed inside the gap region, which is initially filled with the alumina film. To accomplish this, Buffered Oxide Etchant (BOE, HF: H_2O = 1:10) is used to partially remove the alumina inside the nanogap (see Appendix A.9 for more details). After cleaning with DI water and drying with nitrogen, the sample is soaked in a 2 mM benzenethiol (BZT) solution in ethanol for 24 hours to coat the exposed gold and silver surfaces with a monolayer of BZT molecules.[111] Excess BZT molecules are then removed by cleaning the sample with flowing ethanol for two minutes.

The spectra from BZT-coated samples are then measured with FTIR as shown in Figure 5.3a. By increasing the metal stripe width from 450 nm to 900 nm, the resonance position moves from around 6 μm to 11.5 μm. Six fingerprint absorption bands in the mid-IR for BZT covered by the resonances of our nanogap structures are observed:

1000, 1022, 1073, 1181, 1473, and 1575 cm^{-1}. The first FP resonances from these devices overlap with some of the BZT absorption bands. Also shown is the spectrum measured from BZT coated bare silver surface. It can be seen that the absorption is greatly enhanced for molecules in nanogap cavities. Graded broadband nanogap cavity structures are also tested for BZT sensing. As shown in Figure 5.3b, the broadband resonance from a 3 nm gap graded nanogap cavity almost covers the full range of BZT absorption bands and also shows enhanced absorbance. Comparing to the nanogap cavities with narrower resonance, the broadband nanogap cavities cover broader spectral range and could provide more information in molecule sensing.

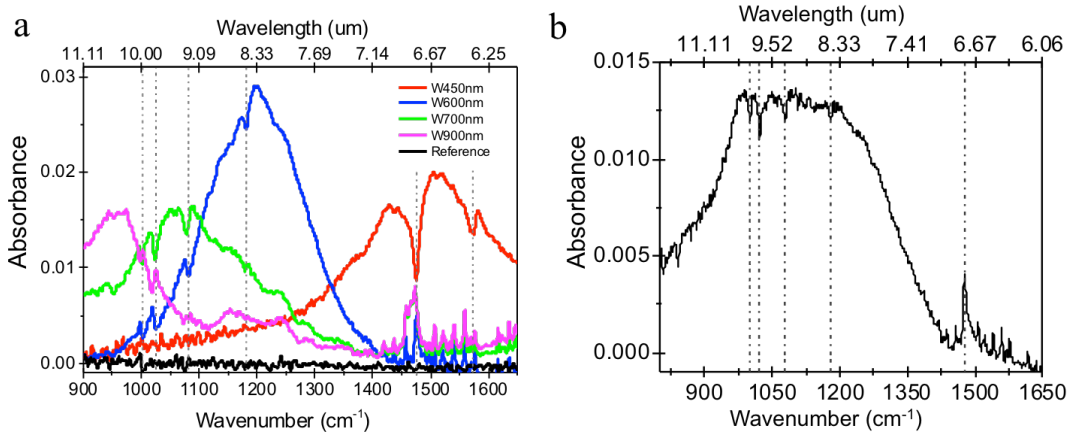

Figure 5.3 Nanogap-enhanced infrared absorption. a, Sensing of benzenethiol using 3 nm wide buried nanogap with various metal stripe widths. The black curve is the absorption of BZT molecules coated on a template-stripped silver film without any pattern. With nearly normal incidence of light, the absorption from BZT is below noise level due to the surface selection rule[112]. **b**, Sensing of BZT using the graded nanogap

structure with 3 nm gap size. The vertical gray dashed lines in **a** and **b** indicate the multiple absorption bands of BZT.

The experimental spectra show asymmetric Fano-shape resonance for each absorption band overlaps with a gap plasmon resonance, which has also been observed by other researchers[82,113-115]. The behavior is demonstrated by modeling too. The BZT monolayer is modeled as a thin dielectric layer, whose dielectric function is obtained as a sum of Lorentz oscillators that match the absorption resonances of BZT molecules. For clarity, however, the oscillator corresponding to the main resonance at 1473 cm^{-1} is modeled. As for the actual experimental sample, BZT molecules are intercalated roughly 3 nm into the gap (the depth is controlled by the BOE etching time) to increase the coupling between the molecules absorption bands and the gap-plasmon resonances.

A set of modeling reflection spectra is calculated for different stripe widths as shown in Figure 5.4. As the resonance of the nanogap cavities is shifted across the BZT absorption resonance, a very distinct Fano-shape feature appears in the reflection spectra. The resonances are qualitatively identical to those shown in Figure 5.3a, and the shape of the Fano resonances depends on the relative position of the BZT absorption band with respect to the energy of the gap plasmon resonance.

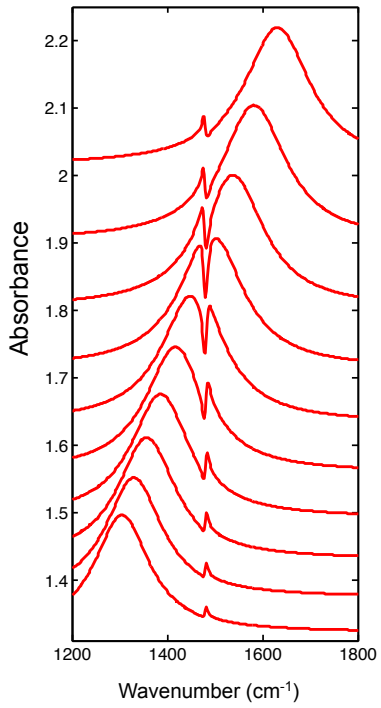

Figure 5.4 Modeled Fano coupling between a BZT absorption band and the first order FP mode of gap plasmon resonance. The BZT absorption at 1473 cm^{-1} is coupled with gap plasmon resonance. The shape of the absorption changes as the plasmon resonance shifts.

5.1.3 Infrared absorption enhancement factor

The IR absorption measurements from nanogap samples are compared with the spectra obtained from reference samples (template-stripped flat silver surface) to calculate the IR absorption enhancement factor. We assume BZT molecules form a uniform monolayer on gold and silver surface both inside of the nanogaps and on the top metal surface, with a same packing density. To take the reference signal from a bare silver surface, the main bench of a Nicolet Series II Magna-IR System 750 FTIR is used. An incidence angle of

83° is chosen for the IR beam to satisfy the surface selection rule. The beam spot is an ellipse around 2 mm and 3 mm in conjugate and transverse diameter.

The enhancement factor is defined as the absorption of BZT coated on nanogap devices comparing to the absorption of BZT coated on a bare silver surface:

$$\mathrm{EF} = \frac{\mathrm{A_{gap}}}{\mathrm{N_{gap}}} \Big/ \frac{\mathrm{A_{surf}}}{\mathrm{N_{surf}}} \tag{5.1}$$

where N_{surf} is the number of BZT molecules contributing to the absorption on a bare template-stripped silver film; N_{gap} is the number of BZT molecules contributing to the SEIRA signal, and A_{gap} and A_{surf} are the amplitudes of the absorption band of interests in the gap and on the template-stripped silver (area coverage ratio is one). Also, an angle correction sin (83°) is applied to A_{surf}. So the equation becomes:

$$\mathrm{EF} = \frac{\mathrm{A_{gap}}}{\mathrm{D} \times \frac{\mathrm{L}}{\mathrm{P}} \times 4\mathrm{wL}} \Big/ \frac{\mathrm{A_{surf}}}{\sin(83^\circ) \times \mathrm{D} \times \mathrm{S_o}} \tag{5.2}$$

where the *D* is the surface density of BZT monolayer on a metal surface, which is assumed to be the same for nanogap and template-stripped metal surface; *L* (=130 μm) is the width of the square aperture in the IR microscope; P (=3 μm) is the period of embedded nanogaps; and w is width of the nanogap. The depth of nanogap after BOE etching is assumed equal to the width of nanogap. So the surface area inside the nanogap for each embedded nanogap device is 4wL. S_o is the area of the beam spot size of the IR beam in the main bench. The EFs calculated from nanogap cavities with 3 nm gap width

are shown in Table 5.1. It can be seen that the enhancement factors as high as 10^4-10^5 are calculated using the above definitions.

Absorption peak (1/cm) \ Absorption on substrates and EF		Template stripped silver	Nanogap cavity width w=450 nm	EF	Nanogap cavity width w=600 nm	EF
1575		3.00E-05	0.00238	**5.49E+05**		
1473		3.30E-04	0.00752	**1.58E+05**		
1181		1.20E-04			0.0109	**6.28E+05**
1073		1.20E-04			0.00168	**9.69E+04**
1022		1.00E-05			0.00234	**1.62E+06**
1000		1.00E-05			0.00172	**1.19E+06**
Absorption peak (1/cm)	Nanogap cavity width w=700 nm	**EF**	Nanogap cavity width w=900 nm	**EF**	Nanogap cavity with graded width	**EF**
					0.00077	**4.46E+04**
1073	0.00273	**1.67E+05**			0.00129	**7.44E+04**
1022	0.00278	**1.94E+06**	0.00242	**1.66E+06**	0.00226	**1.56E+06**
1000	0.00185	**1.31E+06**	0.00121	**8.30E+05**	0.00147	**1.02E+06**

Table 5.1 SEIRA enhancement factor for different nanogap cavity devices. The blanks in the table are the BZT absorption bands that are not overlapped with gap plasmon resonances and thus are not observable in the spectra.

5.1.4 Discussions

In summary, buried plasmonic nanocavity arrays with a minimum gap size of 3 nm are fabricated using atomic layer deposition and template stripping in wafer scale. These structures generate intense gap plasmons that boost near-field coupling of mid infrared radiation with molecules situated in the gaps, and enhance the IR absorption by approximately 5 orders of magnitude. As the hotspots of each nanocavity uniformly extend along millimeter-long lines, our substrates are robust against localized defects or

contaminants, which helps to achieve more reproducible SEIRA spectroscopy. The ultra-long plasmonic hotspots also facilitate practical sensing applications over large areas, in contrast to the point-like nanogap structures used in previous experiments. As with other template-stripped metallic nanostructures,[76] the surfaces of these nanogap cavities are initially protected by a silicon template. The template provides a robust protection mechanism against contamination or degradation, and thus each chip can be stored for a long time and template-stripped on-demand, which is essential for the storage and dissemination of the devises. The vertical arms of the "U" shape cavity allow the coupling of incident light. The dielectric material in the vertical arms can be easily removed and backfilled with analyte molecules. These buried cavities are mechanically robust in further processing and the template-stripped planarized top surface facilitates integration with other devices. Note that smaller gap dimensions (down to 1 nm) should be achievable using ALD even though they are not needed for the molecular sensing experiments performed here. Our technique dramatically reduces the cost of fabrication for SEIRA substrates and provides new possibilities to carry out bio-molecular fingerprint sensing at mid IR frequencies.

5.2 Nanogap-enhanced Raman scattering

Ultra-thin metal-insulator-metal nanogaps[22-24,46,47] and ultra-sharp nano tips[25,116,117] are demonstrated to be very effective plasmonic building blocks. Both structures can be used to tightly confine electromagnetic waves into nano scale volume to get strong local electric field for studies and applications such as nonlocal effect[11], enhanced light-matter interactions[118-120], high resolution imaging[76], optical trapping[121], and sensing[122], etc. Here, the application of the complex structure, ultra-thin nanogaps fabricated on ultra-sharp tip of metal wedges introduced in section 3.3.2, will be discussed.

My contributions: I did confocal Raman measurements on molecules coated complex nanogap structures with two lasers at different wavelengths, analyzed the data, and calculated field enhancement factor, etc.

5.2.1 Confocal Raman scattering measurements

The buried nanogaps on wedge tip are used as a surface enhanced Raman scattering platform. The alumina layer sandwiched between the two layers of metal has many outlets in the metal films, which serves as nano sized gap if the alumina is partially etched using wet etching (BOE). After partially removing alumina between metal (silver) layers, the complex nanogap samples are incubated in a 2 mM benzenethiol (BZT)

solution in ethanol for 24 hours to form a self-assembly monolayer of BZT molecules on the metal surface. The samples are then rinsed with ethanol spraying for 2 minutes to remove any excess BZT molecules. BZT is chosen because it is known as an efficient Raman scatter and its Raman spectra have been well characterized[123].

With a confocal Raman microscope, enhanced Raman scattering is observed from different XY planes at the different Z positions of the 3D structures. An Argon ion laser at 514.5 nm is focused to diffraction-limit by an object lens and scanned at a plane across the wedge by sitting the sample on a XYZ scanning stage (schematic shown in Figure 5.5h), where the scattered Raman signals are collected with the same objective lens and a fiber. The Raman signal is then being measured by a spectrometer.

The Raman scattering intensity is strongly polarization-dependent[124], as shown in Figure 5.5a-g. In figures 5.5a-d, the Raman images are collected at different Z positions (500 nm per step, from the bottom of the wedge to the tip of the wedge) in horizontal planes across the wedge and with the laser polarized perpendicular (P2; P1 is defined as the polarization of laser along the nanogaps) to the nanogaps on the tip of the wedge. The gap plasmons can only be excited with TM polarized light. So in each scan plane, the hot spots are observed at different positions on the wedge when the light is polarized across the nanogap on the 3D wedges.

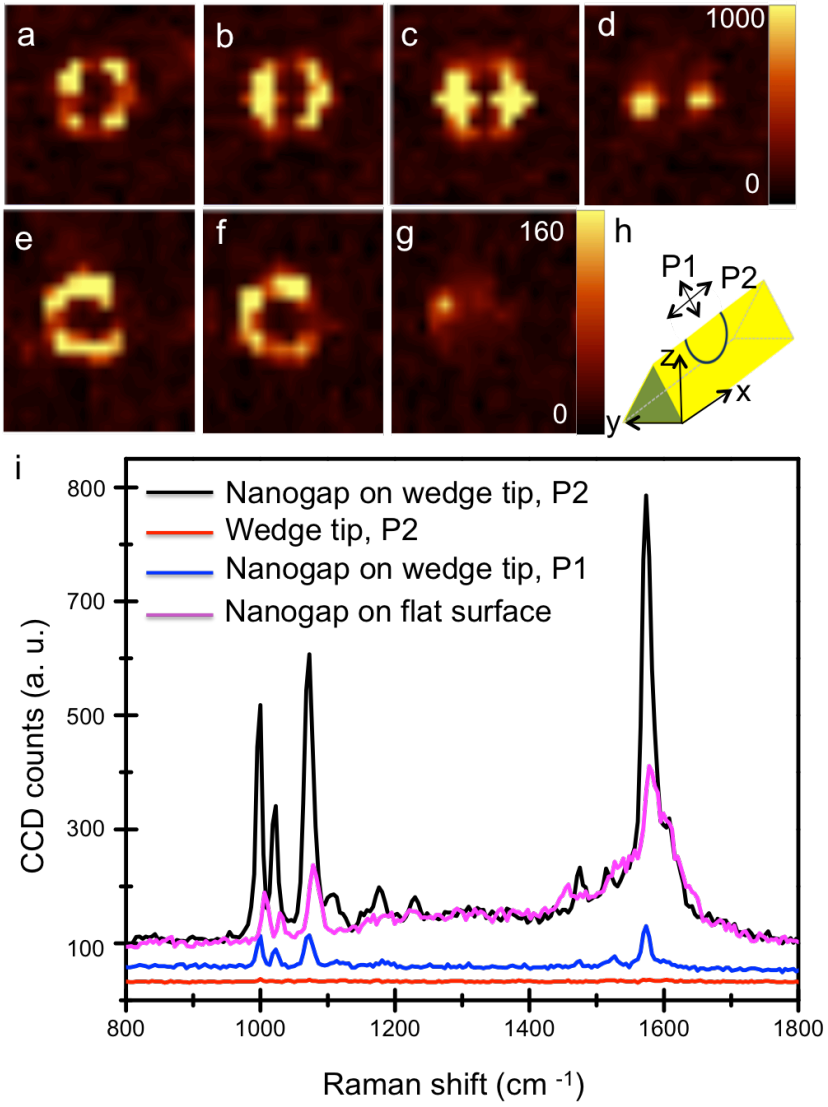

Figure 5.5 Raman scattering from BZT on nanogap at wedge tip excited with 514.5 nm laser. Raman intensity images on XY plane at multiple Z positions from nanogaps (5 nm gap width) on wedge structure with laser polarized perpendicular to the nanogap **a-d** and parallel to the nanogap **e-g**. The Laser wavelength is 514.5 nm. **h**, Schematic of laser polarization and the layout of nanogap on wedge tip. **i**, Raman spectra at wedge tip from 5 nm nanogap on wedge structure with laser polarized across nanogap (P2). The intensity images from **a-g** are generated by integration of the breathing mode of the BZT aromatic ring with 30 cm^{-1} spectral width.

As shown in the Raman intensity images in Figure 5.5e-g, the Raman scattering intensity at the nanogap on wedge tip with P2 polarized light is about 10 times stronger than illuminating with P1 polarization. The reasons for still observing SERS with laser polarization along to the gap are (1) the roughness of nanogap sidewall and (2) the lightning-rod effects from the sharp wedge tip. The Raman scattering spectra are shown in Figure 5.5i, where the spectra from nanogaps on the wedge tip and from bare wedge tip are compared with different polarized light. An enhancement factor of 10^4 is obtained by placing 5 nm nanogaps on wedge tip, in comparison to the Raman scattering of BZT coated on flat silver surface. The enhancement factor is also five times higher than the enhancement from a nanogap on flat metal surface.

Though the structure is not designed to have a resonance at 514. 5 nm, enhanced Raman scattering is observed from nanogaps on wedge tips. To see if the enhancement is wavelength-dependent, the nanogap on wedge structures are also tested with a 753 nm laser. The Raman intensity images and spectra are showed in Figure 5.6. Similarly, strong Raman scattering are observed from the non-resonance nanogap structures. It can be noticed that with a 753 nm laser, a red shift of Raman scattering is observed in comparison to the bulk Raman vibrations of neat benzenethiol, which is because the

adsorbed molecule changes its chemical structures by forming chemical bonds to metal surfaces[125].

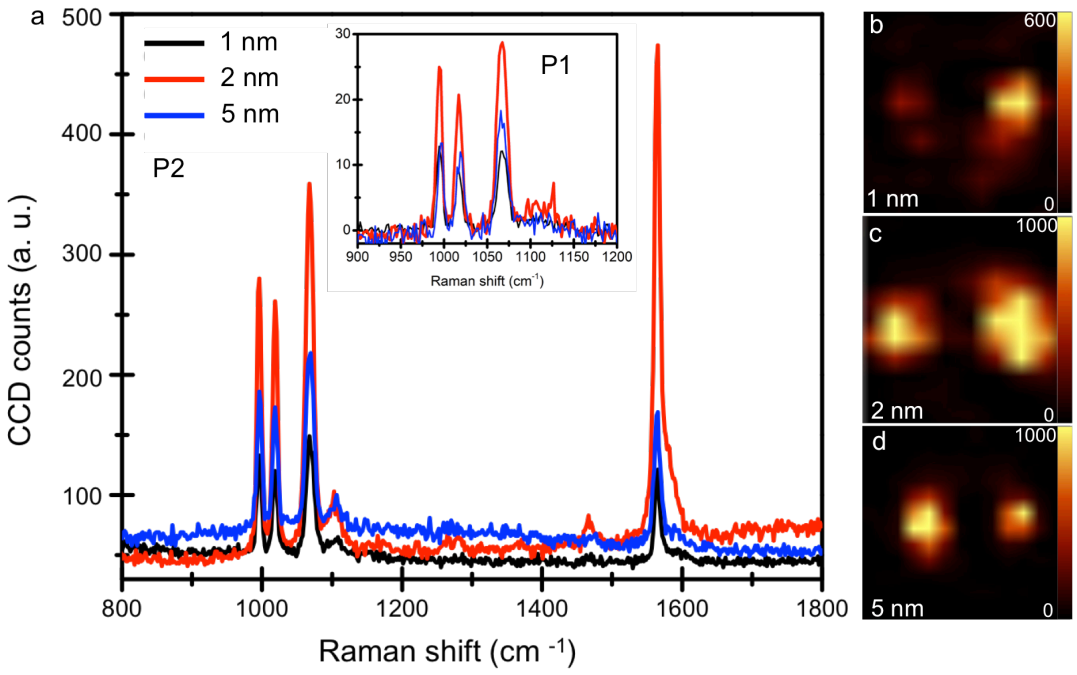

Figure 5.6 Raman scattering of BZT from nanogaps on wedge tips excited with a 753 nm laser. a, Raman spectra collected from 1, 2, and 5 nm nanogaps on wedge tips with laser polarized across nanogap (P2). The insert in **a** shows the Raman spectra from the same spot with laser polarized along the nanogap (P1). Raman intensity images on XY plane at different Z position in the nanogap on wedge structures with 753 nm laser polarized perpendicular to the nanogap are shown in **b-d** for gap size of 1,2 and 5 nm.

It is interesting to notice that the Raman scattering increases as the gap size changes from 5 nm to 2 nm, and decreases as the gap size changes from 2 nm to 1 nm. One possible reason could be the size of BZT molecule (0.6 nm)[126] is comparable to the nanogap width in 1 nm gaps. It is possible that only a single layer of BZT can be formed

inside the 1 nm wide gap. Furthermore, another reason could be the steric hindrance effect of molecules in an ultra-narrow gap[127]. When the concentration of BZT inside the 1 nm gap is lower, the angle of the molecules to the normal direction of metal surface is larger than the angle formed in the higher concentration case. Due to surface selection rule, the interaction of TM polarized field with the molecules will be smaller. Also, the Raman scattering intensity in 1 nm gap is about half of that in 2 nm gap, which suggests that the field in the non-resonant 1 nm gap is comparable to that in the 2 nm gap. It is known that when the gap sizes decreases from 2 nm to 1 nm, non-classical effects, such as tunneling and nonlocal effect, start to play roles. Theoretical and experimental studies indicate that the field predicted from the non-classical model is usually smaller than the value predicated by the classical model when the nanogap size decreases from classical to the non-classical regime[104,128].

5.2.2 Raman enhancement factor

The field enhancement factor of Raman scattering intensity from a 2 nm gap on the wedge tip is calculated using this equation：

$$\mathrm{EF}_{\mathrm{GapSERS}} \propto \frac{\mathrm{I}_{\mathrm{GapSERS}}\,\mathrm{N}_{\mathrm{Vol}}}{\mathrm{I}_{\mathrm{Vol}}\,\mathrm{N}_{\mathrm{Surf}}} \tag{5.2}$$

where $EF_{GapSERS}$ is the enhancement factor of Raman intensity in the nanogap on wedge tip. Raman scattering from neat BZT (Thiophenol, ≥99%, Sigma-Aldrich) in a quartz cuvette with 1 mm light path is measured as a reference. $I_{GapSERS}$ and I_{Vol} are Raman scattering intensities of the in-plane ring breathing mode coupled the to the $\nu\,(C-S)$ (shift from 1092 cm^{-1} to 1065 cm^{-1}) from BZT coated on the silver surface of nanogap sample[45,129,130] and from the neat liquid BZT sample respectively, by subtracting the Raman scattering intensity at 900 cm^{-1} (as background). N_{Surf} is the number of BZT molecules in the laser spot area on metal surface plus the area inside the nanogaps for calculating the averaged enhancement factor, or it is the number of molecules in the area inside the nanogaps for calculating local enhancement factor. N_{Vol} is the number of BZT molecules in the laser focus volume in the neat liquid BZT. For 2 nm gap on wedge tip, the average enhancement factor is about 10^4, and the local enhancement factor is as large as $10^7 \sim 10^8$. Refer to Appendix A. 10 for more details about the definition of the average and the local enhancement factors.

5.3 More discussions of nanogap-enhanced light-matter interactions

5.3.1 Nanogap-enhanced THz and thin film interactions

Thin film sensing in THz range has been limited by the small interaction cross-section due to the huge mismatch of THz wavelength and the thin film thickness. SPR sensing in the visible regime can easily detect resonance shifts upon 1 nm thick or sub- 1 nm change in film thickness[131]. However, with THz-TDS, the minimum detectable film thickness is a few microns for common dielectric materials, such as photoresist and polydimethylsiloxane (PDMS)[132-134], and a few hundred nanometers for materials that absorb THz radiation such as water and DNA[135]. Various schemes including waveguide, slot antenna, and metamaterials have been employed to enhance the interaction of THz waves with thin films. However, the detection of nanometer-thick films has never been demonstrated before.

Another interesting thin film, graphene, has attracted a lot of interests in the past two decades[136]. It is a one-atom-thick fabric of carbon with very high electronic and thermal conductivities, mechanical strength and unique optical properties. The applications of graphene include flexible electronics[137], high frequency transistors[138], photon detectors[139], optical modulator[120,140], sensor[141], and energy storage[142,143], etc. Besides graphene, there

are many other interesting 2D materials, such as boron nitride (BN)[144] and molybdenum disulphide (MoS_2)[145]. In the aspect of interaction with light, there is a huge mismatch of the atomic scale thickness of the 2D materials and the much larger wavelength of light. Especially for THz waves, normally with millimeter wavelength, the interaction of THz and graphene is extremely weak[146].

Atomic layer lithography fabricated nanogap arrays and centimeter long nanogaps are particularly useful for thin film sensing in THz waves. Sensing of 1 nm thick thin film and the enhanced interaction between graphene and THz waves are demonstrated using nanogaps. More information about these applications can be found in these references[47,120,122].

5.3.2 Nanogap-enhanced nonlinear optical effect

Plamsonic nanostructures have the potential to incredibly enhance the local electric field of light, thus can greatly enhance the usually very weak higher order nonlinear optical effects, such as second harmonic generation[147] and third harmonic generation[148]. Furthermore, as the distance of the two metal films is reduced to less than 5 nm, the classical nonlocality[149] effect starts to play a role. Through collaboration with Prof. David R. Smith's group at Duke University, the applications of the planar nanogaps in study of

nanogap enhanced third harmonic generation and nonlocal effect are demonstrated. More details can be found in references[71,72].

5.4 Conclusions

The applications of nanogaps for enhanced light-matter interactions, including surface enhanced infrared absorption and surface enhanced Raman scattering, are demonstrated in this chapter. It can be seen that our unique fabrication schemes provide effective methods to make nanogap structures for these applications. The atomic layer lithography is very straightforward to disseminate and could be easily adopt by interested researchers. By removing one of the largest obstacles in nanofabrication, our new patterning technique will boost the throughput of experimental studies and help to accomplish practical applications of ultra-strong light-matter interactions in nanogaps. Furthermore, nanogaps can be easily integrated with electrical contacts, and such devices can be used for studying light-induced quantum-mechanical tunneling, nonlocal electrodynamics, and applications such as mid-IR wave detection and emission[61], as well as investigation of 2D materials such as graphene and MoS_2[120].

CHAPTER 6

6. Electrical Applications of Nanogaps

As discussed in previous chapters, vertical nanogap structures are particularly suitable for electrical applications. When the two electrodes are only a few nanometers apart, the electric field inside and near the nanogap area can be greatly enhanced and thus lead to many applications. In this chapter, I will discuss the utilities of vertical nanogap and planar nanogap structures to enhance local electric field for applications such as dielectrophoresis and tunneling-induced light emission. The work is not published yet until the submission of this thesis.

My contributions: I designed the electrodes to electrically address the vertical and planar nanogaps, and also developed lithography fabrication scheme and fabricated the devices. I also carried out light emission measurements.

6.1 Dielectrophoresis

In this section, the background for dielectrophoresis (DEP) is briefly introduced. Then the method and the process to fabricate electrical addressable nanogap structures for DEP applications are discussed in detail.

6.1.1 Background of dielectrophoresis

Dielectrophoresis is the movement of polarizable particles in the presence of a non-uniform electric field. DEP forces originate from the differences between the dielectric properties (conductivity and permittivity) of the particles and the medium environments. The force that a particle experiences in an electrical field is given by

$$\overline{F_{elec}} = q\overline{E} + (\overline{m}\nabla)\overline{E} + \frac{1}{6}\nabla(\overline{Q}:\nabla\overline{E}) + \cdots \quad (6.1)$$

The first term describes the Columbic interaction between the net charge of the particle and the electrical field $\overline{E}$. If the particle is not charged or the net field is zero, the first term is zero. $\overline{m}$ and $\overline{Q}$ are the dipole and the quadruple force components. The two additional terms are the interactions of the particle and the electric field, which are not zero when the field is spatially non-uniform ($\nabla\overline{E} \neq 0$).

From equation 6.1, the time-averaged DEP force on a sphere particle is given by:

$$< \overline{F}(t) >= 2\,\pi\varepsilon_m^* r^3[\mathrm{Re}\big(f_{CM}(\omega)\big)\nabla E^2 + \mathrm{Im}\big(f_{CM}(\omega)(\overline{E}\nabla\overline{\varphi})\big)] \quad (6.2)$$

here, r is the radius of the sphere. $f_{CM}(\omega)$ is the complex Clausius-Mossotti function and is defined as $\frac{\varepsilon_p^*(\omega)-\varepsilon_m^*(\omega)}{\varepsilon_p^*(\omega)+2\varepsilon_m^*(\omega)}$, where $\varepsilon_p^*(\omega)$ and $\varepsilon_m^*(\omega)$ are frequency dependent complex permittivities of the particles and the environment medium, respectively. Since $f_{CM}(\omega)$ is frequency dependent, the net DEP force is also frequency dependent. The sign (negative or positive) of the real part of the $f_{CM}(\omega)$ decides whether the particles being pushed

away (negative DEP) or trapped (positive DEP) toward the electrical field maximum or minimum. The sign of the imaginary part of the $f_{CM}(\omega)$ determines whether the particles being pushed in the same or opposite directions to which the field is traveling. The strength of the force also depends on the particle shape, size, the frequency, and the magnitude of the electric field, indicating the possibility of selective manipulation of different particles. Furthermore, the detection of low concentration analyte depends both on detection devices and transportation of the analyte towards the devices. Usually, diffusion dependent detections take many hours. However, with DEP forces, the diffractive limit can be exceeded and the responsible time of the detection can be speeded up enormously. So the DEP forces are widely used to study, manipulate, transport, and sort various types of particles. More details about DEP can be found in this references[150].

From equation (6.2), it can be seen that larger electric intensity gradient helps to achieve stronger dielectrophoresis forces. One method to get large gradient is to minimize the geometry of the electrode. Structures such as metallic tips[151], micro/nano scale gaps[152], and sharp electrode edges are fabricated to enhance the DEP forces. There have been many methods to fabricated electrode structures, however, the method to make chip scale devices with nano-sized distance between two electrodes are still not available. Here, our centimeter long nanogap substrate, which is described in section 3.1.2, will be

introduced as a practically suitable substrate for making electrodes with nano-sized distance to enhance DEP forces.

6.1.2 Fabrication of chip scale electrically addressable vertical nanogaps

The centimeter long nanogap fabricated by the method described in Chapter 3 is used as a substrate to fabricate the chip scale electrodes. On each chip, there is a centimeter long rectangle nanogap loop patterned with alignment marks, which can be used for further photolithography. In the photolithography process, first, negative resist is coated on the nanogap substrate. To bake the resist, the temperature of the hotplate should not be higher than 100 ºC to avoid deforming of the nanogap. Then electrode patterns are defined by patterning the negative resist, as shown in Figure 6.1a. The exposed metal is then etched away using ion mill etching. At last, the mask resist is removed in a solvent (1165 Remover) to expose the nanogap between the patterned electrodes, as shown in Figure 6.1b. The detailed fabrication process is further discussed in Appendix A.3.

As shown in Figure 6.1c, hundreds of electrode patterns can be fabricated on the centimeter long nanogap substrate. The black dot line in the figure indicates the position of the nanogap. Figure 6.1 d and e show the photographs of the fabricated devices. The zoomed-in figure clearly shows that every two metal electrodes are separated by one

nanogap. Nanogap arrays with 30 nm gap in width are fabricated using the above-mentioned process. The current voltage (IV) curves of the nanogaps are tested to confirm the insulation of nanogap using a HP 4145A semiconductor analyzer and a Signatone probe station. For 30 nm thick alumina film inside the nanogap, the measured current is below the noise level of the measurement setup at a bias voltage as large as 20 V, which is already larger than the usual applicable working voltage for DEP trapping applications.

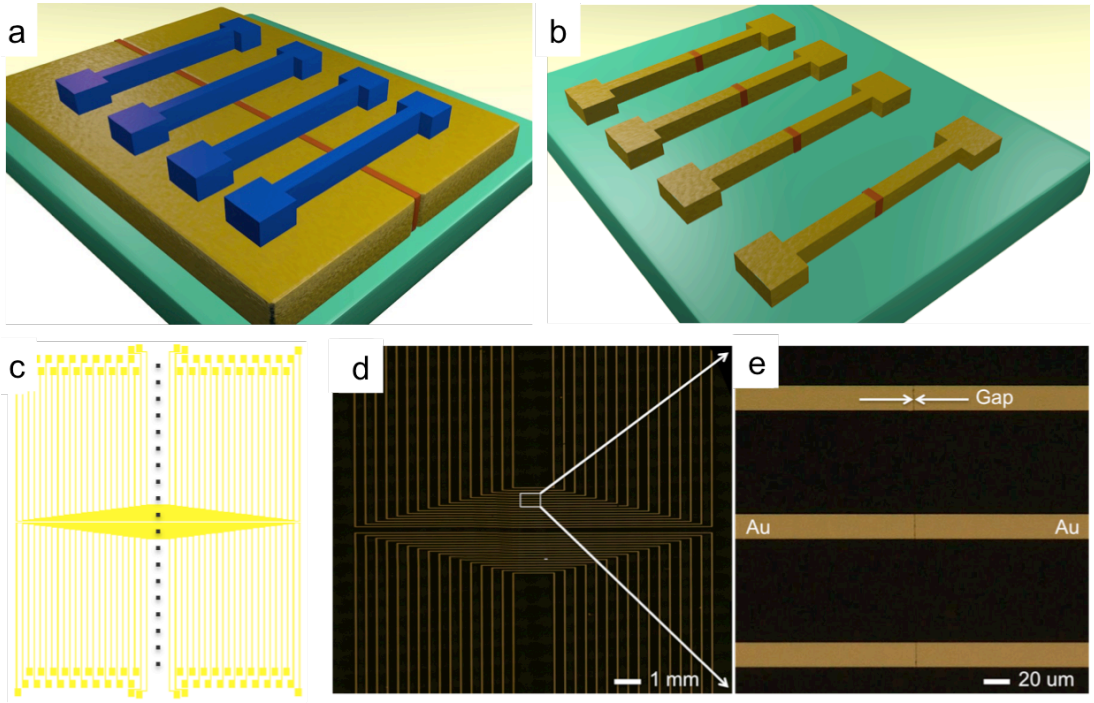

Figure 6.1 Photographs of a chip design and the fabricated chip with electrically addressable nanogaps. **a-c**. Fabrication process and the pattern design for an array of electrically addressable nanogaps. **d**. Optical microscope image of electrically addressable nanogap array on a glass substrate. **e**. Zoomed in optical microscope image showing three nanogaps with patterned electrodes. The width of the nanogaps is 30 nm.

6.2 Tunneling-induced light emission from planar nanogaps

6.2.1 Background of tunneling-induced light emission

People have observed tunneling-induced light emission when electrons tunnel across a very thin dielectric film[7,153], however, at a very low efficiency. The mechanism of the light emission evolves the interplay between the fundamentally quantum-mechanical process of tunneling and the very strong optical and electrostatic fields within a single digit nanometer-sized gap — a regime that nonlinear and non-equilibrium effects dominate[154,155]. The understanding of this extreme regime is limited by the difficulty to make controllable, large-scale, and sub-nanometer gaps between metal surfaces. Tunneling-induced emission has been measured between metal surfaces and scanning-tunneling-microscope tips[105,156]. The geometry provides very small gaps and allows precise control over the gap size, but only emits at a single point with very weak signals, which limits the quantitative understanding of the tunneling-induced light emission process.

Here we try to use the planar nanogap (stack of metal-insulator-metal films) arrays created by the method described in Chapter 3 to study tunneling-induced light emission. The dielectric film that the electrons tunneling through is the ultra thin alumina film in

the nanogap. This section will explore four different designs to make nanogap for tunneling-induced light emission. The planar nanogaps are patterned into an array that expects to help to couple light out from the nanogaps. Systematically investigations are carried out to study the turn-on voltage, efficiency, and lifetime of the devices with different dielectric thickness and different substrates. The arrays of nanogap are designed to study how the efficiency of tunneling-induced emission is affected by the geometry of the array, such as period, line width, etc.

6.2.2 Tunneling-induced light emission chip fabrication and preliminary results

Four different designs of the samples are fabricated and tested for tunneling-induced light emission measurements. Two tungsten probes are used to electrically connect to the patterned electrodes and apply direct voltage across the nanogaps.

Sample A*:* Template strip metal (gold) lines (40 nm in thickness, 2~3 μm in width) in epoxy, as electrode one; coat the sample with 5 nm alumina using ALD at low temperature; then deposit a second layer of gold (43 nm in thickness) using sputtering by partially exposing the electrode fingers. A third gold film with adhesion layer is deposited by sputtering only on top of the second gold film to serve as electrode two. The two

selective sputtering deposition processes are realized by covering part of the pattern with cover glass slides.

By applying a bias voltage across the nanogap, it is found that the turning on point for 5 nm alumina thick nanogap device is 3.7 V. When increasing the voltage to 3.8 V or higher, the light emission becomes stronger. After the voltage being increased to 4.1 V, the device emitted light for about 15 minutes and broke down.

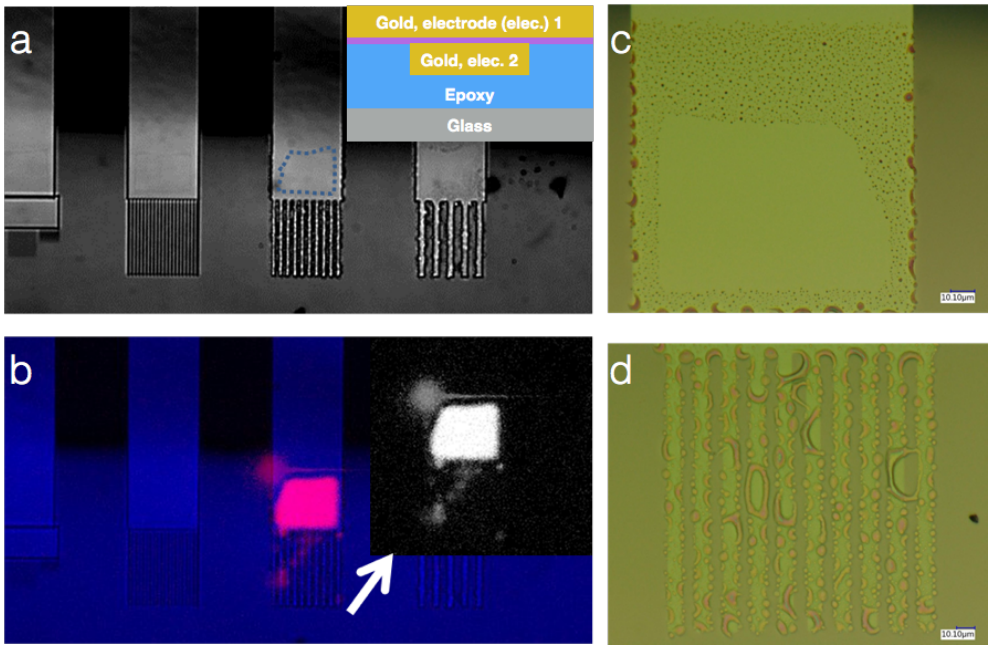

Figure 6.2 Schematic of *sample A* and tunneling-induced light emission measurement. a, micrograph of planar gap formed between template stripped metal film and micro sized pattern array. The insert is schematic of *sample A*, where the purple color is 5 nm thick alumina; and elec.1 is 43 nm thick template stripped gold film; elec.2 is 40 nm deposited gold film. **b**, Light emission observed at 4.0 V showed in false color (The insert shows the CCD image of light emission). **c** and **d**, micrographs of planar gap after

light emission measurement, showing the deformation of the nanogap due to the melting of epoxy.

The template stripping method provides an ultra-smooth metal surface, thus we can get more uniform nanogap between the TS gold and the secondly deposited gold film. However, the epoxy is melted or deformed due to the heat generated by tunneling induced current. As shown in Figure 6.2 b and d, the epoxy is melted in the patterned gold area, without emitting light after the deformation. The areas where epoxy doesn't melt emit most of the light. This is due to the heated generated from the tunneling induced current. The overheat issue could possible be solved by sitting the sample on a more heat conductive substrate. For example, instead of using glass as substrate, more heat conductive substrate should be used.

To avoid the problem of epoxy and also to see if ultra smooth metal surface is necessary for light emission, nanogaps are made on direct deposited metal in *sample B*.

Sample B*:* Instead of using template stripped ultra smooth surface, gold lines (40 nm in thickness) are patterned on silicon wafer as the first electrode. Following with the ALD (3 nm alumina), a 35 nm gold film is deposited as the second electrode. *Sample B* and the light emission results are shown in Figure 6.3. After applying a voltage, the device starts to emit light at about 1.5 V. Most of the light emitted from the nanogap grating area.

Though the device emits more light as the voltages increases, the emitted light is so weak that the CCD needs to work in single photon counting mode to detect the light. And the signal is too weak to allow spectroscopy measurement. For the device with 3 nm alumina layer inside the gap, it starts to break down at about 2.1 V.

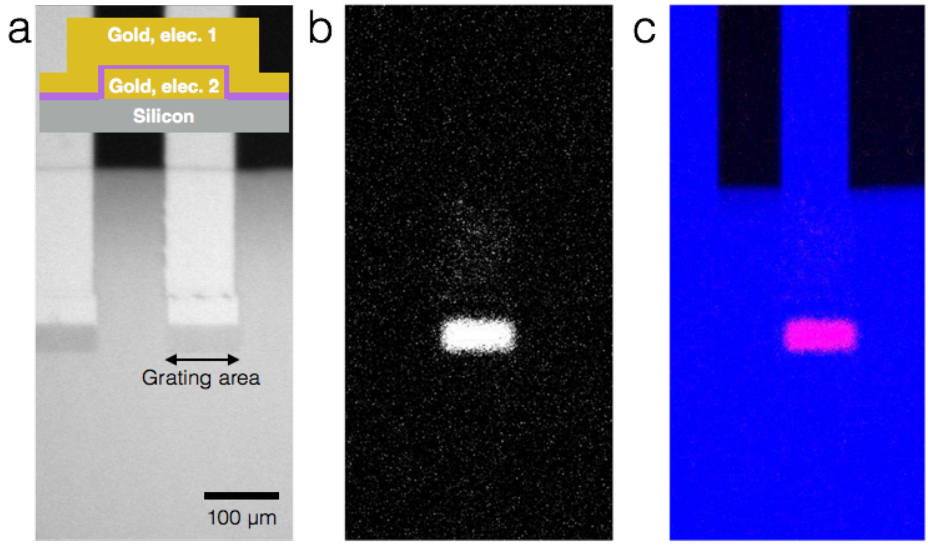

Figure 6.3 Schematic of *Sample* B and tunneling-induced light emission measurement. a, micrograph of planar gap formed between metal film and nano sized pattern array. The insert is schematic of sample B. **b** and **c**, CCD image and false color image of light emission observed at 1.9 V.

To test the lifetime of the device, the biasing voltage is fixed at 1.9 V, and at the meanwhile the emitted light is recorded using a CCD camera. The lifetime of the device is longer comparing that of *sample A* – with epoxy at the substrate. However, within one hour, the device with 3 nm thick alumina tunneling junction is broken, , as shown in Figure 6.4.

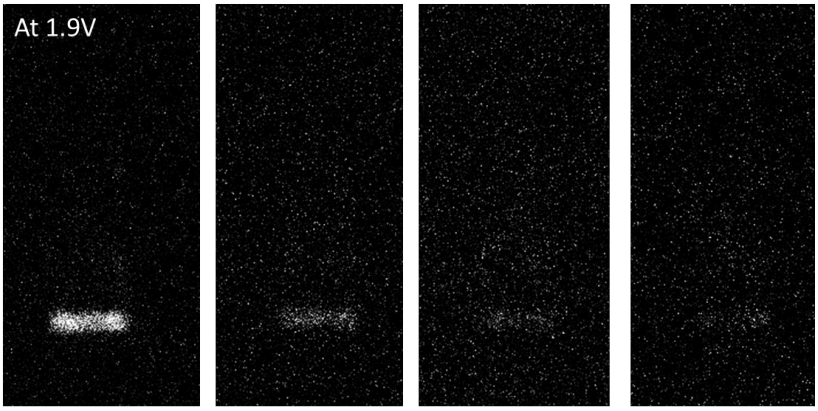

Figure 6.4 Light emission lifetime of *sample B*.

Sample C: Instead of using silicon as the substrate in *sample B*, for *sample C*, gold lines (30 nm in thickness) are patterned on glass slide as first electrode. Similarly, following with the ALD (5 nm alumina) and 30 nm gold deposited as second electrode.

The emitted light is collected from both sides of the sample, as shown in the Figure 6.5. Similarly, the turn on voltage is 3.5 V for the 5 nm thick alumina film. More light is observed from the grating area, as shown in Figure 6.5 c and d. The observed light is stronger in the pad area than that in the connection area, mostly due to the reason that the light in the connection area is distributed to both sides of the sample, while in the pad area, most of the light is transmitted to the topside of the sample.

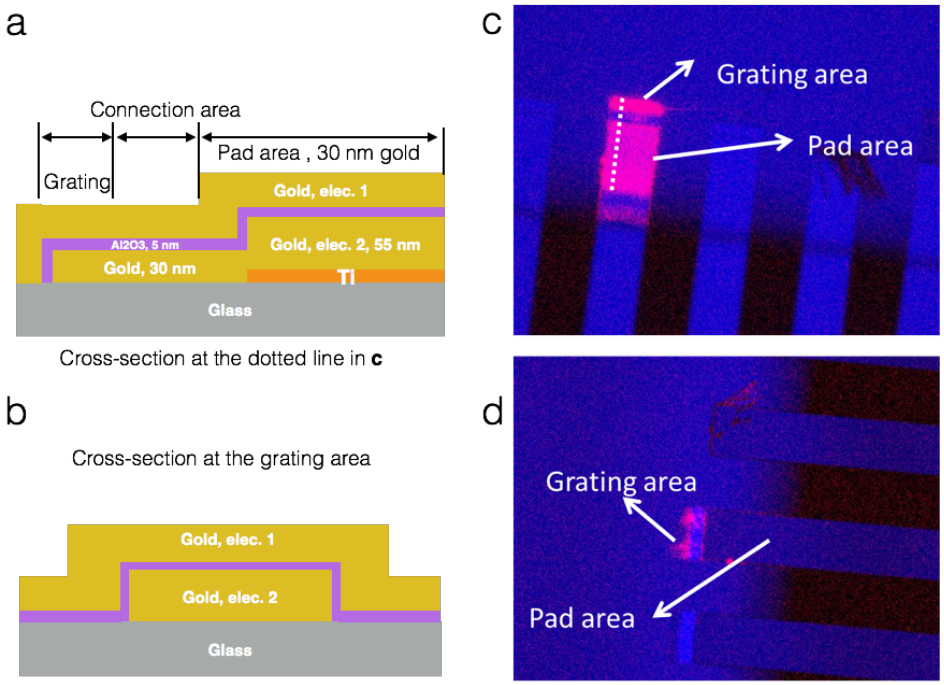

Figure 6.5 Schematic of *sample C* and tunneling-induced light emission measurement. a-b, schematic of *sample C* showing the top and cross-section in the patterned grating area of the planar nanogap. **c-d**, light emission observed from the metal side of the sample and from the glass side of the sample.

Sample D: Similar to *sample B*, except that in *Sample D* a gold film (55 nm) with adhesion layer is deposited underneath the patterned gold lines, shown in Figure 6.6a and b. A gold film is deposited before patterning of the grating, in the purpose of reflecting more emitted to the top of the sample. The alumina thickness inside the nanogap is 5 nm. Similarly, the turn on voltage for the sample with 5 nm thick alumina film is 3.5 V. However, it can be seen that from Figure 6.6c, the efficiency of light emission is still quite low.

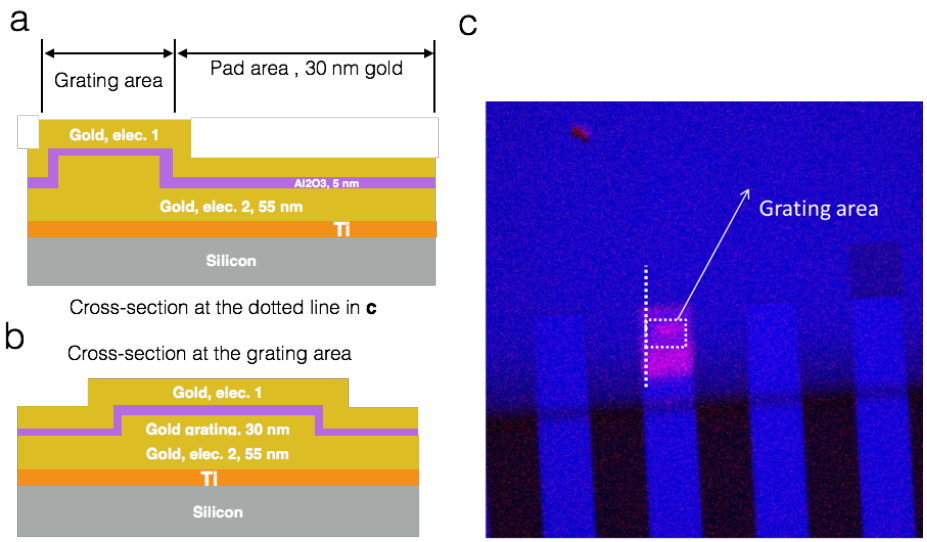

Figure 6.6 Schematic of *sample D* and tunneling-induced light emission measurement.

In this section, four different sets of planar nanogap samples are fabricated to study tunneling-induced light emission through nanogaps. It is demonstrated that for alumina thickness of 5 nm, the quality of alumina is consistent throughout different sets of samples. It is also noticed that the quantum efficiency and lifetime of the device are still low. Possible reasons might be the contamination of gold film during patterning and pinholes in ALD deposited films, etc.

6.3 Conclusions

In this chapter, fabrication and applications of electrically addressable nanogaps are discussed. The centimeter long nanogap is demonstrated as a very convenient substrate to

make chip scale platforms for manipulation of nano particles, which could lead to many applications in the biomedical applications. Furthermore, various designs have been tested to fabricate samples for tunneling-induced light emission. The experimental experiences can be very helpful for further study in this area.

CHAPTER 7

7. Summary and Future Directions

This chapter summarizes the nanogap research introduced in the previous chapters and discusses several future research directions.

7.1 Summary

This thesis presents new fabrication methods based on atomic layer lithography to make metal–insulator –metal nanogap structures and introduced the applications of the nanogap structures for enhanced light-matter interactions. My research focuses on design, fabrication, and characterization of the nanogap structures, which enable light to be squeezed into nanometer-scale volumes and create high intensity hot spots. The vertical and buried nanogap arrays are demonstrated to have huge field enhancement inside and at the vicinity of the nanogap area, demonstrated both by experimental measurements and modeling. This extreme confinement of light is applied to areas such as optical sensing of molecules, thin film sensing, optical electric field enhanced spectroscopy, and active manipulation of nano materials, etc.

The ALD-based patterning techniques remove one of the largest obstacles to the experimental studies and real world applications of the enhanced light-matter interactions

in the tightly confined optical fields. Those techniques are also wafer scale, high throughput, and low cost fabrication methods, which could open up the possibility to the regime where tunneling-induced emission and optical rectification become significant. It is expected that these new fabrication techniques and knowledge gained from such structures will directly and indirectly benefit the future work on harnessing optical energy inside nanostructures and electronic chips.

7.2 Future directions

7.2.1 Electrically addressable nanogap fabrication and applications

As discussed in Chapter 6, electrons tunneling through a nanometer-thick dielectric film in the nanogap structure can emit light. Our atomic layer lithography method is a possible solution to the challenge of the study and applications of the tunneling-induced light emission by providing an easier and more controllable way to make electrically addressable nanogaps. Besides tunneling-induced light emission, various other applications can be developed from electrically addressable nanogaps, such as electrically controllable optical interaction of light with nano materials.

In this section, a possible solution to make planar nanogap structure for tunneling-induced light emission will be discussed. And then another electrically addressable

vertical nanogap structures will be fabricated, on which the electrical bias, light and nano materials can be easily applied to the substrate to enhance the interaction between the electrical filed and the interested nano materials.

First, to make electrically addressable planar nanogap, one possible method is to combine stencil lithography, template stripping and ALD. Template stripping and atomic layer deposition provide ultra-smooth metal surface and ultra-thin dielectric film. Stencil lithography is a method that uses a shadowing mask (stencils) with nano/micro meter size apertures. As a simple and parallel lithography method, there is no need for resist processing or heating of the substrate. With a prefabricated shadowing mask, planar nanogap structures could be easily made on the prepared substrate, i.e. dielectric layer coated ultra-smooth metal surface.

As shown in Figure 7.1a, grating patterns are made on a suspended silicon nitride (Si_3N_4) film on top of a silicon wafer as stencils. Then the stencil is put to a close contact to the alumina coated template-stripped gold film. A thin gold film is deposited through the stencil, showing in Figure 7.1b. It can be seen that not only the open area is deposited with gold, areas around the pattern areas are also deposited with small gold particles, mostly due to the shadowing effect. For stencil lithography, proper distance between the stencil and the substrate is a critical parameter to nicely replicate the pattern on the

shadow mask. The deposition method is critical too. Usually, more directional deposition tools, such as an e-beam evaporator, work better than a sputtering machine. The temperature of the substrate also affects the deposition of metal. Hot substrate always provides more energy to the deposited metal particles and results in spreading of the metal deposition. Those parameters should be carefully controlled in the future study. More details about the fabrication process are described in A.9.

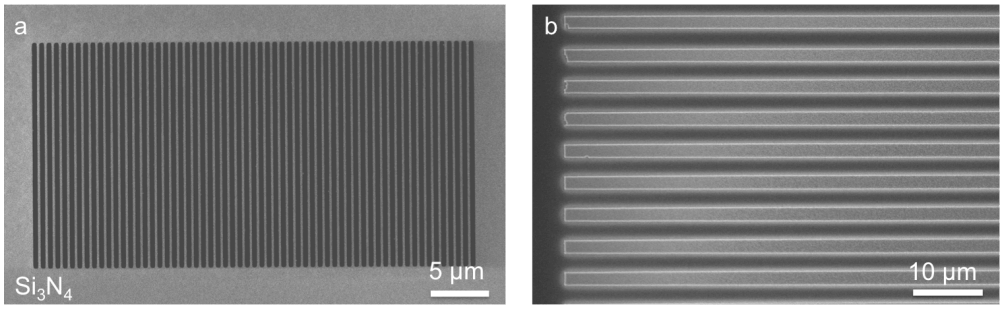

Figure 7.1 Preliminary results of planar nanogap fabricated by stencil lithography. **a**, Suspended silicon nitride film made by e-beam lithography and reactive ion etching. **b**, Au stripes deposited on top of alumina coated ultra-smooth template-stripped gold film.

Stencil lithography could be an alternative way to make planar nanogap structures rather than using e-beam lithography (described in section 3.3). The method not only avoids the expensive and complicated e-beam lithography, it also eliminates possible contaminations to the dielectric layer, for example, leaving a thin layer of resist residue if otherwise using lithography method to pattern the top metal layer. For an ultra thin

nanogap, the resist residue thickness could be comparable to the thickness of the thin dielectric layer.

Another possible future study is to make electrically addressable vertical nanogap array. Besides the nanogap with electrodes fabricated from a linear chain of nanogaps as discussed in section 6.1, annular nanogap arrays can be fabricated to satisfy different applications. As shown in Figure 7.2a, electrodes for annular nanogap array are fabricated. First, annular nanogap array is made on glass substrate with atomic layer lithography. The annular nanogap array is then used as a substrate for further patterning of electrodes. As shown in the insert of Figure 7.2a, the schematic of the structure shows a more clear view, where an electrode is patterned to reach the metal (2^{nd} metal layer in atomic layer lithography) inside each annular nanogap. There is a thick insulator layer (200nm in thickness, purple color in the insert figure) – silica, deposited by e-beam evaporation – to completely insulate the electrode that connects 1^{st} metal layer and the 2^{nd} metal layer. Figure 7.2b shows the SEM of an electrically addressable annular nanogap. After lithography, the device is optically tested. As shown in Figure 7.2c-e, with random polarized light, the whole annular nanogap transmits light (except the area being covered with patterned metal as electrode). With linear polarized light, only the nanogap area that is perpendicular to the polarized light transmits light, which demonstrates the excitation

of gap plasmon inside the nanogap. The IV curve of the devices are also measured, showing good insulation between the metal films inside and outside of the annular nanogap, with alumina thickness around 10 nm and above.

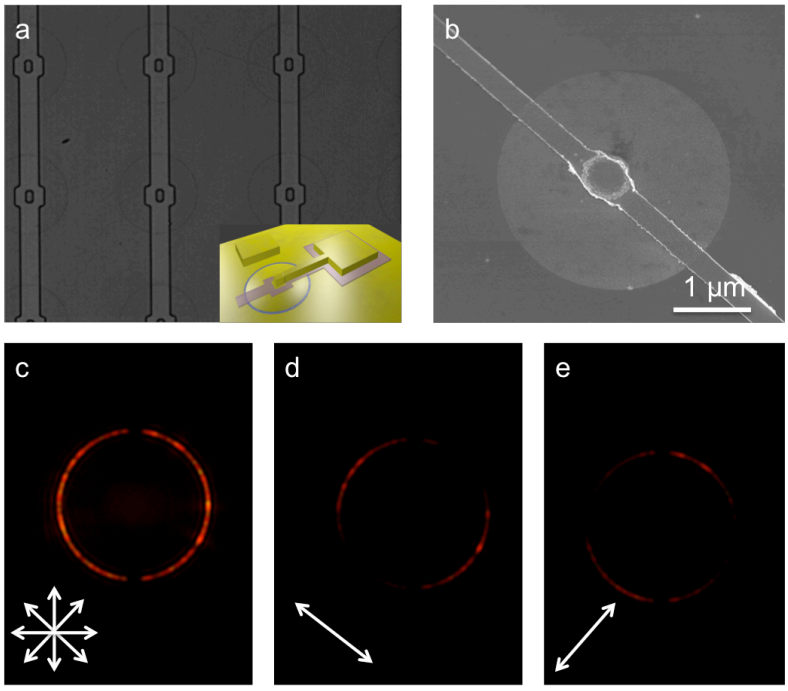

Figure 7.2 Preliminary results of electrically addressable annular nanogap array. a, Optical microscope image of electrically addressable annular nanogap array. The insert shows the design of the electrodes. **b**, SEM of electrically addressable annular nanogap. **c-e** Optical transmission measurement shown the function of the annular nanogap.

7.2.2 Nanogap dimer fabricated with FIB

Using atomic layer lithography, it is quite easy to make nanogaps in large scale. The metal films at both sides of the nanogap can be removed by FIB, to make nano antennas with a gap (also called nano antenna dimer) in between. Different shapes and sizes of

nano antenna dimers are widely used as a plasmonics platform to enhance light-matter interactions. Comparing to nanogap structures with continuous metal film, the nanogap between two nano dimers has it own advantages. One example is if the nano particles are designed in right size, its local surface plasmon resonance could be coupled to gap plasmon, which might infer even higher field enhancement.

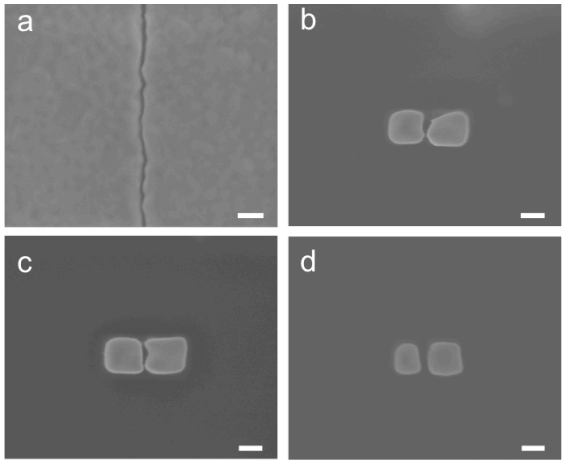

Figure 7.3 Preliminary results of nanogap dimers fabricated from atomic layer lithography fabricated nanogap. a, 20 nm gap between two gold films. **b-d**, The metal around the nanogap is removed by FIB milling. The scale bar in each figure is 100 nm.

The nanogap structures fabricated with atomic layer lithography are extremely suitable to make dimer structures. Furthermore, hybrid nano antenna dimer can be made if different metals are deposited during atomic layer lithography. Figure 7.3 shows some preliminary results of using FIB to remove the surrounded metal. During FIB milling process, the metal at the corners of the pattern is rounded due to the damage from ion

beam milling. Instead of using FIB, e-beam lithography can be used to pattern resist as a mask for etching, and then the metal around can be removed by ion milling etching or wet etching methods.

Bibliography

1 Xu, H. X., Bjerneld, E. J., Kall, M. & Borjesson, L. Spectroscopy of single hemoglobin molecules by surface enhanced Raman scattering. *Physical Review Letters* **83**, 4357-4360, doi:10.1103/PhysRevLett.83.4357 (1999).

2 Haynes, C. L., McFarland, A. D. & Van Duyne, R. P. Surface-enhanced Raman spectroscopy. *Analytical Chemistry* **77**, 338A-346A, doi:10.1021/ac053456d (2005).

3 Liu, Z. W., Lee, H., Xiong, Y., Sun, C. & Zhang, X. Far-field optical hyperlens magnifying sub-diffraction-limited objects. *Science* **315**, 1686-1686, doi:10.1126/science.1137368 (2007).

4 Atwater, H. A. & Polman, A. Plasmonics for improved photovoltaic devices (vol 9, pg 205, 2010). *Nature Materials* **9**, 865-865, doi:10.1038/nmat2866 (2010).

5 Bozhevolnyi, S. I., Volkov, V. S., Devaux, E., Laluet, J. Y. & Ebbesen, T. W. Channel plasmon subwavelength waveguide components including interferometers and ring resonators. *Nature* **440**, 508-511, doi:10.1038/nature04594 (2006).

6 Righini, M., Zelenina, A., Girard, C. & Quidant, R. Parallel and selective trapping in a patterned plasmonic landscape. *Nature Physics* **3**, 477-480, doi:10.1038/nphys624 (2007).

7 Lambe, J. & McCarthy, S. L. Light-emission from inelastic electron-tunneling. *Physical Review Letters* **37**, 923-925, doi:DOI 10.1103/PhysRevLett.37.923 (1976).

8 Challener, W. A. *et al.* Heat-assisted magnetic recording by a near-field transducer with efficient optical energy transfer (vol 3, pg 220, 2009). *Nature Photonics* **3**, 303-303, doi:10.1038/nphoton.2009.71 (2009).

9 Mansuripur, M. *et al.* Plasmonic nano-structures for optical data storage. *Optics Express* **17**, 14001-14014, doi:10.1364/oe.17.014001 (2009).

10 Brolo, A. G. Plasmonics for future biosensors. *Nature Photonics* **6**, 709-713, doi:10.1038/nphoton.2012.266 (2012).

11 Ciraci, C. *et al.* Probing the Ultimate Limits of Plasmonic Enhancement. *Science* **337**, 1072-1074, doi:10.1126/science.1224823 (2012).

12 Kern, J. *et al.* Atomic-Scale Confinement of Resonant Optical Fields. *Nano Letters* **12**, 5504-5509, doi:10.1021/nl302315g (2012).

13 Pelton, M., Aizpurua, J. & Bryant, G. Metal-nanoparticle plasmonics. *Laser & Photonics Reviews* **2**, 136-159, doi:10.1002/lpor.200810003 (2008).

14 Maier, S. A. *et al.* Local detection of electromagnetic energy transport below the diffraction limit in metal nanoparticle plasmon waveguides. *Nature Materials* **2**, 229-232, doi:10.1038/nmat852 (2003).

15 Halas, N. J., Lal, S., Chang, W. S., Link, S. & Nordlander, P. Plasmons in Strongly Coupled Metallic Nanostructures. *Chemical Reviews* **111**, 3913-3961, doi:10.1021/cr200061k (2011).

16 Michaels, A. M., Jiang, J. & Brus, L. Ag nanocrystal junctions as the site for surface-enhanced Raman scattering of single Rhodamine 6G molecules. *Journal of Physical Chemistry B* **104**, 11965-11971, doi:10.1021/jp0025476 (2000).

17 Ebbesen, T. W., Lezec, H. J., Ghaemi, H. F., Thio, T. & Wolff, P. A. Extraordinary optical transmission through sub-wavelength hole arrays. *Nature* **391**, 667-669, doi:10.1038/35570 (1998).

18 Barnes, W. L., Dereux, A. & Ebbesen, T. W. Surface plasmon subwavelength optics. *Nature* **424**, 824-830, doi:10.1038/nature01937 (2003).

19 Garcia-Vidal, F. J., Martin-Moreno, L., Ebbesen, T. W. & Kuipers, L. Light passing through subwavelength apertures. *Reviews of Modern Physics* **82**, 729-787, doi:10.1103/RevModPhys.82.729 (2010).

20 Xie, Y., Zakharian, A. R., Moloney, J. V. & Mansuripur, M. Transmission of light through slit apertures in metallic films. *Optics Express* **12**, 6106-6121, doi:10.1364/opex.12.006106 (2004).

21 Seo, M. A. *et al.* Terahertz field enhancement by a metallic nano slit operating beyond the skin-depth limit. *Nature Photonics* **3**, 152-156, doi:10.1038/nphoton.2009.22 (2009).

22 Miyazaki, H. T. & Kurokawa, Y. Squeezing visible light waves into a 3-nm-thick and 55-nm-long plasmon cavity. *Physical Review Letters* **96**, doi:10.1103/PhysRevLett.96.097401 (2006).

23 Schuller, J. A. *et al.* Plasmonics for extreme light concentration and manipulation. *Nature Materials* **9**, 193-204, doi:10.1038/nmat2630 (2010).

24 Ward, D. R., Huser, F., Pauly, F., Cuevas, J. C. & Natelson, D. Optical rectification and field enhancement in a plasmonic nanogap. *Nature Nanotechnology* **5**, 732-736, doi:10.1038/nnano.2010.176 (2010).

25 Novotny, L. & van Hulst, N. Antennas for light. *Nature Photonics* **5**, 83-90, doi:10.1038/nphoton.2010.237 (2011).

26 Xu, H. X. & Kall, M. Surface-plasmon-enhanced optical forces in silver nanoaggregates. *Physical Review Letters* **89**, doi:10.1103/PhysRevLett.89.246802 (2002).

27 Ward, D. R. *et al.* Electromigrated nanoscale gaps for surface-enhanced Raman spectroscopy. *Nano Letters* **7**, 1396-1400, doi:10.1021/nl070625w (2007).

28 Duan, H. G., Hu, H. L., Kumar, K., Shen, Z. X. & Yang, J. K. W. Direct and Reliable Patterning of Plasmonic Nanostructures with Sub-10-nm Gaps. *Acs Nano* **5**, 7593-7600, doi:10.1021/nn2025868 (2011).

29 Savage, K. J. *et al.* Revealing the quantum regime in tunnelling plasmonics. *Nature* **491**, 574-577, doi:10.1038/nature11653 (2012).

30 Drude, V. P. Vol. 306 556-613 (Annalen der Physik, 1900).

31 Lindquist, N. C. *et al.* Tip-based plasmonics: squeezing light with metallic nanoprobes. *Laser & Photonics Reviews* **7**, 453-477, doi:10.1002/lpor.201209044 (2013).

32 Stuart, B. *Infrared spectroscopy : fundamentals and applications*. (Chichester, West Sussex, England ; Hoboken, N.J. : J. Wiley 2004).

33 Aroca & Ricardo. *Surface-Enhanced Vibrational Spectroscopy*. 1 edn, (John Wiley & Sons, Ltd, 2006).

34 Hatta, A., Ohshima, T. & Suetaka, W. Observation of the enhanced infrared-absorption of para-nitrobenzoate on Ag island films with an ATR technique. *Applied Physics a-Materials Science & Processing* **29**, 71-75, doi:10.1007/bf00632429 (1982).

35 Hartstein, A., Kirtley, J. R. & Tsang, J. C. Enhancement of the infrared-absorption from molecular monolayers with thin metal overlays. *Physical Review Letters* **45**, 201-204, doi:10.1103/PhysRevLett.45.201 (1980).

36 Coe, J. V., Heer, J. M., Teeters-Kennedy, S., Tian, H. & Rodriguez, K. R. Extraordinary transmission of metal films with arrays of subwavelength holes. *Annual Review of Physical Chemistry* **59**, 179-202, doi:10.1146/annurev.physchem.59.032607.093703 (2008).

37 Adato, R. *et al.* Ultra-sensitive vibrational spectroscopy of protein monolayers with plasmonic nanoantenna arrays. *Proceedings of the National Academy of Sciences of the United States of America* **106**, 19227-19232, doi:DOI 10.1073/pnas.0907459106 (2009).

38 Huck, C. *et al.* Surface-Enhanced Infrared Spectroscopy Using Nanometer-Sized Gaps. *Acs Nano* **8**, 4908-4914, doi:10.1021/nn500903v (2014).

39 Raman, C. & Krishnan, K. A new type of secondary radiation. **121**, 501-502, doi:10.1038/121501c0 (1928).

40 Jeanmaire, D. L. & Van Duyne, R. P. Surface Raman spectroelectrochemistry Part I Heterocyclic, aromatic, and aliphatic amines adsorbed on the anodized silver electrode. 1-20, doi:10.1016/S0022-0728(77)80224-6 (1977).

41 Albrecht, M. G. & Creighton, J. A. Anomalously intense Raman-spectra of pyridine at a silver electrode. *Journal of the American Chemical Society* **99**, 5215-5217, doi:10.1021/ja00457a071 (1977).

42 Zhang, X. Y., Zhao, J., Whitney, A. V., Elam, J. W. & Van Duyne, R. P. Ultrastable substrates for surface-enhanced Raman spectroscopy: Al2O3 overlayers fabricated by atomic layer deposition yield improved anthrax biomarker detection. *Journal of the American Chemical Society* **128**, 10304-10309, doi:10.1021/ja0638760 (2006).

43 Lindquist, N. C., Nagpal, P., McPeak, K. M., Norris, D. J. & Oh, S.-H. Engineering metallic nanostructures for plasmonics and nanophotonics. *Reports on Progress in Physics* **75**, doi:10.1088/0034-4885/75/3/036501 (2012).

44 Puurunen, R. L. Surface chemistry of atomic layer deposition: A case study for the trimethylaluminum/water process. *Journal of Applied Physics* **97**, doi:10.1063/1.1940727 (2005).

45 Im, H., Bantz, K. C., Lindquist, N. C., Haynes, C. L. & Oh, S. H. Vertically Oriented Sub-10-nm Plasmonic Nanogap Arrays. *Nano Letters* **10**, 2231-2236, doi:10.1021/nl1012085 (2010).

46 Chen, X. S. *et al.* Atomic layer lithography of wafer-scale nanogap arrays for extreme confinement of electromagnetic waves. *Nature Communications* **4**, doi:10.1038/ncomms3361 (2013).

47 Chen, X. S. *et al.* Squeezing Millimeter Waves through a Single, Nanometer-wide, Centimeter-long Slit. *Scientific Reports* **4**, doi:10.1038/srep06722 (2014).

48 Nishikawa, Y., Nagasawa, T., Fujiwara, K. & Osawa, M. Silver island films for surface-enhanced infrared-absorption spectroscopy - effect of island morphology on the absorption enhancement. *Vibrational Spectroscopy* **6**, 43-53, doi:10.1016/0924-2031(93)87021-k (1993).

49 Brown, L. V. *et al.* Surface-Enhanced Infrared Absorption Using Individual Cross Antennas Tailored to Chemical Moieties. *Journal of the American Chemical Society* **135**, 3688-3695, doi:Doi 10.1021/Ja312694g (2013).

50 Aksu, S. *et al.* High-Throughput Nanofabrication of Infrared Plasmonic Nanoantenna Arrays for Vibrational Nanospectroscopy. *Nano Letters* **10**, 2511-2518, doi:10.1021/nl101042a (2010).

51 Neubrech, F. *et al.* Resonant Plasmonic and Vibrational Coupling in a Tailored Nanoantenna for Infrared Detection. *Physical Review Letters* **101**, doi:10.1103/PhysRevLett.101.157403 (2008).

52 Cubukcu, E., Zhang, S., Park, Y. S., Bartal, G. & Zhang, X. Split ring resonator sensors for infrared detection of single molecular monolayers. *Applied Physics Letters* **95**, doi:Artn 043113 Doi 10.1063/1.3194154 (2009).

53 Schuck, P. J., Fromm, D. P., Sundaramurthy, A., Kino, G. S. & Moerner, W. E. Improving the mismatch between light and nanoscale objects with gold bowtie nanoantennas. *Abstracts of Papers of the American Chemical Society* **229**, U730-U730 (2005).

54 Koh, A. L., Fernandez-Dominguez, A. I., McComb, D. W., Maier, S. A. & Yang, J. K. W. High-Resolution Mapping of Electron-Beam-Excited Plasmon Modes in Lithographically Defined Gold Nanostructures. *Nano Letters* **11**, 1323-1330, doi:10.1021/nl104410t (2011).

55 Choo, H. *et al.* Nanofocusing in a metal-insulator-metal gap plasmon waveguide with a three-dimensional linear taper. *Nature Photonics* **6**, 837-843, doi:10.1038/nphoton.2012.277 (2012).

56 Melli, M. *et al.* Reaching the Theoretical Resonance Quality Factor Limit in Coaxial Plasmonic Nanoresonators Fabricated by Helium Ion Lithography. *Nano Letters* **13**, 2687-2691, doi:10.1021/nl400844a (2013).

57 Ward, D. R. *et al.* Electromigrated nanoscale gaps for surface-enhanced Raman spectroscopy. *Nano Letters* **7**, 1396-1400, doi:10.1021/nl070625w (2007).

58 Wang, H., Levin, C. S. & Halas, N. J. Nanosphere arrays with controlled sub-10-nm gaps as surface-enhanced Raman spectroscopy substrates. *Journal of the American Chemical Society* **127**, 14992-14993, doi:10.1021/ja055633y (2005).

59 Hoffmann, J. M., Janssen, H., Chigrin, D. N. & Taubner, T. Enhanced infrared spectroscopy using small-gap antennas prepared with two-step evaporation nanosphere lithography. *Optics Express* **22**, 14425-14432, doi:10.1364/oe.22.014425 (2014).

60 Im, H. *et al.* Self-Assembled Plasmonic Nanoring Cavity Arrays for SERS and LSPR Biosensing. *Advanced Materials* **25**, 2678-2685, doi:10.1002/adma.201204283 (2013).

61 Ikeda, K. *et al.* Controlled thermal emission of polarized infrared waves from arrayed plasmon nanocavities. *Applied Physics Letters* **92**, doi:02111710.1063/1.2834903 (2008).

62 Nagpal, P., Lindquist, N. C., Oh, S. H. & Norris, D. J. Ultrasmooth Patterned Metals for Plasmonics and Metamaterials. *Science* **325**, 594-597, doi:10.1126/science.1174655 (2009).

63 Lindquist, N. C., Johnson, T. W., Norris, D. J. & Oh, S.-H. Monolithic Integration of Continuously Tunable Plasmonic Nanostructures. *Nano Letters* **11**, 3526-3530, doi:10.1021/nl2005737 (2011).

64 Bao, W. *et al.* Mapping Local Charge Recombination Heterogeneity by Multidimensional Nanospectroscopic Imaging. *Science* **338**, 1317-1321, doi:10.1126/science.1227977 (2012).

65 Suh, J. Y. *et al.* Extraordinary Nonlinear Absorption in 3D Bowtie Nanoantennas. *Nano Letters* **12**, 269-274, doi:10.1021/nl2034915 (2012).

66 Berthelot, J. *et al.* Three-dimensional manipulation with scanning near-field optical nanotweezers. *Nature Nanotechnology* **9**, 295-299, doi:10.1038/nnano.2014.24 (2014).

67 Yin, Y. D. & Xia, Y. N. Self-assembly of spherical colloids into helical chains with well-controlled handedness. *Journal of the American Chemical Society* **125**, 2048-2049, doi:10.1021/ja029408h (2003).

68 Lassiter, J. B. *et al.* Plasmonic Waveguide Modes of Film-Coupled Metallic Nanocubes. *Nano Letters* **13**, 5866-5872, doi:10.1021/nl402660s (2013).

69 Moreau, A. *et al.* Controlled-reflectance surfaces with film-coupled colloidal nanoantennas. *Nature* **492**, 86-+, doi:10.1038/nature11615 (2012).

70 Rose, A. *et al.* Control of Radiative Processes Using Tunable Plasmonic Nanopatch Antennas. *Nano Letters* **14**, 4797-4802, doi:10.1021/nl501976f (2014).

71 Ciracì, C. *et al.* Film-coupled nanoparticles by atomic layer deposition: comparison with organic spacing layers. *Applied Physics Letters* **104**, 023109, doi:10.1063/1.4861849 (2014).

72 Lassiter, J. B. *et al.* Third-Harmonic Generation Enhancement by Film-Coupled Plasmonic Stripe Resonators. *Acs Photonics* **1**, 1212-1217, doi:10.1021/ph500276v (2014).

73 Lumdee, C., Yun, B. F. & Kik, P. G. Wide-Band Spectral Control of Au Nanoparticle Plasmon Resonances on a Thermally and Chemically Robust Sensing Platform. *Journal of Physical Chemistry C* **117**, 19127-19133, doi:10.1021/jp4056522 (2013).

74 George, S. M. Atomic layer deposition: an overview. *Chemical Reviews* **110**, 111-131, doi:Doi 10.1021/Cr900056b (2010).

75 Le, F. *et al.* Metallic nanoparticle arrays: A common substrate for both surface-enhanced Raman scattering and surface-enhanced infrared absorption. *Acs Nano* **2**, 707-718, doi:10.1021/nn800047e (2008).

76 Johnson, T. *et al.* Highly Reproducible Near-Field Optical Imaging with Sub-20-nm Resolution Based on Template-Stripped Gold Pyramids. *Acs Nano* **6**, 9168-9174, doi:10.1021/nn303496g (2012).

77 Bharadwaj, P., Bouhelier, A. & Novotny, L. Electrical Excitation of Surface Plasmons. *Physical Review Letters* **106**, doi:10.1103/PhysRevLett.106.226802 (2011).

78 Knight, M. W., Sobhani, H., Nordlander, P. & Halas, N. J. Photodetection with Active Optical Antennas. *Science* **332**, 702-704, doi:10.1126/science.1203056 (2011).

79 Kurokawa, Y. & Miyazaki, H. T. Metal-insulator-metal plasmon nanocavities: Analysis of optical properties. *Physical Review B* **75**, doi:03541110.1103/PhysRevB.75.035411 (2007).

80 de Waele, R., Burgos, S. P., Polman, A. & Atwater, H. A. Plasmon Dispersion in Coaxial Waveguides from Single-Cavity Optical Transmission Measurements. *Nano Letters* **9**, 2832-2837, doi:10.1021/nl900597z (2009).

81 Alaee, R. *et al.* Deep-Subwavelength Plasmonic Nanoresonators Exploiting Extreme Coupling. *Nano Letters* **13**, 3482-3486, doi:Doi 10.1021/Nl4007694 (2013).

82 Petschulat, J. *et al.* Plasmonic modes of extreme subwavelength nanocavities. *Optics Letters* **35**, 2693-2695 (2010).

83 Kischkat, J. *et al.* Mid-infrared optical properties of thin films of aluminum oxide, titanium dioxide, silicon dioxide, aluminum nitride, and silicon nitride. *Applied Optics* **51**, 6789-6798 (2012).

84 Olmon, R. L. *et al.* Optical dielectric function of gold. *Physical Review B* **86**, doi:Doi 10.1103/Physrevb.86.235147 (2012).

85 Ciraci, C., Lassiter, J. B., Moreau, A. & Smith, D. R. Quasi-analytic study of scattering from optical plasmonic patch antennas. *Journal of Applied Physics* **114**, doi:10.1063/1.4827185 (2013).

86 Zhang, X. C. Terahertz wave imaging: horizons and hurdles. *Physics in Medicine and Biology* **47**, 3667-3677, doi:10.1088/0031-9155/47/21/301 (2002).

87 Tribe, W. R., Newnham, D. A., Taday, P. F. & Kemp, M. C. in *Conference on Terahertz and Gigahertz Electronics and Photonics III.* 168-176 (2004).

88 Leahy-Hoppa, M. R. Terahertz for weapon and explosive detection. *Critical Infrastructure Security: Assessment, Prevention, Detection, Response* **54**, 207-220 (2012).

89 Kleine-Ostmann, T. & Nagatsuma, T. A Review on Terahertz Communications Research. *Journal of Infrared Millimeter and Terahertz Waves* **32**, 143-171, doi:10.1007/s10762-010-9758-1 (2011).

90 Jackson, J. B. *et al.* Terahertz imaging for non-destructive evaluation of mural paintings. *Optics Communications* **281**, 527-532, doi:10.1016/j.optcom.2007.10.049 (2008).

91 Yan, Z., Ying, Y., Zhang, H. & Yu, H. in *Conference on Terahertz Physics, Devices, and Systems.* U147-U156 (2006).

92 Wu, Q., Hewitt, T. D. & Zhang, X. C. Two-dimensional electro-optic imaging of THz beams. *Applied Physics Letters* **69**, 1026-1028, doi:10.1063/1.116920 (1996).

93 Mittleman, D. M., Jacobsen, R. H. & Nuss, M. C. T-ray imaging. *Ieee Journal of Selected Topics in Quantum Electronics* **2**, 679-692, doi:10.1109/2944.571768 (1996).

94 Grischkowsky, D., Keiding, S., Vanexter, M. & Fattinger, C. Far-Infrared Time-Domain Spectroscopy with Terahertz Beams of Dielectrics and Semiconductors. *Journal of the Optical Society of America B-Optical Physics* **7**, 2006-2015, doi:Doi 10.1364/Josab.7.002006 (1990).

95 Kyoung, J. S., Seo, M. A., Park, H. R., Ahn, K. J. & Kim, D. S. Far field detection of terahertz near field enhancement of sub-wavelength slits using Kirchhoff integral formalism. *Optics Communications* **283**, 4907-4910, doi:DOI 10.1016/j.optcom.2010.08.008 (2010).

96 Shalaby, M. *et al.* Skirting terahertz waves in a photo-excited nanoslit structure. *Applied Physics Letters* **104**, doi:Artn 171115 Doi 10.1063/1.4871305 (2014).

97 Im, H., Lindquist, N. C., Lesuffleur, A. & Oh, S. H. Atomic Layer Deposition of Dielectric Overlayers for Enhancing the Optical Properties and Chemical Stability of Plasmonic Nanoholes. *Acs Nano* **4**, 947-954, doi:Doi 10.1021/Nn901842r (2010).

98 Kang, J. H., Kim, D. S. & Park, Q. H. Local Capacitor Model for Plasmonic Electric Field Enhancement. *Physical Review Letters* **102**, 093906, doi:Artn 093906 Doi 10.1103/Physrevlett.102.093906 (2009).

99 Koo, S., Kumar, M. S., Shin, J., Kim, D. & Park, N. Extraordinary Magnetic Field Enhancement with Metallic Nanowire: Role of Surface Impedance in Babinet's Principle for Sub-Skin-Depth Regime. *Physical Review Letters* **103**, doi:10.1103/PhysRevLett.103.263901 (2009).

100 Groner, M. D., Elam, J. W., Fabreguette, F. H. & George, S. M. Electrical characterization of thin Al_2O_3 films grown by atomic layer deposition on silicon and various metal substrates. *Thin Solid Films* **413**, 186-197, doi:Doi 10.1016/S0040-6090(02)00438-8 (2002).

101 Bareiss, M. *et al.* Printed array of thin-dielectric metal-oxide-metal (MOM) tunneling diodes. *Journal of Applied Physics* **110**, doi:10.1063/1.3615952 (2011).

102 Pendry, J. B., Aubry, A., Smith, D. R. & Maier, S. A. Transformation Optics and Subwavelength Control of Light. *Science* **337**, 549-552, doi:10.1126/science.1220600 (2012).

103 de Abajo, F. J. G. Nonlocal Effects in the Plasmons of Strongly Interacting Nanoparticles, Dimers, and Waveguides. *Journal of Physical Chemistry C* **112**, 17983-17987, doi:10.1021/jp807345h (2008).

104 Esteban, R., Borisov, A. G., Nordlander, P. & Aizpurua, J. Bridging quantum and classical plasmonics with a quantum-corrected model. *Nature Communications* **3**, 825, doi:Artn 825 Doi 10.1038/Ncomms1806 (2012).

105 Bharadwaj, P., Bouhelier, A. & Novotny, L. Electrical excitation of surface plasmons. *Physical Review Letters* **106**, 226802, doi:Artn 226802 Doi 10.1103/Physrevlett.106.226802 (2011).

106 Lee, S. H. *et al.* Switching terahertz waves with gate-controlled active graphene metamaterials. *Nature Materials* **11**, 936-941, doi:10.1038/nmat3433 (2012).

107 Liu, M. K. *et al.* Terahertz-field-induced insulator-to-metal transition in vanadium dioxide metamaterial. *Nature* **487**, 345-348, doi:10.1038/nature11231 (2012).

108 Yang, F. Z. & Sambles, J. R. Resonant transmission of microwaves through a narrow metallic slit. *Physical Review Letters* **89**, 063901, doi:Artn 063901 Doi 10.1103/Physrevlett.89.063901 (2002).

109 Aouani, H. *et al.* Ultrasensitive Broadband Probing of Molecular Vibrational Modes with Multifrequency Optical Antennas. *Acs Nano* **7**, 669-675, doi:10.1021/nn304860t (2013).

110 Aydin, K., Ferry, V. E., Briggs, R. M. & Atwater, H. A. Broadband polarization-independent resonant light absorption using ultrathin plasmonic super absorbers. *Nature Communications* **2**, 7, doi:10.1038/ncomms1528 (2011).

111 Haynes, C. L. & Van Duyne, R. P. Plasmon-sampled surface-enhanced Raman excitation spectroscopy. *Journal of Physical Chemistry B* **107**, 7426-7433, doi:10.1021/jp027749b (2003).

112 Osawa, M. Surface-enhanced infrared absorption. *Near-Field Optics and Surface Plasmon Polaritons* **81**, 163-187 (2001).

113 Giannini, V., Francescato, Y., Amrania, H., Phillips, C. C. & Maier, S. A. Fano Resonances in Nanoscale Plasmonic Systems: A Parameter-Free Modeling Approach. *Nano Letters* **11**, 2835-2840, doi:10.1021/nl201207n (2011).

114 Luk'yanchuk, B. *et al.* The Fano resonance in plasmonic nanostructures and metamaterials. *Nature Materials* **9**, 707-715, doi:10.1038/nmat2810 (2010).

115 Wu, C. H. *et al.* Fano-resonant asymmetric metamaterials for ultrasensitive spectroscopy and identification of molecular monolayers. *Nature Materials* **11**, 69-75, doi:10.1038/nmat3161 (2012).

116 Gramotnev, D. K. & Bozhevolnyi, S. I. Nanofocusing of electromagnetic radiation. *Nature Photonics* **8**, 14-23, doi:10.1038/nphoton.2013.232 (2014).

117 Bailo, E. & Deckert, V. Tip-enhanced Raman scattering. *Chemical Society Reviews* **37**, 921-930, doi:10.1039/b705967c (2008).

118 D'Andrea, C. *et al.* Optical Nanoantennas for Multiband Surface-Enhanced Infrared and Raman Spectroscopy. *Acs Nano* **7**, 3522-3531, doi:10.1021/nn4004764 (2013).

119 Chen, X. S., Ciraci, C., Smith, D. R. & Oh, S. H. Nanogap-Enhanced Infrared Spectroscopy with Template-Stripped Wafer-Scale Arrays of Buried Plasmonic Cavities. *Nano Letters* **15**, 107-113, doi:10.1021/nl503126s (2015).

120 Park, H. R. *et al.* Perfect Extinction of Terahertz Waves in Monolayer Graphene over 2-nm-Wide Metallic Apertures. *Advanced Optical Materials* **3**, 667-673, doi:10.1002/adom.201400546 (2015).

121 Barik, A. *et al.* Dielectrophoresis-Enhanced Plasmonic Sensing with Gold Nanohole Arrays. *Nano Letters* **14**, 2006-2012, doi:10.1021/nl500149h (2014).

122 Park, H. R., Chen, X. S., Nguyen, N. C., Peraire, J. & Oh, S. H. Nanogap-Enhanced Terahertz Sensing of 1 nm Thick (lambda/10(6)) Dielectric Films. *Acs Photonics* **2**, 417-424, doi:10.1021/ph500464j (2015).

123 Im, H., Bantz, K. C., Lindquist, N. C., Haynes, C. L. & Oh, S. H. Vertically Oriented Sub-10-nm Plasmonic Nanogap Arrays. *Nano Letters* **10**, 2231-2236, doi:10.1021/nl1012085 (2010).

124 Baik, J. M., Lee, S. J. & Moskovits, M. Polarized Surface-Enhanced Raman Spectroscopy from Molecules Adsorbed in Nano-Gaps Produced by

Electromigration in Silver Nanowires. *Nano Letters* **9**, 672-676, doi:10.1021/nl803145d (2009).

125 Han, S. W., Lee, S. J. & Kim, K. Self-assembled monolayers of aromatic thiol and selenol on silver: Comparative study of adsorptivity and stability. *Langmuir* **17**, 6981-6987, doi:10.1021/la010464q (2001).

126 Sabatani, E., Cohenboulakia, J., Bruening, M. & Rubinstein, I. Thioaromatic monolayers on gold - a new family of self-assembling monolayers. *Langmuir* **9**, 2974-2981, doi:10.1021/la00035a040 (1993).

127 Nara, J., Higai, S., Morikawa, Y. & Ohno, T. Density functional theory investigation of benzenethiol adsorption on Au(111). *Journal of Chemical Physics* **120**, 6705-6711, doi:10.1063/1.1651064 (2004).

128 Tame, M. S. *et al.* Quantum plasmonics. *Nature Physics* **9**, 329-340, doi:10.1038/nphys2615 (2013).

129 Fleger, Y., Mastai, Y., Rosenbluh, M. & Dressler, D. H. SERS as a probe for adsorbate orientation on silver nanoclusters. *Journal of Raman Spectroscopy* **40**, 1572-1577, doi:10.1002/jrs.2300 (2009).

130 Bryant, M. A., Joa, S. L. & Pemberton, J. E. Raman-scattering from monolayer films of thiophenol and 4-mercaptopyridine at Pt surfaces. *Langmuir* **8**, 753-756, doi:10.1021/la00039a002 (1992).

131 Homola, J. Surface plasmon resonance sensors for detection of chemical and biological species. *Chemical Reviews* **108**, 462-493, doi:Doi 10.1021/Cr068107d (2008).

132 O'Hara, J. F., Withayachumnankul, W. & Al-Naib, I. A Review on Thin-film Sensing with Terahertz Waves. *Journal of Infrared Millimeter and Terahertz Waves* **33**, 245-291, doi:DOI 10.1007/s10762-012-9878-x (2012).

133 Withayachumnankul, W. *et al.* Sub-diffraction thin-film sensing with planar terahertz metamaterials. *Optics Express* **20**, 3345-3352 (2012).

134 Withayachumnankul, W., O'Hara, J. F., Cao, W., Al-Naib, I. & Zhang, W. L. Limitation in thin-film sensing with transmission-mode terahertz time-domain spectroscopy. *Optics Express* **22**, 972-986, doi:Doi 10.1364/Oe.22.000972 (2014).

135 Nagel, M. *et al.* Integrated planar terahertz resonators for femtomolar sensitivity label-free detection of DNA hybridization. *Applied Optics* **41**, 2074-2078, doi:Doi 10.1364/Ao.41.002074 (2002).

136 Novoselov, K. S. *et al.* A roadmap for graphene. *Nature* **490**, 192-200, doi:10.1038/nature11458 (2012).

137 Pei, S. F., Zhao, J. P., Du, J. H., Ren, W. C. & Cheng, H. M. Direct reduction of graphene oxide films into highly conductive and flexible graphene films by hydrohalic acids. *Carbon* **48**, 4466-4474, doi:10.1016/j.carbon.2010.08.006 (2010).

138 Liao, L. *et al.* High-speed graphene transistors with a self-aligned nanowire gate. *Nature* **467**, 305-308, doi:10.1038/nature09405 (2010).

139 Echtermeyer, T. J. *et al.* Strong plasmonic enhancement of photovoltage in graphene. *Nature Communications* **2**, doi:10.1038/ncomms1464 (2011).

140 Emani, N. K. *et al.* Electrical Modulation of Fano Resonance in Plasmonic Nanostructures Using Graphene. *Nano Letters* **14**, 78-82, doi:10.1021/nl403253c (2014).

141 Schedin, F. *et al.* Detection of individual gas molecules adsorbed on graphene. *Nature Materials* **6**, 652-655, doi:10.1038/nmat1967 (2007).

142 Simon, P. & Gogotsi, Y. Materials for electrochemical capacitors. *Nature Materials* **7**, 845-854, doi:10.1038/nmat2297 (2008).

143 Stoller, M. D., Park, S. J., Zhu, Y. W., An, J. H. & Ruoff, R. S. Graphene-Based Ultracapacitors. *Nano Letters* **8**, 3498-3502, doi:10.1021/nl802558y (2008).

144 Chopra, N. G. *et al.* Boron-Nitride nanotubes. *Science* **269**, 966-967, doi:10.1126/science.269.5226.966 (1995).

145 Novoselov, K. S. *et al.* Two-dimensional atomic crystals. *Proceedings of the National Academy of Sciences of the United States of America* **102**, 10451-10453, doi:10.1073/pnas.0502848102 (2005).

146 Nair, R. R. *et al.* Fine structure constant defines visual transparency of graphene. *Science* **320**, 1308-1308, doi:10.1126/science.1156965 (2008).

147 Pu, Y., Grange, R., Hsieh, C. L. & Psaltis, D. Nonlinear Optical Properties of Core-Shell Nanocavities for Enhanced Second-Harmonic Generation. *Physical Review Letters* **104**, doi:10.1103/PhysRevLett.104.207402 (2010).

148 Kauranen, M. & Zayats, A. V. Nonlinear plasmonics. *Nature Photonics* **6**, 737-748, doi:10.1038/nphoton.2012.244 (2012).

149 Ciraci, C. *et al.* Probing the Ultimate Limits of Plasmonic Enhancement. *Science* **337**, 1072-1074, doi:10.1126/science.1224823 (2012).

150 Pohl, H. A. *Dielectrophoresis*. (Cambridge University Press, 1978).

151 Novotny, L., Bian, R. & Xie, X. Theory of nanometric optical tweezers. *Physical Review Letters* **79**, 645-648, doi:10.1103/PhysRevLett.79.645 (1997).

152 Krupke, R., Hennrich, F., von Lohneysen, H. & Kappes, M. Separation of metallic from semiconducting single-walled carbon nanotubes. *Science* **301**, 344-347, doi:10.1126/science.1086534 (2003).

153 Laks, B. & Mills, D. L. Photon-emission from slightly roughened tunnel-junctions. *Physical Review B* **20**, 4962-4980, doi:10.1103/PhysRevB.20.4962 (1979).

154 Marinica, D. C., Kazansky, A. K., Nordlander, P., Aizpurua, J. & Borisov, A. G. Quantum Plasmonics: Nonlinear Effects in the Field Enhancement of a Plasmonic Nanoparticle Dimer. *Nano Letters* **12**, 1333-1339, doi:Doi 10.1021/Nl300269c (2012).

155 Pelton, M. & Bryant, G. W. *Introduction to metal-nanoparticle plasmonics*. pp 135-161 (John Wiley & Sons, Hoboken, 2013).

156 Dawson, P. & Boyle, M. G. Light emission from scanning tunnelling microscope on polycrystalline Au films - what is happening at the single-grain level? *Journal of Optics a-Pure and Applied Optics* **8**, S219-S226, doi:10.1088/1464-4258/8/4/s23 (2006).

Appendix A

Fabrication Methods and Recipes

A.1 Atomic layer deposition and deposition rate calibration.

High temperature (at 250 ºC) ALD recipe: Typical rate 1.1 Å / cycle

1. Purge chamber with N_2 20 sccm for 20 seconds
2. Water vapor pulse last for 0.015 seconds
3. N_2 purge for 5 seconds
4. TMA pulse last for 0.015 seconds
5. N_2 20 sccm purge for 5 seconds
6. Go back to step 2 and repeat until reach the desired thickness.

Low temperature (at 50 ºC) ALD recipe: Typical rate 1.0 Å / cycle

1. Purge chamber with N_2 for 20 seconds
2. Water vapor pulse 0.035 seconds
3. N_2 purge last for 20 seconds
4. TMA pulse for 0.035 seconds
5. N_2 purge for 20 seconds
6. Go back to step 2 and repeat until reach the desired thickness.

Preparation of ALD calibration sample on template stripped silver is shown in Figure

A.1. Other methods to calibration of ALD deposition rate include measurement using

standard method in ellipsometry, AFM, SEM top view and cross-section view, and TEM cross-section view of the nanogap. The fabrication processes of the AFM and TEM samples to calibrate ALD deposition rate are discussed below.

AFM sample preparation

A step in ALD deposited alumina film is created on template-stripped ultra-smooth silver film. AFM is used to scan an area across the step to measure the height of the step, i.e. the alumina thin film thickness.

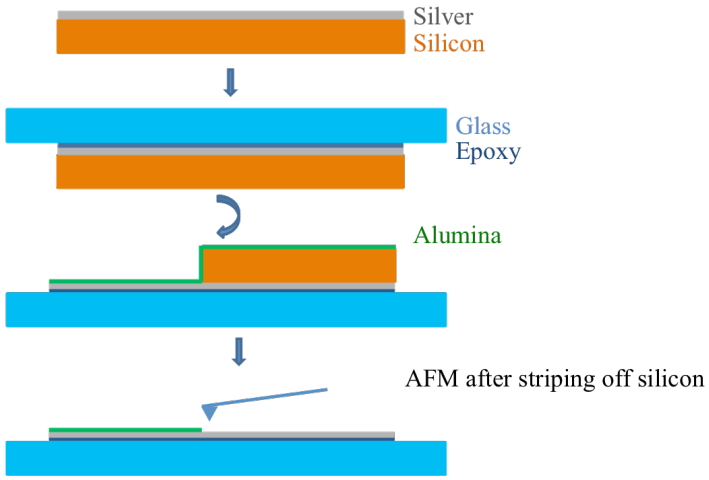

Figure A.1 Fabrication process of AFM sample for ALD deposition rate calibration. From top to bottom, first a silver film is deposited on a clean silicon piece, and then the silicon piece is partially removed by stripping. In this case, the silver underneath the remained silicon piece is under protection in the following ALD deposition process. The whole sample is then coated with alumina using ALD. At last, the remained silicon piece is removed by template stripping. And then the sample is ready for AFM scan.

TEM sample preparation

A lamina of the Au/alumina/Au structure is cut from a nanogap at one side of the rectangular nanogap loop by FIB milling. The lamina is picked up using an OmniProbe nanomanipunator inside FIB and is attached to a TEM grid. The lamina is further thinned with FIB milling to lesser than 100 nm for imaging by TEM (JEM-ARM200F, JEOL).

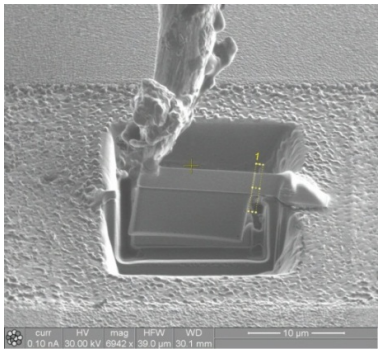

Figure A.2 TEM sample preparation: cut a thin lamina through a nanogap with FIB and then pick the thin lamina, which contains a nanogap, by an Omni probe.

A.2 Atomic layer lithography

1. Process for photolithography on glass substrate

Clean Pyrex glass wafer: soak in fresh H_2SO_4: H_2O_2= 1: 1 for 10 minutes, then clean with running DI water for 5 minutes, then dry with a wafer drier;

Dehydrate on hot plate at 200 ºC for 5 minutes;

Spin coat NR71-1500P at 3000 PRM for 45 seconds for resist thickness about 1.6 µm;

Bake on hot plate at 150 ºC for 90 seconds (or 2 minutes);

Ma6, contact aligner, exposure 27 seconds (17 to 25 sec), 20 µm gap between mask and substrate, hard contact mode;

Bake on hot plate at 100 ºC for 90 seconds;

Develop in developer RD 6 for 23 seconds (or 20 seconds);

Descum with STS RIE with condition: (O2NILOW) O_2 100 sccm, 50W, 100 mTorr, for 20 seconds.

2. Metal deposition (Gold with a Ti or Cr adhesion layer, or silver alone) with Temescal, at a deposition rate of 1 Å / second.
3. Lift off with 1165 remover overnight, and then gentle sonication for 5 minutes.
4. Clean the sample with Acetone, methanol, and isopropyl alcohol.
5. Deposit alumina by ALD.
6. Metal deposition with Temescal, at a deposition rate of 1 Å / seconds.
7. Apply 3M Scotch Magic Tape to peel off the excess metal on top of the pattern to expose nanogaps.

A.3 Chip scale nanogap devices with electrodes

1. After peeling off the top metal layer from the centimeter long nanogap sample, cover one gap at the side of the rectangular nanogap ring with cover glass slide, and expose the other nanogap, as shown in the figure A.3 below;

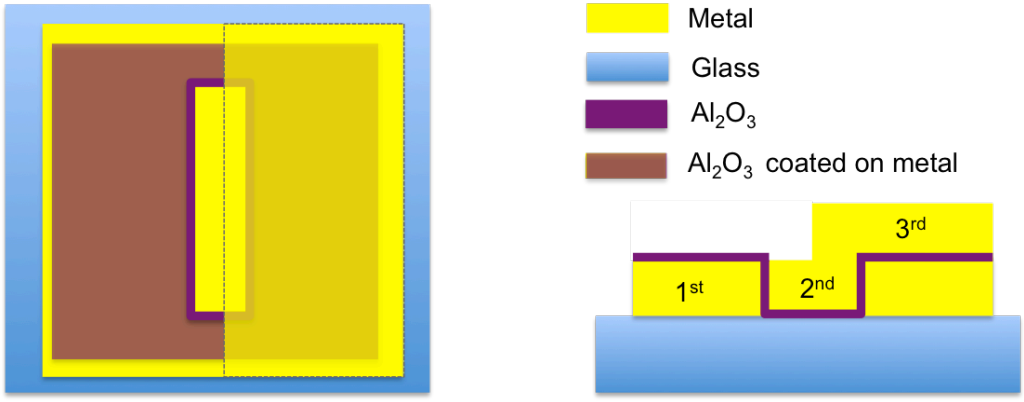

Figure A.3 Sacrifice one gap by depositing a 3rd metal layer. The purpose is to make electrical connection between the 2nd metal to the electrode, which will be patterned in the 1st metal layer in the following processes. The third metal is deposited by sputter using a cover glass slide to cover (protect) one nanogap (Cover glass is used here to avoid another lithography.) and sanctifies the exposed gap.

2. Sputter Au with adhesion layer (3.5 nm Ti (rate: 7nm/min, 30 s) and 72 nm Au (rate: 43 nm/min, 100 s)) using AJA II to make connection over one nanogap to electrically connect the first metal and the second metal layers deposited in the atomic layer lithography process;

Second photolithography to make electrical connection:

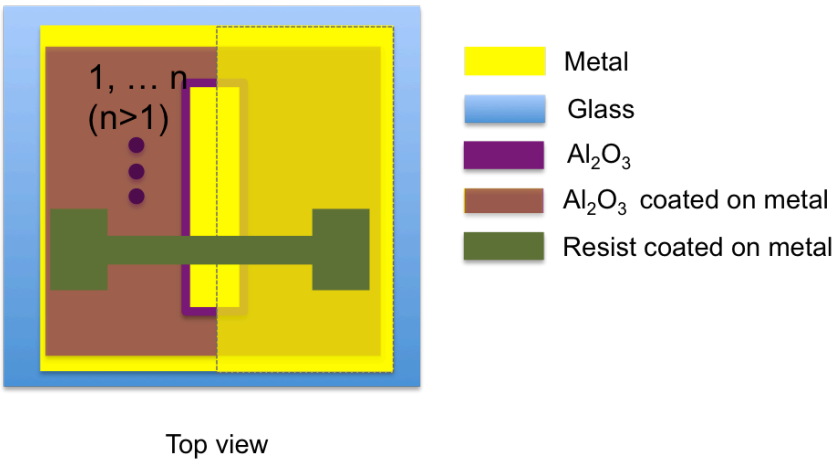

Figure A.4 Photolithography on a nanogap substrate to define electrodes.

3. After sputtering, remove any tape residues on the samples by Acetone, Methanol and IPA. Use Q-tips to help if necessary;
4. Bake the chip on a hot plate at 100 ºC for 2 minutes;
5. Spin coat: NR71-1500P, 3000 RPM for 45 seconds;

6. Pre-bake on hot plate 100 °C for 4 minutes for 30 seconds. Lower temperature is preferred to avoid deforming of nanogaps;
7. Exposure with Ma6 for 18 seconds, hard contact mode, with 20 µm gap;
8. Post bake at 100 ºC for 90 seconds;
9. Develop in RD6 for 20 seconds, followed by soaking in water for 3 minutes;
10. Remove residual resist on the samples with STS etcher using O2Clean (O_2 100 sccm, 100 W, 100 mTorr), for 30 seconds;
11. Etch through the exposed metal (Gold etch rate ~ 162 nm / min, alumina etch rate ~ 9 nm/min) using ion mill etcher, with the resist as etching mask;

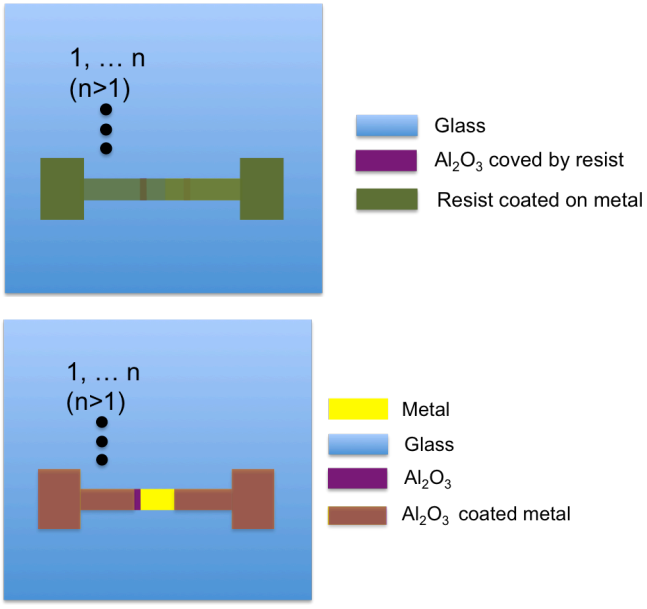

Figure A.5 Top view of the patterns after ion mill etching (top) and after remove resist (down). The thin alumina layer (purple color) shows that the nanogap insulates two metal electrodes.

12. Soak the sample in 1165 remover for about 10 minutes to remove resist. The solvent can be heated to about 90 ºC to aid the removal process;
13. Check the electrical connection before adding fluidics.

A.4 Buried nanogap

1. Lithography with Canon Stepper

   Clean silicon wafer: soak in BOE for 10 seconds to remove native oxide, clean in running water for 5 minutes; soak in fresh H_2SO_4: H_2O_2= 1: 1 on a hotplate at 125 ºC for 10 minutes, then clean with running water for 5 minutes, then dry the wafer with a wafer dryer;

   Dehydrate on hot plate at 200 ºC for 5 minutes;

   Bake on a hot plate at 110 ºC for 60 seconds;

   Immerse in HMDS vapor for 2 minutes to promote adhesion between wafer and resist;

   Spin coat resist MiR 701 at 4000 RPM for 30 seconds;

   Soft bake at 110 ºC for 60 seconds;

   Exposure with Stepper at a dose of 210mJ/cm^2 and focus = 0;

   Develop in developer CD26 for 33~35 seconds;

   Descum with STS RIE with O2NILOW (O_2 100 sccm, 50 W, 100 mTorr), for 20 seconds.

2. Deposit metal (Au) with CHA or Temescal.
3. Lift off the metal in acetone for a few hours;
4. Remove any organic residue (descum) with STS RIE with O2Clean for 30 seconds;
5. Coat the sample with ALD alumina for desired thickness;
6. Conformal metal deposition use CHA (with planetary fixture) or AJA II sputter;
7. Apply epoxy (NOA 61, Norland Products Inc.), expose to UV light for 15 minutes, and cure on a hot plate at 55 ºC over night (more than 12 hours).

A.5 Nanogap on wedge

1. Process to make wedges in (110) silicon wafer: use 100 nm / 200 nm Si_3N_4 on top of silicon wafer as etching mask.

   Dehydrate on a hot plate at 200 ºC for 5 minutes;

   Bake on a hot plate at 105 ºC for 90 seconds;

   Immerse in HMDS vapor for 2 minutes to promote adhesion between wafer and resist;

   Spin coat SPR955, 0.7 cm at 4000 RPM for 30 seconds;

   Soft bake 110 ºC for 60 seconds;

   Exposure at dose: 135 mJ/cm^2, focus = 0;

   Develop in developer CD26 for 60 seconds;

   Descum with STS RIE with O2Clean for 20 seconds;

   Etch through the exposed Si_3N_4 with STS;

   Remove resist with STS RIE with O2Clean, for 4 minutes;

   Remove any organics using fresh H_2SO_4: H_2O_2= 1: 1 for 10 minutes;

   Clean with running water for 5 minutes, then dry with wafer dryer;

   Soak in 30% concentration KOH saturated with IPA at 80 ºC, for 30 minutes to 40 minutes to etch into silicon to make wedges.

2. Pattern in 3D substrate (buried nanogaps on wedge)

   Dehydrate the wedge patterned silicon piece on a hot plate at 200 ºC for 10 minutes;

   Soak in HMDS vapor for 5 minutes;

   Spin coat NR71-1500P at 500RPM for10 seconds, then at 3000RPM for 45 seconds;

   Prebake on hot plate at 150 ºC for 60 seconds;

   Exposure using Ma6 for 25 seconds, 20 μm gap, and hard contact mode;

Soft bake on hot plate at 100 ºC for 60 seconds;

Develop in RD 6 for 25 seconds; (20 sec)

Descum with STS etcher with O2Clean for 30 seconds;

Deposit metal with CHA or Temescal and lift off, to get metal stripes patterned in the wedges;

Deposit dielectric film on the sample by ALD to define nanogap size;

Deposit a second metal layer two times thicker than the 1st metal layer by sputtering;

Apply UV epoxy (NOA 61, Norland Products Inc.) to the Au surface, put a standard glass slide on top of it, cure the sample under UV light (360 ~ 370 nm) for 15 minutes, and cure the epoxy on a hotplate at 65 ºC for 12 hours;

Template strip to expose the wedges and the nanogaps on top of the wedge tips.

A.6 Planar gap e-beam lithography process

Follow the above-mentioned process to clean a silicon wafer;

Deposit 30 nm Au, with a rate of 0.1 Å /sec for 100 Å, then speed up to 1 Å /sec to get 30 nm Au film in total;

Template strip following the above-mentioned process in A.5;

Coat the sample with ALD alumina layer at 50 ºC with a typical rate of 1 Å/ cycle;

Spin coat: PMMA A4, speed 4000 RPM, 30 seconds, soft bake in oven at 110 ºC for 1 hour, mainly because the epoxy can not stand temperatures higher than 125 ºC;

No conductive layer is needed, as there is a gold film at the bottom of resist. Expose dose depends on each pattern (does about 850-1100 $\mu C/cm^2$, depends on pattern size, resolution 1 or 2 nm, current 1 or 2 nA). Then develop in MIBK:IPA= 1: 3 for 30 seconds, soak for 30 seconds in IPA, and then blow-dry with N_2;

Follow the low power descum process to remove any PMMA residue on the alumina surface;

Deposit 30 nm Au by e-beam evaporation;

Lift off in acetone for about 5 to 10 minutes.

A.7 Planar gap for tunneling-induced light emission

Here, the fabrication processes of the *samples A, B, C* and *D* in section 6.2 are discussed in detail.

Sample A,

1. Follow the process from spin coating step in A. 6 to make metal nano metal gratings on silicon wafer. The wafer is already pre-patterned with easily accessible electrode pattern (gold, without adhesion layer). The pattern design is shown in Figure A.6, where the green color block is micro sized metal pattern made with e-beam lithography. The blue color grating is the pattern design for e-beam lithography. The width of the metal lines can be tuned to get different resonances from the nanogap. The patterns are written with different beam dose, and aligned to pre-patterned electrode pad using alignment-writing process in Vistec-EBPG5000+ machine.

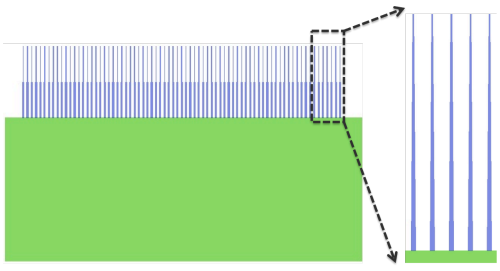

Figure A.6 Pattern design for planar nanogaps with aligned e-beam lithography.

2. Use ALD to deposit 3 to 5 nm alumina thin film on the metal gratins.

3. Use a cover glass slide to cover the green pattern in the above figure. Deposit a second layer of gold (2nd gold) on top the grating and other exposed area by sputtering. This is a rough fabrication process. The purpose to use this process is to avoid any contamination on the alumina layer during lithography process.
4. Then cover the whole structure, and only partially expose the second deposited metal, and deposit a third metal (3rd gold) with adhesion layer as another electrode. The whole device looks like the Figure A.7 below.

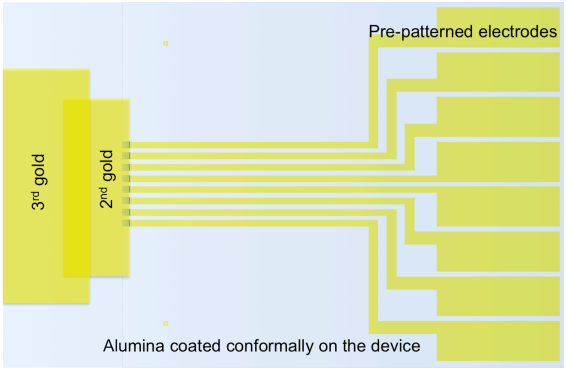

Figure A.7 Schematic of *Sample A*.

Sample B

1. Follow the process in A. 6 to make gratings on silicon substrate.
2. Follow the standard process for S1813, and use Ma6 mask aligner to pattern electrode 1, with finger shaped patterns (similar to the pattern shown in Figure A.5)).
3. Follow the process A. 5 from 5) to 7), except that the ALD is done at 250 ºC.
4. Deposit another gold layer on top the finger shaped patterns by following the process for *Sample A*. 3 to make the second electrode.

Sample C

Follow the process for *Sample A*.1 to make metal gratings on pre-patterned glass substrate, except that the pre-patterned electrode has Ti adhesion layer underneath it.

Sample D

Follow the process for *Sample A*.1 to make metal gratings on pre-patterned silicon substrate, except that the gratings are deposited on top of the pre-patterned electrode.

A.8 Stencil lithography for planar nanogap

1. The process for fabricating suspended nitride film:

   Define patterns on the front side of a Si_3N_4 (LPCVD grown 200 nm Si_3N_4 on both sides of silicon wafer) silicon wafer using Canon stepper or e-beam lithography;

   Etch into nitride using the resist as mask (O2Clean for 30 seconds and Nit1 (CF_4 40 sccm, O_2 4 sccm, pressure 100mT, power 100 watts) etch for 80 seconds), leave around 50 nm thick nitride film in the pattern. Need to cover the backside of the wafer with photoresist for protection;

   Remove resist with acetone, methanol, and isopropyl. Coat the front surface with a new layer of resist to for protection;

   Do another photolithography on the backside of wafer to define KOH etching window;

   Descum with O2Clean for 30 seconds and etch the exposed Si_3N_4 exposed from last step for using 3 min Nit1 to open the KOH etching window;

   Remove resist with O2Clean on each side of the wafer for 5 minutes;

   Completely remove resist with H_2SO_4 : H_2O_2 = 1: 1 on 125 ºC hotplate for 10 minutes;

Etch through silicon wafer using 30% concentration KOH saturated with IPA. It is better to cut the wafer before KOH etch; otherwise the cutting process might put too much force on the suspended film and break it;

Soak the film in water for half hour to completely remove KOH;

Set the wafer still for drying in air. Don't process until the wafer is completely dry;

On the front side, Nit1 etch for 70 second to etch through the left nitride film to open the apertures.

2. Metal deposition with stencils:

Apply the stencil mask to the substrate upside down for deposition metal (for planar gap: dielectric film coated metal thin film). Fix the mask to sample substrate with tape;

Deposit metal in CHA. Sputtering is not preferred, due to the deposition to the area around the designed pattern area.

A.9 Form BZT monolayer on gold or silver surface

The BZT used in this thesis is diluted from BZT, Sigma-Aldrich, with ≥99% purity to a 2 mM solution with ethanol. Before putting the nanogap sample into the solution, the alumina inside the nanogap is first partially removed by BOE etching, which the etching rate is around 1 nm / second, with an etching time that allows the depth of etching into

the gap close to the width of the nanogap. Then the nanogap samples are soaked in the solution for 24 hours to allow forming BZT monolayer on metal top surface and sidewall inside the gap. Before measurement, the samples are cleaned with flow ethanol for 2 minutes to remove excess BZT molecules. The angle of the BZT molecules on metal surface might be different depends on the crystalline directions of the metal. For simplicity, the angle of the molecules to surface is assumed to be 90º to the surface, both on the flat surface and on the sidewall inside of nanogaps.

A.10 Definition of local and average enhancement factor for SERS

The averaged enhancement factor is calculated by considering the metal surface area defined by the confocal spot size of the lens at particular laser wavelength. The confocal spot area plus the metal area within the nanogaps is used to calculate N_{surf}. The local EF reveals the field enhanced more close to or in the nanogap, by ignoring the molecules outside of the nanogap where the electric filed is relatively low. The localized EF is calculated using the gap area at the tip of the wedge obtained from SEM. Here, the gap width and depth are 2 nm. The diameter of the tip is 20 nm. So the area inside the gap is 2 nm × 20 nm × 2. In both cases, I_{gap} and I_{vol} are measured by subtracting background CCD counts at 900 cm^{-1} from the CCD counts of the interested scattering band.

Appendix B

Acronyms

Table B.1 A list of common acronyms used in the thesis.

Acronym	Definition
AFM	Atomic Force Microscopy
ALD	Atomic Layer Deposition
BOE	Buffered Oxide Etchant, HF: H_2O=1:10
BZT	Benzenethiol
DEP	Dielectrophoresis
e-beam	Electron beam
FDTD	Finite Difference Time Domain
FIB	Focused Ion Beam
FP	Fabry-Pérot
LSPR	Localized Surface Plasmon Resonance
PDMS	Polydimethylsiloxane
PMMA	Polymethyl Methacrylate
SAM	Self Assembled Monolayer
SHG	Second Harmonic Generation
SEM	Scanning Electron Microscopy
SEIRA	Surface Enhanced Infrared Absorption
SERS	Surface Enhanced Raman Scattering
SP	Surface Plasmon
SPPs	Surface Plasmon Polaritons
TEM	Transmission Electron Microscopy
THG	Third Harmonic Generation
TMA	Trimethylaluminum